Utilization of Internal Resonance in Gyroscope Design

by

Amr Marzouk

M.A.Sc., Simon Fraser University, 2009
B.Sc., Arab Academy for Science and Technology, 2007

Thesis Submitted in Partial Fulfillment of the

Requirements for the Degree of

Doctor of Philosophy

in the

School of Mechatronic Systems Engineering

Faculty of Applied Sciences

SIMON FRASER UNIVERSITY

Fall 2014

Approval

Name:	**Amr Marzouk**
Degree:	**Doctor of Philosophy**
Title:	***Utilization of Internal Resonance in Gyroscope Design***
Examining Committee:	**Chair:** Woo Soo Kim Assistant Professor

Farid Golnaraghi
Senior Supervisor
Professor

Behraad Bahreyni
Supervisor
Associate Professor

Mehrdad Moallem
Supervisor
Professor

Albert Leung
Internal Examiner
Professor
School of Engineering Science
Simon Fraser University

Joseph Cusumano
External Examiner
Professor
Engineering Science and Mechanics
Pennsylvania State University

Date Defended/Approved: November 26, 2014

Partial Copyright Licence

Abstract

Coriolis vibratory gyroscopes (CVG) suffer from various error sources including manufacturing imperfections and environmental factors. This poses a difficult solution called “mode matching” requiring complex and accurate on-chip electronics.

The research discussed in this thesis acts as a proof of concept on utilizing well-established phenomena in the field of nonlinear dynamics and vibration in the design of CVG gyroscopes with improved sensitivity and robustness against manufacturing imperfections. A significant increase in the sense mode bandwidth is shown by structurally tuning the system to 2:1 resonance between the sense and drive modes respectively.

A simplified mathematical model of a two-degree-of-freedom system, having quadratic nonlinearities, is obtained and compared qualitatively to more complex models from literature. Experimental results verify numerical simulations, confirming the aforementioned hypothesis. Additional bandwidth enhancement possibility is established through simple feedback of the nonlinear coupling terms obtained from the mathematical models.

Keywords: Internal resonance; saturation; nonlinear vibration; gyroscope; resonator

To my dearly beloved wife Alyaa and son Adam

Your boundless love, support and patience have and will always empower me

Acknowledgements

Firstly I would like to thank Professor Golnaraghi. This work would not have been completed without his patience and foresight. His positive influence and everlasting excitement have helped me shape my goals. I am grateful to his invaluable guidance in many aspects of life.

I would also like to thank Professor Behraad Bahreyni on his time and support throughout this research. His multidisciplinary expertise helped in building the framework of applications of this research in MEMS scale. Moreover, I am very grateful to Professor Mehrdad Moallem for his time, support and feedback on this research. I am keen on thanking my external and internal examiners Professors Joseph Cusumano and Albert Leung for their dedicated time and valuable feedback.

I would like to thank my parents Maha and Alaa and my sisters for their immeasurable encouragement and sacrifices. I am very much obliged to Monsieur Jacques Desplaces. His limitless encouragement and unbounded support throughout my graduate studies had major influence on my career path.

I would like to thank my friend and collaborator Atabak Sarrafan for his extremely helpful support. Together and Oldooz Pooyanfar, we established a great research team in a very positive, respectful and friendly work environment.

In addition, our treasured technical staff Mustafa Sajid, Taha Al-Khudairi, Zain Khanzada and Gary Wan have been of extreme help. Last but not least, I would like to thank our administrative management staff Julibeth Fernandez, Jennifer Leone and Carol Jang for all their help and kind support.

Table of Contents

List of Figures

List of Symbols

$\vec{r}_i^j$	Position of *i* with respect to *j* $[m]$
$\vec{v}_i^j$	Velocity of *i* with respect to *j* $[m.s^{-1}]$
$\vec{a}_i^j$	Acceleration of *i* with respect to *j* $[m.s^{-2}]$
x	Displacement with respect to *x*-axis $[m]$
$\dot{x}$	Velocity with respect to *x*-axis $[m.s^{-1}]$
$\ddot{x}$	Acceleration with respect to *x*-axis $[m.s^{-2}]$
y	Displacement with respect to *y*-axis $[m]$
$\dot{y}$	Velocity with respect to *y*-axis $[m.s^{-1}]$
$\ddot{y}$	Acceleration with respect to *y*-axis $[m.s^{-2}]$
$\hat{e}_i$	Unit vectors *i* = 1, 2, 3 along the *x, y* and *z* axes gyroscope rotating frame of reference
Ω	Applied angular velocity $[rad.s^{-1}]$
$\dot{\Omega}$	Applied angular acceleration $[rad.s^{-2}]$
m	Mass $[Kg]$
f	Forcing amplitude $[N]$
k	Spring constant $[N.m^{-1}]$
c	Damping coefficient $[N.\mathrm{s}.m^{-1}]$
Ω	Natural frequency $[rad.s^{-1}]$
ζ	Damping Ratio
θ	Coordinate angular displacement $[rad]$
$\dot{\theta}$	Coordinate angular velocity $[rad.s^{-1}]$
$\ddot{\theta}$	Coordinate angular acceleration $[rad.s^{-2}]$
l	Length $[m]$
I	Inertia $[Kg.m^2]$
V	Potential Energy $[joules]$
T	Kinetic Energy $[joules]$
ρ	Nondimensional displacement
γ	Nondimensional damping
τ	Nondimensional time
ξ	Fast nondimensional time scale
η	Slow nondimensional time scale
σ_1	Internal detuning parameter $\omega_1 = 2\omega_2 + \varepsilon\sigma_1$
σ_2	Drive mode natural frequency detuning parameter away from a specific natural frequency
u	Generalized coordinate
$\dot{u}$	Generalized velocity
$\ddot{u}$	Generalized acceleration
a	Nondimensional modal amplitude

Chapter 1.

Introduction

1.1. Background and Motivation

In ancient times, Greek, Chinese and Roman societies constructed the first gyroscopes as a self-balancing spinning toy. Sailors were the first to use gyroscope like devices to locate the horizon in foggy or misty conditions. In 1851, the device was named a "gyroscope" by French scientist Leon Foucault and used to detect rotation of planet Earth. The gyroscope designed by Foucault was a long, heavy pendulum which was set to swing back and forth along the north-south plane, while Earth turned beneath it [1].

Navigation grade gyroscopes such as the Sperry gyroscope employed a rotating momentum wheel fixed to a gimbal structure. These types of gyroscopes suffered from several drawbacks, mainly related to bearing friction and wear. The solution to the bearing problem was the elimination of rotating parts. As a result, the vibrating gyroscopes, such as the Hemispherical Resonator Gyroscope (HRG) and Tuning Fork Gyroscopes, were introduced as alternatives. Recently, there have been alternative high-performance technologies such as fibre-optic gyroscopes (FOG) and ring laser gyroscopes (RLG), which are relatively more accurate. For this reason, fibre-optic gyroscopes and ring laser gyroscopes are mainly applied to high-end applications.

Coriolis vibratory gyroscopes (CVG) are designed based on the fictitious force induced on a moving mass with respect to a rotating frame of reference [2]. They are currently being used in many navigation applications, ranging from systems such as Inertial Navigation Systems (INS), automotive anti-rollover and suspension controls, rehabilitation and video-gaming controllers such as those used in the PlayStation™ and Wii™. In inertial

navigation applications, gyroscopes, accelerometers and magnetometers are components of an inertial measurement unit (IMU) also called an Attitude and Heading Reference System (AHRS). IMU's have great potential for indoor motion tracking systems in manufacturing [3], human supporting systems [4], rehabilitation [5], and a range of other applications. One of the most important components to obtain accurate orientation using an IMU is the gyroscope. The three angular velocities are integrated to obtain angular displacement. This integration step introduces drift directly related to noise density and sensitivity of the gyroscope. In the consumer market, gyroscopes are commonly manufactured based on Micro-electromechanical Systems (MEMS) technology, which are produced at low cost with medium accuracy and sensitivity. However, MEMS gyroscopes are subject to manufacturing imperfections and manufacturing defects that significantly impact their performance due to their design and complexity of their implementation.

Most commercial MEMS CVG gyroscopes are generally composed of a proof mass moving in two degrees of freedom (DOF) forming drive and sense modes, respectively. Upon periodic excitation of the drive mode - mainly electrostatically - an external rotation (with the rotation axis normal to that of the drive mode) results in a Coriolis force that transfers the vibration energy from the drive to the sense mode [1]. These modes are normally tuned to the same resonance frequencies (i.e. mode-matched or tuned to 1:1 ratio) in order to maximize their corresponding vibration amplitudes [6]. Realistically, this tuning is challenging to achieve due to manufacturing imperfections, and "significant amplification gains are lost" [7]. Utilizing nonlinear dynamics (the focus of this research) in the design process can significantly improve the performance of gyroscopes specifically and sensors relying on the principles of modal interactions in general [8].

The developments of mitigation techniques to compensate for gyroscope errors- such as bias and drift- have been an active area of research for decades. The most commonly used strategy has been through utilizing sensor fusion algorithms. As the name suggests, the basic idea of sensor fusion is based on combining data from multiple redundant sensors to predict the best estimate of sensor values. Parnian and Golnaraghi [9] developed an indoor inertial navigation system based on fusing the 3D position and

orientation information from both a stereovision camera system and an IMU using a variation of the Extended Kalman Filter (EKF) algorithm. This system was then applied to estimate the position and orientation of surgical tools during an operation- a system named commercially as the Surgical Navigation System (SNS). Won and Golnaraghi [10] developed a fastening tool system for the automotive industry by calibrating and fusing IMU data with string potentiometers for quality assurance. Marzouk and Golnaraghi [11] utilized EKF as a sensor fusion algorithm aided with a mechanical model of the human arm to be used in a post-stroke rehabilitation application. As a result of this extensive research by our research team, robustness and sensitivity have always been a challenge resulting mainly from the IMU system component caused by the gyroscope specifically.

This research aims at studying the effects of nonlinear dynamics and vibration on (a) the resonator and (b) on the gyroscope to improve robustness and sensitivity. This serves as a proof of concept for future work on implementing these concepts in micro-scale designs of parametric resonators and gyroscopes.

1.2. Literature Review

Early in the eighteenth century, mechanical gyroscopes were used for measuring orientation; after the MEMS revolution, micro-machined gyroscopes were developed based on a variety of physical phenomena. In 1942, a patent for a tuning fork CVG was registered to F.W. Meredith and later improved by Hobbs and Hunt in the 1950s [12]. Scientists and researchers who developed the miniature tuning fork gyroscopes using MEMS technology used the same theory of operation as that in the earlier mechanical one. However, several key parameters had to be taken into consideration due to the extremely small size of the MEMS structure.

The first CVG MEMS gyroscope design used two vibration modes to measure angular velocity [13]. The first mode was excited by the system in order to generate Coriolis forces accompanying rotation. The second mechanism used a capacitive-based structure to transform Coriolis vibrations from the physical mechanical quantity into its

electrical form as a voltage or duty cycle signal. After that, the sensor readings were filtered and amplified according to the sensor specifications, using electronic circuits that can also be embedded on the same semiconductor die. Analog Devices showed that their iMEMS™ gyroscope design was based on the concept of measuring the Coriolis acceleration [14]. Draper Labs made another one of the first of announcements of a fully functioning CVG [15].

Due to unavoidable manufacturing imperfections, a major drawback in CVG design lies in mode matching the excitation drive-signal frequency with the resonance frequency of the structure. A minor shift in the excitation frequency can result in a gain drop and consequently sensitivity. As demonstrated by A. Cenk and A. Shkel, [1], a 5 Hz relative shift in the drive-signal of a CVG with a high quality factor (QF = 10000) resulted in a 90% gain drop. This decreased the overall gain of the sensor [16],[17]. Moreover, it can render manufacturing to be challenging [5], [18]. Another major element contributing to the difficulty of mode matching is the damping coefficients of the system. It can vary during or after the manufacturing process is completed due to package leaks (which leads to vacuum loss) and temperature change resulting from internal friction.

One of the most successful mechanical approaches introduced multiple degrees of freedom to increase the bandwidth of the sense mode and hence increased robustness and immunity to the aforementioned imperfections [19]–[23]. One mitigation strategy they used to increase bandwidth was to design a multi-DOF resonator as shown by C. Acar and A. M. Shkel [24][25]. Despite its complexity, this approach showed promising results. Nevertheless, the multiple DOF approach increases design constraints. Other control-based proposed solutions used adaptive control and tuning [26], [27].

In order to increase the sensitivity of a CVG (i.e. obtain a higher sense-mode proof-mass displacement per angular rate input), the sense and drive mode natural frequencies should match [28] under low damping conditions [29]. Some research groups conducted physical experiments to show the nonlinear phenomena in MEMS gyroscopes and offered mathematical models for its mitigation. Researchers in [30] collaborated with STMicroelectronics to model a few types of these nonlinearities. Their semi-analytical

solution was built on a two-dimensional FEA model (using FEMLAB/COMSOL™ Multiphysics) of a classical vibrating MEMS comb drive used in the design of both accelerometers and gyroscopes. The nonlinear results were further curve fitted using a third order polynomial. Finally, the polynomial fit calculated parameters were used to build a lumped element model and a physical prototype to verify the numerical results. In the physical experiments, they used a Polytech™ Doppler vibrometer to measure the proof mass velocity at each excitation frequency using a microscope for aiming the vibrometer's laser pointer on the proof mass. The obtained velocity from the vibrometer was further divided by the drive frequency to obtain displacement [31]. Results showed that the support beams induced structural nonlinearities. A numerical and a semi-analytical model was devised to outline these nonlinearities and then compared to experimental results. The numerical methods used were adapted from [32].

Another experimental proof was produced by A. Trusov et al [33] to show the nonlinear dynamics of electrically actuated resonators. They used a simple MEMS multi-cantilever accelerometer designed by Senata Technologies was used with masses attached to the end of each tip. Moreover, it has also been shown that the sub-harmonic resonances appear at an excitation frequency close to twice the fundamental natural frequency of the resonator.

The small signals produced by gyroscopes require displacement measurements in the order of Fermi (10^{-15} of a meter) and charges comparable to that of a single electron [34]. Utilizing nonlinear dynamics in the design process can significantly improve the performance of inertial sensors [8]. In 1984 [35], an L-beam macro-scale structure was built with a 2:1 ratio between its first two natural frequencies, the nonlinear internal resonance phenomenon was shown through analytical modeling and nonlinear vibration analysis techniques (explained in more details in Chapter 2 of this thesis). A few key publications ([36], [37], [38], [39]) were published in which the internal resonance was utilized to control the vibration of an oscillatory system. In [40], Golnaraghi studied the nonlinear behavior of a rotating flexible robot arm with similar equations of motions to a gyroscope. In [36], a strategy was proposed for controlling the free vibrations of a second-

order system coupled to a controller (itself a second-order system) utilizing quadratic nonlinear terms. Upon proper tuning of the controller's natural frequency to a 2:1 ratio, the nonlinear terms act as an energy bridge, causing the vibrations of the plant to be transferred to the controller. In [37], this concept was extended to forced vibration, which takes advantage of the saturation phenomenon that occurs when two natural frequencies of a system with quadratic nonlinearities are in the ratio of 2:1. When the system was excited at a frequency rate close to higher than that of the natural frequency, most of the input energy is channeled to the secondary system to be actively controlled.

The governing equations in this case were very similar to those of a gyroscope, and the quadratic nonlinearities used were identical to the Coriolis terms in gyroscope mathematical models. The main goal of this research is to use these principles to enhance and immunize MEMS gyroscopes against manufacturing nonlinearities by increasing robustness.

The principle idea of this research is based on applying the nonlinear principles, namely internal resonance and saturation in gyroscope design. These principles have attracted a great deal of attention over the past few years for several other applications. To maximize the sensitivity of gyroscopes, drive and sense modes have been usually designed to the same resonance frequencies (i.e. mode matched or tuned to a 1:1 resonance ratio between these modes), have high quality factors and large proof mass, and are driven with large amplitudes [6]. This research area, which has been active for approximately a decade, involves the study of nonlinear behaviors arising in small scale, vibratory, and mechanical devices that are typically integrated with highly accurate electronics for use in signal processing, actuation, and sensing applications. The inherent nature of these devices, which includes low damping, desired resonant operation, and the presence of nonlinear potential fields, sets an ideal stage for the appearance of nonlinear behavior. While nonlinearities are typically avoided in device design, they have the potential to allow designers to beneficially use nonlinear behavior in certain applications.

1.3. Objectives

The broader goal of this research is to improve robustness and sensitivity of MEMS gyroscopes by decreasing the sense-mode gain loss due to manufacturing imperfections relative to the quality factor. In this thesis, this goal is achieved by increasing the sense mode's bandwidth by tuning the system to a 2:1 resonance frequency ratio between its sense and drive modes, respectively, and by utilizing nonlinear effect known as internal resonance. Ideally this results in a flattop frequency response for the sense mode. In this respect, the objectives of this thesis are to prove the proposed concept utilizing a macro test bed. More specifically we

1. Study and identify the best suited macro proof of concept gyro configuration.
2. Study the nonlinear behaviour of the system.
3. Confirm the theoretical hypothesis using numerical simulation as well as physical experiments in case of 2:1 internal resonance
4. Confirm that under internal resonance, the system can behave as a gyroscope and compare its performance to a linear gyroscope case.
5. Demonstrate the robustness of the sense mode of the proposed design.
6. Establish the basis for bandwidth enhancement using parametric excitation and feedback of nonlinear terms to the drive signal.

As a result, MEMS gyroscope applications such as navigation systems or automotive stability controls that integrate gyroscope's data to obtain angular displacement for orientation estimations will be dramatically influenced by decreasing the need for complex sensor fusion algorithms and accurate electronics.

1.4. Contributions

1. Mathematical modelling and simulation of a nondimensionalized macro-scale gyroscope with 2:1 frequency ratio between its first two natural frequencies. The analytical solution is verified using computer simulations and the nonlinear behavior is proved to enhance performance.

2. A novel gyroscope macro-scale physical design proving the hypothesis.

3. The nondimensionalized mathematical, simulation and physical models will lay the foundation for further research on applying the concept to MEMS scale designs.

4. A novel method has been introduced to increase the sense mode bandwidth through using feedback of the nonlinear coupling terms of the system.

   More publications are expected after submission of a patent, currently in progress through the SFU Innovation Office.

1.5. Thesis Outline

In Chapter 1, a brief historical background and applications of gyroscopes is first provided. After that, literature review is presented on the topic of improving robustness by increasing sense mode bandwidth for Coriolis type gyroscopes.

In Chapter 2, the connection between related previous research utilizing nonlinear internal resonance and saturation and gyroscope models, is established. Multiple analytical and experimental models are summarized with focus on the effects of modal interaction and nonlinear coupling on the frequency response.

In Chapter 3, a simplified lumped-element mathematical model of a T-beam gyroscope is presented. The equations of motion are first derived using Euler-Lagrange's energy method and are then nondimensionalized. Furthermore the equations of motion are scaled to study the effect of the nonlinear terms on the overall performance. Then the approximate analytical solution is given through the perturbation solution. Numerical simulation results are then compared to literature for validating the model. Moreover, the novel hypothesis of increasing bandwidth of the sense mode through feedback of the nonlinear coupling terms is presented.

In Chapter 4, experimental evidence is shown to confirm the analytical results are conversed. Two different macro-scale experimental prototypes are presented: one as a resonator and the other as a gyroscope.

In Chapter 5, the conclusion is stated as well as ideas for future work.

Chapter 2.

Utilizing Internal Resonance in Gyroscope Design

As specified in section 1.3, the goal of this research is to improve the stability and robustness of MEMS gyroscopes by increasing the sense mode's natural frequency bandwidth by tuning the system to a 2:1 resonance ratio between its sense and drive modes, respectively, and nonlinear effects known as internal resonance. In this chapter, we establish the configuration of a gyroscope best suitable to utilize the principle of internal resonance in its operation.

2.1. Coriolis Vibratory Gyroscopes

Coriolis Vibratory Gyroscopes (CVG) forms the most commonly used design principle in current MEMS-based gyroscopes. Over the past few years, multiple MEMS flexure designs have been developed and analyzed to imitate springs. Pisano [41] and Fedder [42] studied the linear and nonlinear analytical models of common suspension/flexure designs used in MEMS, the latter reporting approximately 3% error between the analytical and FEA solutions.

In MEMS CVG design, the crab-leg flexure has been one of the commonly used designs due to its modeling, design and manufacturing simplicity. One acceptable modeling approximation for a single mass CVG uses a simple two degrees of freedom lumped element model as shown in Figure 2-1.

At first, two coordinate frames are assigned, a fixed inertial frame {i} and a rotating frame {g} attached at the center of the gyroscope frame.

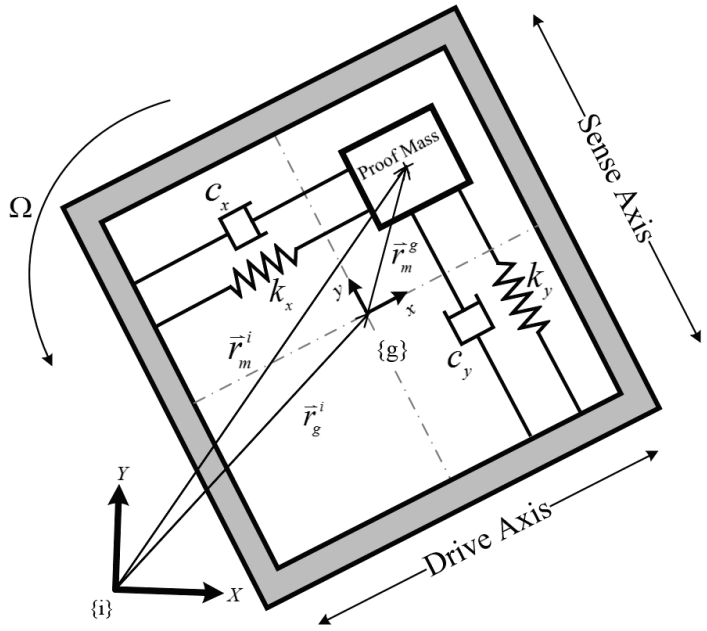

Figure 2-1: Simplified lumped element model for a single mass CVG

The position vector $\vec{r}_m^{\,g}$ of the proof mass with respect to the gyroscope frame is given in Cartesian coordinates as

$$\vec{r}_m^{\,g} = x\,\hat{e}_1 + y\,\hat{e}_2 \tag{2.1}$$

Such that $\hat{e}_1$ and $\hat{e}_2$ are unit vectors along the *x* and *y* axes of the gyroscope frame {g} respectively. Using vector addition we derive the proof mass position with respect to the inertial frame as:

$$\vec{r}_m^{\,i} = \vec{r}_g^{\,i} + \vec{r}_m^{\,g} \tag{2.2}$$

Now using fundamental dynamics theory of rotating frames of reference, the velocity vector of the proof mass with respect to the inertial frame is given by

$$\dot{\vec{r}}_m^{\,i} = \left(\frac{d\,\vec{r}_m^{\,g}}{dt} \right) + \Omega\,\hat{e}_3 \times \vec{r}_m^{\,g} \tag{2.3}$$

Such that Ω is the input angular velocity applied on the gyroscope about the *z* axis. Expanding equation (2.3) we find that the velocity of the proof mass with respect to the inertial frame is

$$\vec{\dot{r}}_m^{\,i} = \left(\dot{x} - \Omega y\right)\hat{e}_1 + \left(\dot{y} + \Omega x\right)\hat{e}_2 \tag{2.4}$$

In order to derive acceleration of the proof mass, equation (2.4) is differentiated with respect to time based on equation (2.3). The acceleration vector is thus found to be

$$\begin{aligned}\vec{\ddot{r}}_m^{\,i} &= \left[\left(\frac{d}{dt}\right)_m^g + \Omega\times\right]\left[\left(\frac{d\vec{r}_m^{\,g}}{dt}\right) + \Omega\hat{e}_3\times\vec{r}_m^{\,g}\right] \\ &= \left(\ddot{x} - \dot{\Omega}y - 2\Omega\dot{y} - \Omega^2 x\right)\hat{e}_1 + \left(\ddot{y} + \dot{\Omega}x + 2\Omega\dot{x} - \Omega^2 y\right)\hat{e}_2\end{aligned} \tag{2.5}$$

The reaction forces acting upon the proof mass due to angular rotation are thus given by

$$\vec{F}_m^i = m\left[\left(\ddot{x} - \dot{\Omega}y - 2\Omega\dot{y} - \Omega^2 x\right)\hat{e}_1 + \left(\ddot{y} + \dot{\Omega}x + 2\Omega\dot{x} - \Omega^2 y\right)\hat{e}_2\right] \tag{2.6}$$

One can classify these forces into three different types:

$$\begin{aligned}\vec{F}_{Coriolis} &= \left(-2m\,\Omega\dot{y}\right)\hat{e}_1 + \left(2m\,\Omega\dot{x}\right)\hat{e}_2 \\ \vec{F}_{Centrifugal} &= \left(-m\,\Omega^2 x\right)\hat{e}_1 - \left(2m\,\Omega^2 y\right)\hat{e}_2 \\ \vec{F}_{Euler} &= \left(-m\,\dot{\Omega}y\right)\hat{e}_1 - \left(m\,\dot{\Omega}x\right)\hat{e}_2\end{aligned} \tag{2.7}$$

Now to consider stiffness and damping effects as well as the harmonic forcing excitation with amplitude *F* and frequency ω_d the equations of motion become

$$\begin{aligned}m\left(\ddot{x} - \dot{\Omega}y - 2\Omega\dot{y} - \Omega^2 x\right) + k_x x + c_x\dot{x} &= F\sin\left(\omega_d t\right) \\ m\left(\ddot{y} - \dot{\Omega}x + \Omega^2 y\right) + k_y y + c_y\dot{y} &= -2m\Omega\dot{x}\end{aligned} \tag{2.8}$$

The term $2\Omega\dot{y}$ can be neglected as the effect of the displacement of the sense axis on the drive displacement is significantly less than vice versa. Also assuming a constant input

angular velocity (i.e. $\dot{\Omega}=0$) the terms $\dot{\Omega}y$ and $\dot{\Omega}x$ can be neglected. Moreover, since the input angular acceleration is almost always less than the drive mode natural frequency, the centripetal acceleration terms $\Omega^2 x$ and $\Omega^2 y$ can also be ignored yielding the equations of motion to be

$$\begin{aligned} m\ddot{x}+k_x x+c_x\dot{x} &= F\sin(\omega_d t) \\ m\ddot{y}+k_y y+c_y\dot{y} &= -2m\Omega\dot{x} \end{aligned} \tag{2.9}$$

Dividing both sides by the proof mass *m* and using the following substitutions

$$\omega_x=\sqrt{\frac{k_x}{m}}\ ;\ \omega_y=\sqrt{\frac{k_y}{m}}\ ;\ \zeta_x=\frac{c_x}{2m\omega_x}\ ;\ \zeta_y=\frac{c_y}{2m\omega_y} \tag{2.10}$$

We get $$\ddot{x}+2\zeta_x\omega_x\dot{x}+\omega_x^2 x=\frac{F}{m}\sin(\omega_d t) \tag{2.11}$$

Such that $\omega_{x,y}$ and $\zeta_{x,y}$ are the drive and sense mode natural frequencies and damping ratios respectively. Give the harmonic forcing nature of the system the solution is expected to also take a harmonic nature as $x(t)=x_o\sin(\omega_d t+\phi)$ (2.12)

Where the amplitude of the response along the *x*-axis is given by [33]

$$x_o=\frac{\left(F_\circ/\omega_x^2\right)}{\left(\left[1-\left(\frac{\omega_d}{\omega_x}\right)^2\right]^2+\left[2\zeta_x\frac{\omega_d}{\omega_x}\right]^2\right)^{1/2}}\quad ;\qquad \phi=\tan^{-1}\left(\frac{2\zeta_x\frac{\omega_d}{\omega_x}}{1-\left(\frac{\omega_d}{\omega_x}\right)^2}\right) \tag{2.13}$$

$$\ddot{y}+2\zeta_y\omega_y\dot{y}+\omega_y^2 y=-2\Omega\omega_d X\cos(\omega_d t+\phi) \tag{2.14}$$

$$Y = \frac{2m\Omega\omega_d X}{k_y\left(\left[1-\left(\frac{\omega_d}{\omega_y}\right)^2\right]^2+\left[2\zeta_y\frac{\omega_d}{\omega_y}\right]^2\right)^{1/2}} \tag{2.15}$$

The equations of motion have been verified by comparison to [1], [43] and [33].

In order to enhance the sensitivity Y/Ω, the drive mode displacement amplitude x_o is required to be maximized and the excitation frequency is matched to both the sense and drive mode natural frequencies (i.e. $\omega_d = \omega_x = \omega_y$) also known as mode-matching.

Next, we look at systems with similar dynamics, and obtain different models from literature mainly developed to study modal interactions and vibration absorption by utilizing internal resonance.

2.2. Modal Interaction in L-shaped two DOF resonator with 1:2 internal resonance

As the scope of this research is to study the nonlinear behavior of CVG gyroscopes, it was found that the research done by Alan G. Haddow [35] [44] on the resonator shown in Figure 2-2 is of evident relevance.

In [44], the macro-scale L-shaped structure, shown in Figure 2-2, was subjected to a harmonic base excitation using an electromagnetic vibration shaker, and the performance of the system in both the linear (Figure 2-3) and nonlinear (Figure 2-4) cases was studied, numerically, experimentally and through perturbation analysis.

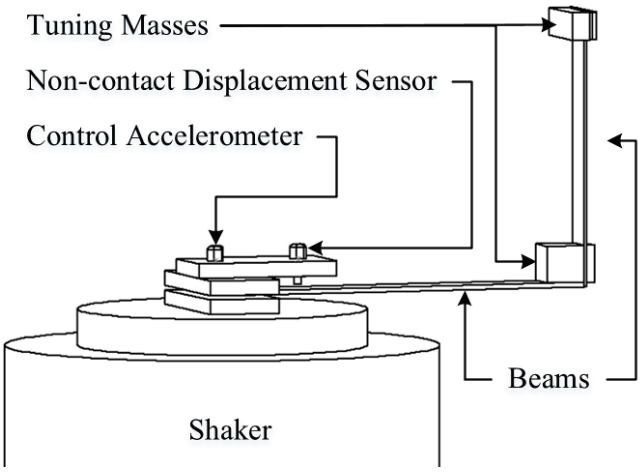

Figure 2-2: A L-beam test-bed setup tuned to 2:1 internal resonance and excited by an electromagnetic shaker[1] [44]

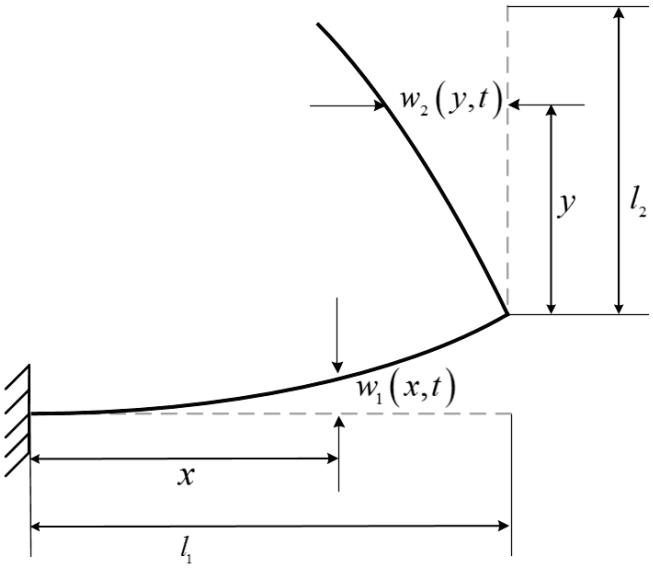

Figure 2-3: Coordinate system for the linear realization of the L-beam[1] [44]

[1] Used with permission, reproduced by author

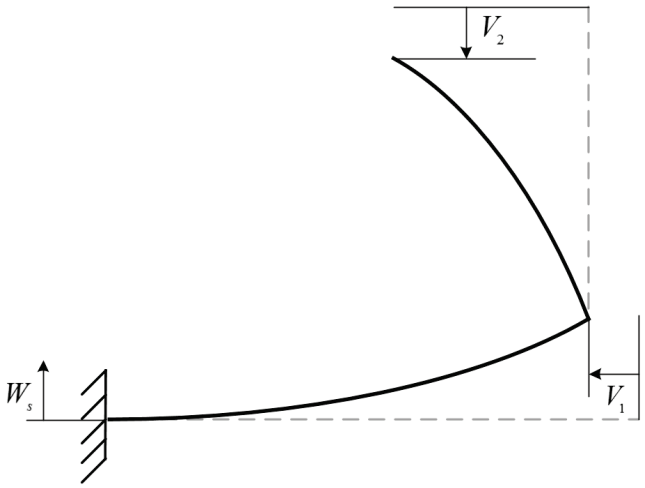

Figure 2-4: Coordinate system for the nonlinear realization of the L-beam[1] [44]

At first, the equations of motion have been derived using Euler-Bernoulli's beam theory combined with Lagrange's energy method. The equations of motion are shown in (2.16) [35].

$$\begin{aligned}
&\begin{bmatrix} \ddot{u}_1 \\ \ddot{u}_2 \end{bmatrix} + \begin{bmatrix} \omega_1^2 & 0 \\ 0 & \omega_2^2 \end{bmatrix} \begin{bmatrix} u_1 \\ u_2 \end{bmatrix} - 2F \begin{bmatrix} K_1 \\ K_2 \end{bmatrix} \cos(\Omega\tau) \\
&\quad + \varepsilon \underline{Y} \begin{bmatrix} \dot{u}_1^2 + u_1\ddot{u}_1 \\ \dot{u}_1\dot{u}_2 + u_1\ddot{u}_2 \\ \dot{u}_1\dot{u}_2 + u_2\ddot{u}_1 \\ \dot{u}_2^2 + u_2\ddot{u}_2 \end{bmatrix} + 2\varepsilon \begin{bmatrix} \mu_1 & 0 \\ 0 & \mu_2 \end{bmatrix} \begin{bmatrix} \dot{u}_1 \\ \dot{u}_2 \end{bmatrix} \\
&\quad + 2\varepsilon F \underline{Z} \left[\Omega\cos(\Omega\tau) \begin{bmatrix} u_1 \\ u_2 \end{bmatrix} + \sin(\Omega\tau) \begin{bmatrix} \dot{u}_1 \\ \dot{u}_2 \end{bmatrix} \right] = \begin{bmatrix} 0 \\ 0 \end{bmatrix}
\end{aligned} \tag{2.16}$$

Such that: u_1 and u_2 are the generalized coordinates corresponding to the primary and secondary beam deflections a_1 and a_2. $\underline{Y}$ and $\underline{Z}$ are matrices composed of nonlinear coefficients and coefficients of parametric terms respectively. Due to the cumbersome nature of the terms, the interested reader is referred to [35] for the detailed listing of parameters. w_s is the base displacement in Figure 2-4 with excitation amplitude F and

[1] Used with permission, reproduced by author

frequency Ω, τ is non-dimensional time, and (.) represents derivative with respect to τ. The quadratic nonlinear terms (Coriolis-like), such as $\dot{u}_1 \dot{u}_2$, represent the generalized velocities for the primary and secondary beams, respectively. The natural frequencies and mode shapes of the systems have been found using Eigen value analysis that closely matched the experimental findings. These terms are also used in the experimental model to amplify the coupling effect between the two degrees of freedom and thus enhancing the bandwidth of higher natural frequency. As part of establishing the background for this study, the mode shapes and natural frequencies obtained using the linearized model were derived and verified using ANSYS™ FEA software, as shown in Figure 2-5.

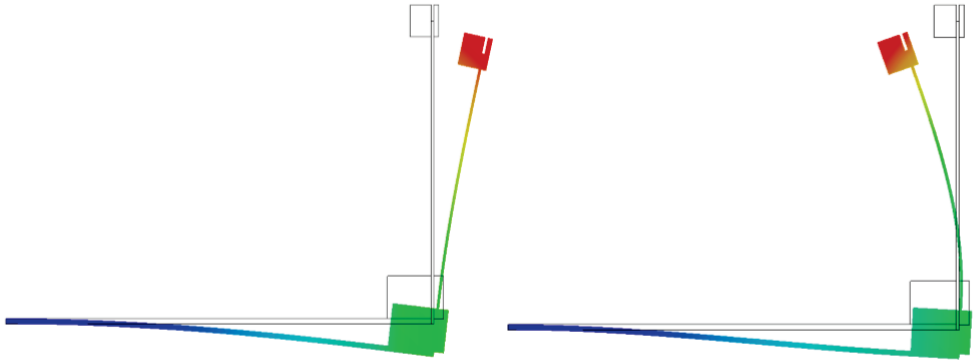

Figure 2-5: The first mode (left) and second mode (right) of the L-beam obtained using ANSYS™ FEA analysis software

2.2.1. Internal Resonance and Saturation

The analytical perturbation solution of the nonlinear equations of motion (2.16) was derived and validated using direct numerical integration, and confirmed results found in [44]. Our approach was based on the method of multiple scales (MMS) developed by Nayfeh [45]. The main focus was to study modal interaction effects on the two DOF L-shaped structure in cases of internal resonance, a nonlinear phenomenon specific to multi-DOF systems [45]. It appears when the natural frequencies of the system are tuned to be in a linear combination. The relation between the natural frequencies can be expressed as:

$$\omega_i = n\,\omega_j \qquad \exists\, i, j, n \in \mathbb{N} \tag{2.17}$$

Such that n is an integer and ω_i and ω_j are natural frequencies of the system.

If a nonlinear system is excited at one of its natural frequencies ω_i, it will not only resonate as explained by linear systems theory, but will also show resonances at multiple/fractions of the excited natural frequency. The focus of this research focuses only on the case when the natural frequency of the drive beam is equal to twice that of the secondary one with a system depicting quadratic nonlinearities. This has been achieved in this specific design by using a thicker drive beam relative to the secondary one [44].

Once the system is tuned to 2:1 internal resonance, an interesting nonlinear effect can be observed. Given that the excitation frequency is fixed at the higher natural frequency, by gradually increasing the excitation amplitude the frequency response curves will show the nonlinear effects on the bandwidth of the resonance peaks. For relatively small excitation amplitudes, the system behaves as predicted by linear theory. After a certain system dependent excitation amplitude threshold, the once linear peak starts to grow in bandwidth and decrease in amplitude as shown in Figure 2-6 such that a_1 and a_2 are the steady state solutions (amplitudes) for the primary and secondary beams respectively. This is when the nonlinear response curves diverge from the expected linear solution.

Another nonlinear phenomena associated with internal resonance is the so-called saturation phenomenon. First illustrated by Nayfeh [46] to analyze modal interaction between a ship's pitch and roll motion. It has been found that modal amplitudes between these two DOF are highly dependent not only on the excitation frequency but also on the excitation amplitude contrary to linear theory. Given that the system contains quadratic nonlinearities, saturation is expected to occur when the drive and sense mode natural frequencies are tuned to 2:1 respectively. Similar to the conditions stated in the previous section, if the excitation frequency is fixed at the higher natural frequency and the amplitude is gradually increased, after an excitation amplitude threshold, the lower mode of vibration is excited. In addition to the increase in bandwidth as state earlier, the modal amplitude of the drive mode "saturates" and an energy bridge starts forming causing the

secondary beam (sense mode) to resonate, as shown in Figure 2-6. Experimental results verifying the saturation phenomenon have been obtained in [35], [44].

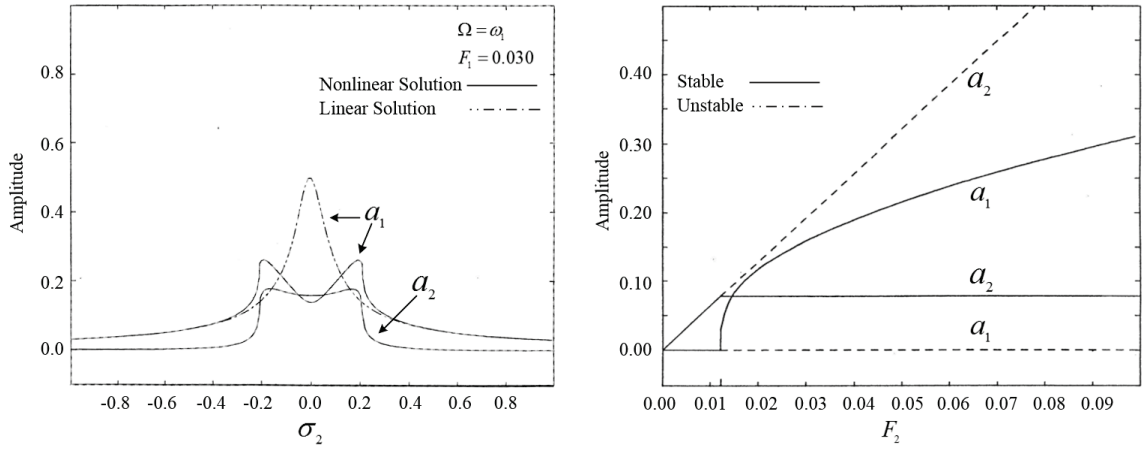

Figure 2-6: Internal resonance and saturation effects on steady state amplitudes as functions of detuning from 2:1 resonance ratio (left) and forcing amplitude (right)[1] [44]

2.3. A two DOF Lumped mass System representing the Gyroscope

Another system similar to the L-beam, is a lumped-element model studied by Tuer *et al.* [39] shown in Figure 2-7 where internal resonance was used for controlling vibrations of a flexible beam using an active tuned controller. The principle objective was once the energy is transferred from a vibrating flexible beam to a secondary rigid one, connected a dc motor was used to actively absorb the vibration. The quadratic coupling nonlinearities in the system, facilitated the transfer of energy between its two modes. The study also highlighted that an actuator could be used to enhance the transfer of energy between two systems.

Due to the complexity of the structure, a lumped-element model mathematical was developed. Considering the center of mass locations, the free body diagram with respect to the inertial frame of reference is shown in Figure 2-8.

[1] Used with permission, reproduced by author

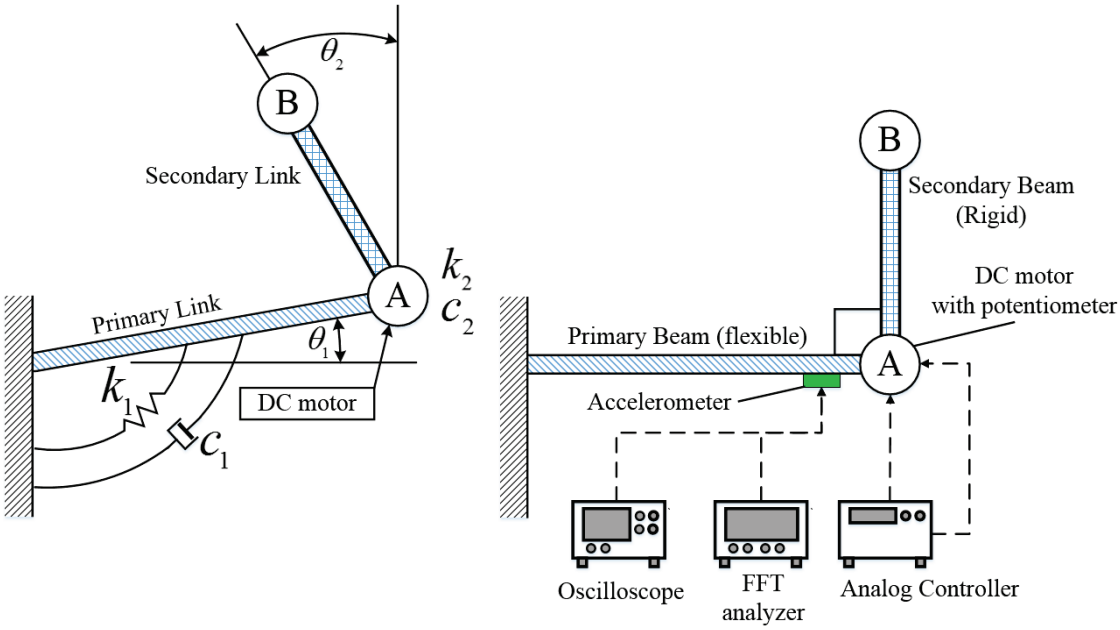

Figure 2-7: An L-beam structure tuned to 2:1 internal resonance between the natural frequencies of its primary and secondary beams, respectively utilizing a DC motor as a vibration absorber, system block diagram (right) and coordinate system (left)[1] [39]

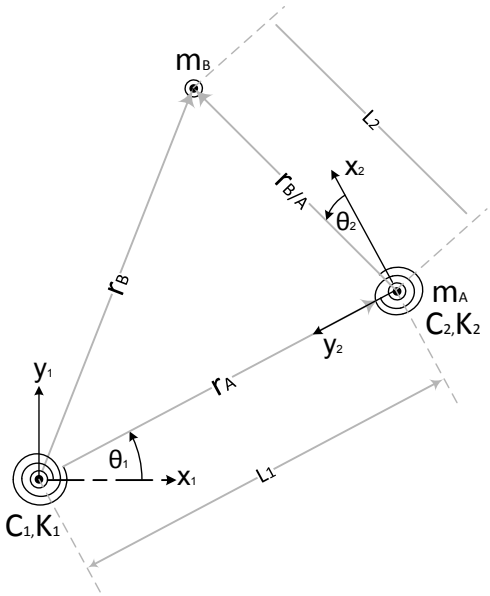

Figure 2-8: Free Body Diagram of the L-beam vibration absorber structure

[1] Used with permission, reproduced by author

In order to follow the Euler-Lagrange equations to derive the equations of motion, we first find the kinetic energy of the system was defined as

$$\begin{aligned} T_{sys} &= \tfrac{1}{2} I_1 \dot{\theta}_1^2 + \tfrac{1}{2}\left(m_2 + m_A + m_B\right) l_1^2 \dot{\theta}_1^2 + \tfrac{1}{2}\left(\tfrac{1}{4} m_2 + m_B\right) l_2^2 \left(\dot{\theta}_1 + \dot{\theta}_2\right)^2 \\ &\quad - \tfrac{1}{2}\left(m_2 + m_B\right) l_1 l_2 \dot{\theta}_1 \left(\dot{\theta}_1 + \dot{\theta}_2\right) \sin\left(\theta_2\right) + \tfrac{1}{2} I_{2/cm} \left(\dot{\theta}_1 + \dot{\theta}_2\right)^2 \end{aligned} \tag{2.18}$$

Such that the mass of moments of inertia of the primary beam (about the base) and the secondary beam (about its centre of gravity) are represented by I_1 and $I_{2/cm}$, respectively. The lengths of the primary and secondary beams are given by l_1 and l_2. The masses of secondary beam, DC motor and secondary beam tip mass are represented by m_2, m_A and m_B, respectively.

The system's total potential energy is $V_{sys} = \tfrac{1}{2} k_1 \theta_1^2 + \tfrac{1}{2} k_2 \theta_2^2$ (2.19)

Now using the Euler-Lagrange procedure, the equations of motion are found to be as [38]

$$\begin{aligned} &\ddot{\theta}_1 + \omega_1^2 \theta_1 + J_{n2} \ddot{\theta}_2 = -2\xi_1 \omega_1 \dot{\theta}_1 + J_{n1}\left(\ddot{\theta}_1 \sin\left(\theta_2\right) + \tfrac{1}{2}\ddot{\theta}_2 \sin\left(\theta_2\right) + \dot{\theta}_1 \dot{\theta}_2 \cos\left(\theta_2\right) + \tfrac{1}{2}\dot{\theta}_2^2 \cos\left(\theta_2\right)\right), \\ &\ddot{\theta}_2 + \omega_2^2 \theta_2 + \ddot{\theta}_1 = -2\xi_2 \omega_2 \dot{\theta}_2 + \tfrac{1}{2} J_{n3}\left(\ddot{\theta}_1 \sin\left(\theta_2\right) - \dot{\theta}_1^2 \cos\left(\theta_2\right)\right) \end{aligned} \tag{2.20}$$

where

$$\begin{aligned} &J_{n1} = \left(m_2 l_1 l_2 + 2 m_B l_1 l_2\right) / \chi_1, \quad J_{n2} = \left(\tfrac{1}{4} m_2 l_1 l_2^2 + m_B l_2^2 + I_{2/cm}\right) / \chi_1 \\ &J_{n3} = \left(m_2 l_1 l_2 + 2 m_B l_1 l_2\right) / \chi_2, \quad \omega_1^2 = k_1 / \chi_1, \quad \omega_2^2 = k_2 / \chi_2 \\ &2\xi_1 \omega_1 = c_1 / \chi_1, \qquad 2\xi_2 \omega_2 = c_2 / \chi_2 \\ &\chi_1 = I_1 + \tfrac{1}{4} m_2 l_2^2 + m_2 l_1^2 + m_B l_2^2 + m_B l_1^2 + m_A l_1^2 + I_{2/cm} \\ &\chi_2 = \tfrac{1}{4} m_2 l_2^2 + m_B l_2^2 + I_{2/cm} \end{aligned}$$

Torsional springs constants are denoted by k_1 and k_2 and viscous damping coefficients by c_1 and c_2 respectively. Separating the linear and nonlinear terms on each side, we get

$$\begin{bmatrix} \chi_1 & \chi_2 \\ \chi_2 & \chi_2 \end{bmatrix} \begin{bmatrix} \ddot{\theta}_1 \\ \ddot{\theta}_2 \end{bmatrix} + \begin{bmatrix} k_1 & 0 \\ 0 & k_2 \end{bmatrix} \begin{bmatrix} \theta_1 \\ \theta_2 \end{bmatrix} = \begin{bmatrix} f \\ g \end{bmatrix} \tag{2.21}$$

The forcing terms is f and g are the remaining nonlinear terms in the equations of motion (2.20). At internal resonance it has been found that damping significantly affects the transfer of energy between the two modes experiencing internal resonance. Based on this fact, a vibration absorber was designed to minimize the vibration in the primary beam [38], [39] by actuating the DC motor to achieve optimal damping. Figure 2-9 shows the frequency response -using FFT- in the case of internal resonance. In the undamped case, a constant-amplitude beat phenomenon was observed due to the transfer of energy from one mode to the other and back given an initial deflection. Damping was then added by matching experimental and simulation results. It can be observed that by tuning the damping to an optimal value (through control) energy can be transferred from the primary beam to the sacrificial one and dissipated before its return.

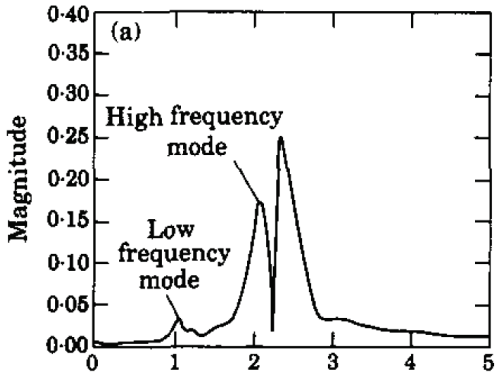

Figure 2-9: Fast Fourier Transform (FFT) of the structure tuned to 2:1 ratio between its first two frequency modes[1] [38]

[1] Used with permission, reproduced by author

2.4. A gyroscopic system based on the L-beam structure

In this section another intensive study of a similar two DOF system is examined with respect to an input angular harmonic excitation. In this case one of the DOFs is translational (i.e. $r_1(t)$) and the other is rotational (i.e. $\theta_1(t)$) as shown in Figure 2-10 [47]. In addition to the excitation forcing function given to the translational DOF, a harmonic rotational one rotates the entire platform using a four-bar linkage mechanism. This rotational excitation will be analogically compared to the input angular rate of gyroscope in later sections.

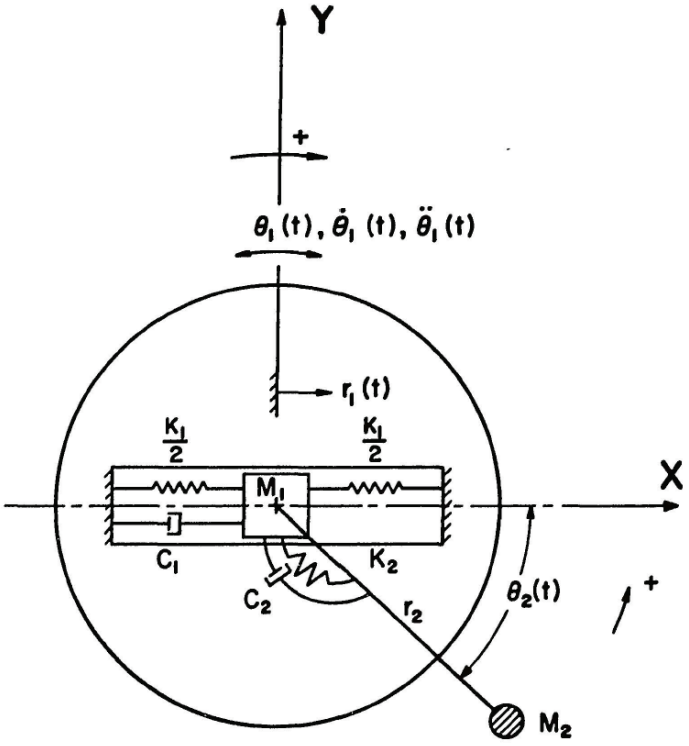

Figure 2-10: Mathematical model for a two degrees of freedom high-speed flexible arm utilizing internal resonance[1] [47]

In addition to studying the nonlinear behavior and saturation in the case of 2:1 internal resonance for the aforementioned system having quadratic nonlinearities, the effect

[1] Used with permission, reproduced by author

of the Coriolis and centripetal forces was taken into consideration. Generally, the equations of motion of a two DOF system, take the form shown as

$$\begin{aligned}\ddot{x}_1 + \omega_1^2 x_1 &= -\gamma_1 \dot{x}_1 + 2\dot{x}_1\dot{x}_2 + F_1 \cos\left(\Omega_1 t + \tau_1\right) \\ \ddot{x}_2 + \omega_2^2 x_2 &= -\gamma_2 \dot{x}_2 + 2\dot{x}_1^2 + F_2 \cos\left(\Omega_2 t + \tau_2\right)\end{aligned} \tag{2.22}$$

Such that $2\dot{x}_1\dot{x}_2$ is the Coriolis-like force induced by the quadratic nonlinearities and $\dot{x}_1^2$ is present in the terms related to centripetal forces due to rotational motion.

The equations of motion of the system were derived to be:

$$\begin{aligned}&\left(m_1 + m_2\right)\ddot{r}_1 + c_1\dot{r}_1 + k_1 r_1 - m_2 r_2\left(\ddot{\theta}_2 \sin\left(\theta_2\right) + \dot{\theta}_2^2 \cos\left(\theta_2\right)\right) \\ &\quad - m_2 r_2\left(\ddot{\theta}_1(t)\sin\left(\theta_2\right) + \dot{\theta}_1^2(t)\cos\left(\theta_2\right) + 2\dot{\theta}_1(t)\theta_2 \cos\left(\theta_2\right)\right) \\ &\quad -\left(m_1 + m_2\right) r_1 \dot{\theta}_1^2(t) = F_r(t) \\ &m_2 r_2^2 \ddot{\theta}_2 + c_2\dot{\theta}_2 + k_2\theta_2 - m_2 r_2 r_1 \sin\left(\theta_2\right) + m_2 r_2 r_1\left(\ddot{\theta}_1(t)\cos\left(\theta_2\right) + \dot{\theta}_1^2 \sin\left(\theta_2\right)\right) \\ &\quad + 2m_2 r_2 \dot{\theta}_1(t)\dot{r}_1 \cos\left(\theta_2\right) = -m_2 r_2^2 \ddot{\theta}_1(t)\end{aligned} \tag{2.23}$$

Such that r_1 and θ_2 are the generalized coordinates, r_2 and θ_1 are given.

The forcing functions are $F_r(t) = A\ \cos(\Omega_r t)$ acting as the translational force and $\theta_1(t) = F_2 \sin(\Omega_\theta t)$ as the rotary one, respectively. As can be seen in the equations of motion (2.23), the nonlinear terms can be divided into two main categories: geometric and kinematic. The geometric nonlinearities include the terms involving $\sin(\theta_2)$ and $\cos(\theta_2)$. The kinematic nonlinear terms on the other hand include velocities represented by $\dot{r}_1$ and $\dot{\theta}_2$ (e.g. $\dot{\theta}_2^2$ involved centripetal acceleration). Also the Coriolis terms show the coupling between the equations of motion such as the $2m_2 r_2 \dot{\theta}_1(t)\dot{r}_1 \cos\left(\theta_2\right)$ term in (2.23).

Rewriting (2.23) in matrix form and separating the linear and nonlinear terms on different sides of the equality leads to:

$$\begin{bmatrix} m_1 + m_2 & 0 \\ 0 & m_2 r_2^2 \end{bmatrix}\begin{bmatrix} \ddot{r}_1 \\ \ddot{\theta}_2 \end{bmatrix} + \begin{bmatrix} k_1 & 0 \\ 0 & k_2 \end{bmatrix}\begin{bmatrix} \dot{r}_1 \\ \dot{\theta}_2 \end{bmatrix} + \begin{bmatrix} c_1 & 0 \\ 0 & c_2 \end{bmatrix}\begin{bmatrix} r_1 \\ \theta_2 \end{bmatrix} = \begin{bmatrix} f \\ g \end{bmatrix} \tag{2.24}$$

Where *f* and *g*, represent the nonlinear terms in the equations of motion. In the following sub-section, the cases of internal resonance and saturation will be shown and later are compared with the proposed mathematical and experimental results for this thesis.

2.4.1. Internal Resonance and Saturation

The nonlinear coupled equations of motion (2.24) were solved using perturbation techniques and verified through direct numerical simulation. The results confirmed the findings in [47]. The nonlinear frequency response function (steady state amplitude response) was then studied in the case of exact internal resonance and the detuned cases, as shown in Figure 2-11. A flattop frequency response can be observed for the second modal amplitude a_2 and a V-shape response for the first modal amplitude a_1. Similar to the previous system, saturation can be observed where the first modal amplitude "saturates" after a certain threshold of forcing amplitude and all energy beyond that threshold is channeled to the second mode.

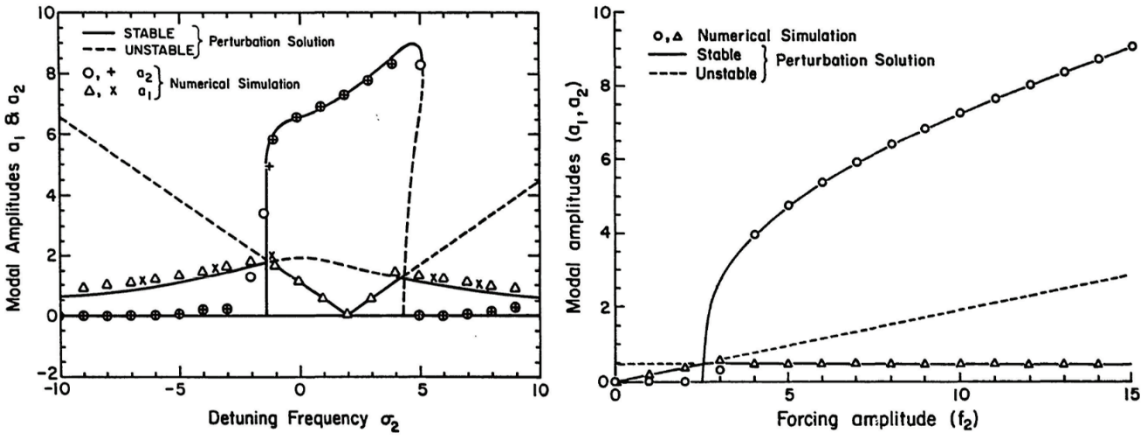

Figure 2-11: Steady state amplitude responses as a function of detuning frequency showing internal resonance (left) and versus excitation amplitude showing saturation (right)[1] [47]

[1] Used with permission, reproduced by author

2.5. Conclusions

This chapter represented three examples with dynamics similar to that of MEMS gyroscopes represented by the equations of motion in (2.8). The nonlinear dynamics associated with these systems are in line with the hypothesis of this research that is *to improve robustness and sensitivity of MEMS gyroscopes, one can increase the sense mode's natural frequency bandwidth by tuning the system to a 2:1 resonance ratio between its sense and drive modes, respectively, through utilizing the nonlinear phenomenon known as internal resonance*.

Chapter 3.

T-beam Structure Mathematical Model

A typical Coriolis vibratory gyroscope is essentially a resonator. Since this research acts as a proof of concept on utilizing internal resonance in modern MEMS gyroscopes, a simple resonator design has been adopted. The T-beam resonator design, shown in Figure 3-1, was influenced by the work shown in [8].

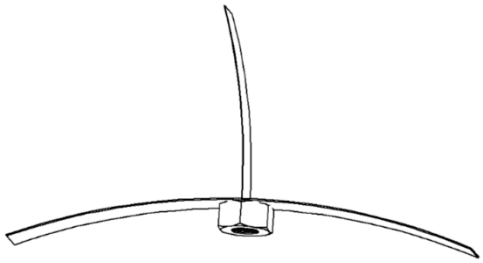

Figure 3-1: T-shaped resonator structure used in this research using two different thicknesses of stainless steel sheet metal and tuning mass

In essence, a T-beam resonator tuned to 2:1 resonance frequency ratio experiences internal resonance resulting in a flattop frequency response at the first "lower" natural frequency. This is represented in the tip displacement of the fixed-free section of the T-beam as shown and the displacement of the center of mass of the fixed-fixed beam as shown in Figure 3-2. *The novelty of this research is in the simplified mathematical model used and the extension of application from a mass sensor to a gyroscope*. The effects of angular velocity on the system dynamics are also discussed in details. In addition, bandwidth and gain enhancement methods are proposed through feedback of the nonlinear coupling terms obtained from the mathematical model.

In this chapter, a mathematical model and numerical simulation of the T-beam structure will be examined under the influence of input angular velocity. The mathematical model uses a simplified lumped-element approach due to firstly the complexity of analysis of such structure as continuous system and secondly that only qualitative results are

required to be compared to experimental results. In addition, at the time of writing, several other common MEMS gyroscope designs are being studied by our research team in the case of internal resonance and compared with the T-beam one.

The nonlinear coupled equations of motion are first derived using Euler-Lagrange equations, and then linearized to study the basic system characteristics. After that the linear and nonlinear responses of the system are compared. Furthermore, the analytical solution is obtained using the two variable expansion perturbation method, for the nondimensionalized scaled nonlinear equations of motion. This approach closely follows the work presented in [47], given that the angular velocity input to the system is constantly compared to a sinusoidal signal.

Once the analytical solution is obtained, it is compared to simulation results and later in the experimental study chapter compared to experimental results. The parameters used in the analytical and numerical solutions are obtained for the experimental test bed for validation purposes.

3.1. T-beam Gyroscope Mathematical Model

Similar to the procedure followed to analyze the L-beam structures in the previous chapter, the lumped mass approach is used for a T-beam structure. The T-beam design uses two flexible sheet metal beams with a suspended tuning mass at the junction as shown in Figure 3-2. The concentrated mass M_1 represents the effective mass attached at the drive beam's center of mass. M_2 represents the effective mass of the clamped-free sense beam and the tuning mass used to achieve the required natural frequency ratio. C_i, K_i are rotational damping coefficients and spring constants respectively.

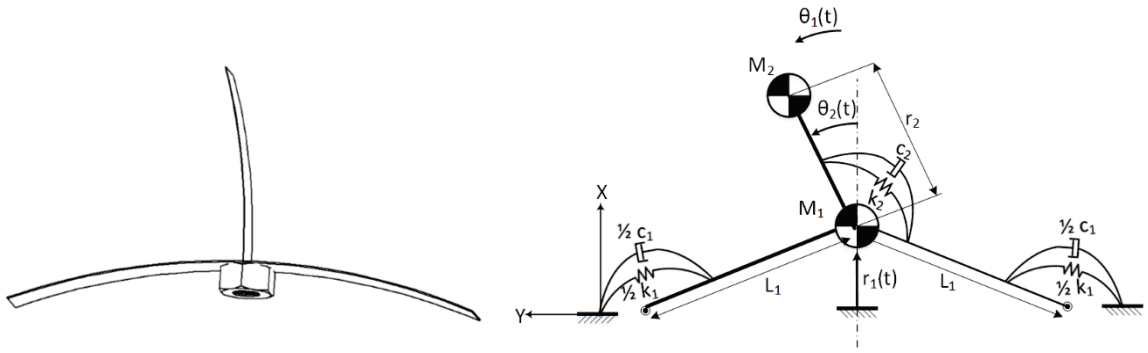

Figure 3-2: T-beam resonator model approximation of the continuous structure (left) by a simplified lumped-element model (right)

The velocities of each of the centers of masses are given by

$$\vec{v}_{m_1} = \dot{r}_1\hat{i} + r_1\dot{\theta}_1\hat{j} \tag{3.1}$$

$$\vec{v}_{m_1} = \left(\dot{r}_1 - r_2\left(\dot{\theta}_1 + \dot{\theta}_2\right)\sin\left(\theta_2\right)\right)\hat{i} + \left(r_1\dot{\theta}_1 + r_2\left(\dot{\theta}_1 + \dot{\theta}_2\right)\cos(\theta_2)\right)\hat{j} \tag{3.2}$$

Such that r_1 is the drive beam center of mass displacement whereas θ_2 and $\dot{\theta}_2$ represent deflection angle and velocity of the sense beam from the vertical axis. $\theta_1, \dot{\theta}_1, \ddot{\theta}_1$ represent the input angular displacement, velocity and acceleration respectively applied to the system. Also r_2 is the length of the sense beam. The kinetic energy of the system can then be shown as

$$\begin{aligned} T_{Total} &= T_{m_1} + T_{m_2} = \tfrac{1}{2} m_1 \dot{r}_{m_1}{}^2 + \tfrac{1}{2} m_2 \dot{r}_{m_2}{}^2 \\ &= \tfrac{1}{2}\left(m_1 + m_2\right) r_1^2 \dot{\theta}_1^2 + \tfrac{1}{2}\left(m_1 + m_2\right)\dot{r}_1^2 + \tfrac{1}{2} m_2 r_2^2 \left(\dot{\theta}_1 + \dot{\theta}_2\right)^2 \\ &\quad + m_2 r_2 \left(\dot{\theta}_1 + \dot{\theta}_2\right)\left(r_1\dot{\theta}_1 \cos(\theta_2) - \dot{r}_1 \sin(\theta_2)\right) \end{aligned} \tag{3.3}$$

and potential energy for the system is

$$V_{System} = V_{\frac{1}{2}k_1} + V_{\frac{1}{2}k_1} + V_{k_2} = \tfrac{1}{2} k_1 \left(\arcsin\left(\frac{r_1}{l_1}\right)\right)^2 + \tfrac{1}{2} k_2 \theta_2^2 \tag{3.4}$$

Such as l_1 is half the drive beam length. Using Euler-Lagrange's formulation, the nonlinear equations of motion were derived as

$$\underline{M}\begin{bmatrix}\ddot{r}_1\\ \ddot{\theta}_2\end{bmatrix}+\underline{C}\begin{bmatrix}\dot{r}_1\\ \dot{\theta}_2\end{bmatrix}+\begin{bmatrix}k_1 & 0\\ 0 & k_2\end{bmatrix}\begin{bmatrix}K_{1,1}\\ \theta_2\end{bmatrix}=\begin{bmatrix}F_{1,1}\\ F_{2,1}\end{bmatrix} \tag{3.5}$$

such that $\underline{M}=\begin{bmatrix}(m_1+m_2) & -m_2 r_2\sin(\theta_2)\\ -m_2 r_2\sin(\theta_2) & m_2 r_2^2\end{bmatrix}$, $\underline{C}=\begin{bmatrix}\dfrac{C_1}{\sqrt{l_1^2-r_1^2}} & 0\\ 0 & C_2\end{bmatrix}$

$$K_{1,1}=\frac{\arcsin\left(\dfrac{r_1}{l_1}\right)}{l_1\left(1-\dfrac{r_1^2}{l_1^2}\right)^{1/2}},\quad F_{1,1}=\begin{pmatrix}m_2 r_2\cos(\theta_2)\left(\dot{\theta}_2^2+\dot{\theta}_1^2\right)+2m_2 r_2\dot{\theta}_1\cos(\theta_2)\dot{\theta}_2\\ +\left(m_1+m_2\right)r_1\dot{\theta}_1^2+F_r(\mathrm{t})\end{pmatrix}$$

$$F_{2,1}=-m_2 r_2 r_1\dot{\theta}_1^2\sin(\theta_2)-2m_2 r_2\dot{\theta}_1\cos(\theta_2)\dot{r}_1$$

3.1.1. Nondimensionalization

In this stage of analysis, new non-dimensional variables are introduced to focus on the nonlinear dynamics irrespective of dimensional scale of the structure. This step will be significant in the near-future phase of utilizing this model in developing MEMS versions of the design. It basically liberates the development from burdens of considering the physical system dimensions and units during the transfer from a macro-scale (on the orders of tens of centimeters) to the micro-scale (on the order of a few micrometers). The dynamics of this model is similar to the system shown in [47].

First Non-dimensional Equation of Motion

As seen in (3.6), ρ_1 represents the non-dimensional driving displacement acting on the mass M_1 and τ is non-dimensional time. That is

$$\rho_1=\frac{r_1}{r_2},\quad r_1=\rho_1 r_2,\quad \tau=\frac{t}{t_c},\quad t=t_c\tau \tag{3.6}$$

Now to proceed to nondimensionalize velocity and acceleration for this generalized coordinate as

$$\frac{\partial r_1}{\partial t}=\frac{\partial r_1}{\partial \tau}\frac{d\tau}{dt}=\frac{\partial\left(\rho_1 r_2\right)}{\partial \tau}\frac{\partial \tau}{\partial t}=r_2\frac{\partial \tau}{\partial t}\frac{\partial \rho_1}{\partial \tau}=r_2\Omega\frac{\partial \rho_1}{\partial \tau}$$
$$\frac{\partial^2 r_1}{\partial t^2}=\frac{\partial}{\partial t}\frac{dr_1}{dt}=\frac{\partial}{\partial \tau}\frac{\partial \tau}{\partial t}\frac{\partial\left(\rho_1 r_2\right)}{\partial \tau}=\Omega\left(r_2\Omega\right)\frac{\partial^2 \rho_1}{\partial \tau^2}=r_2\Omega^2\frac{\partial^2 \rho_1}{\partial \tau^2} \tag{3.7}$$

Following the same method for the input angular velocity to the system, the accompanying non-dimensional parameters become

$$\frac{\partial \theta_1}{\partial t}=\frac{\partial \theta_1}{\partial \tau}\frac{\partial \tau}{\partial t}=\frac{\partial \theta_1}{\partial \tau}\frac{\partial \tau}{\partial t}=\Omega\frac{\partial \theta_1}{\partial \tau}$$
$$\frac{\partial^2 \theta_1}{\partial t^2}=\frac{\partial}{\partial t}\frac{\partial \theta_1}{\partial t}=\frac{\partial}{\partial \tau}\frac{\partial \tau}{\partial t}\frac{\partial \theta_1}{\partial \tau}=\Omega^2\frac{\partial^2 \theta_1}{\partial \tau^2} \tag{3.8}$$

The non-dimensional sense beam deflection angular velocity and acceleration are derived as

$$\frac{\partial \theta_2}{\partial t}=\frac{\partial \theta_2}{\partial \tau}\frac{\partial \tau}{\partial t}=\frac{\partial \theta_2}{\partial \tau}\frac{\partial \tau}{\partial t}=\Omega\frac{\partial \theta_2}{\partial \tau}$$
$$\frac{\partial^2 \theta_2}{\partial t^2}=\frac{\partial}{\partial t}\frac{\partial \theta_2}{\partial t}=\frac{\partial}{\partial \tau}\frac{\partial \tau}{\partial t}\frac{\partial \theta_2}{\partial \tau}=\Omega^2\frac{\partial^2 \theta_2}{\partial \tau^2} \tag{3.9}$$

Isolating the first DOF in (3.5)

$$\left(m_1+m_2\right)\ddot{r}_1+\frac{C_1}{\left(l_1^2-r_1^2\right)^{1/2}}\dot{r}_1+k_1 K_{1,1}-m_2 r_2\sin(\theta_2)\ddot{\theta}_2=\left(m_1+m_2\right)r_1\dot{\theta}_1^2$$
$$+m_2 r_2\left(\dot{\theta}_1^2\cos(\theta_2)+2\dot{\theta}_1^*\dot{\theta}_2\cos(\theta_2)+\dot{\theta}_2^2\cos(\theta_2)\right)+A\cos\left(\omega_r t\right) \tag{3.10}$$

Where: $A=-\left(m_1+m_2\right)r_2\omega_r^2$

Then substituting the obtained non-dimensional variables, the first equation of motion develops into

$$\ddot{\rho}_1 + \frac{\alpha}{(m_1+m_2)\Omega}\dot{\rho}_1 + \frac{k_1 K_{1,1}}{(m_1+m_2)\Omega^2 r_2} - M\sin(\theta_2)\ddot{\theta}_2 =$$
$$\rho_1\Omega^{*2} + M\left(\Omega^{*2}\cos(\theta_2) + 2\Omega^*\dot{\theta}_2\cos(\theta_2) + \dot{\theta}_2^2\cos(\theta_2)\right) \qquad (3.11)$$
$$+F_1\omega_1^2\cos(\Omega_1\tau)$$

Such that $\alpha = \dfrac{C_1}{l_1^2\left(1-\left(\dfrac{\rho_1 r_2}{l_1}\right)^2\right)}$, $M = \dfrac{m_2}{(m_1+m_2)}$, $\dot{\theta}_1^* = \dfrac{\dot{\theta}_1}{\Omega}$, $\Omega_1 = \dfrac{\omega_r}{\Omega}$, $\Omega_2 = \dfrac{\omega_\theta}{\Omega}$

and $F_1 = \dfrac{A}{(m_1+m_2)\Omega^2 r_2}$

The uncoupled natural frequencies of the unforced linear system are:

$$\omega_1 = \left(\frac{K_1}{m_1+m_2}\right)^{1/2} \Big/ \Omega, \qquad \omega_2 = \left(\frac{K_2}{m_2 r_2^2}\right)^{1/2} \Big/ \Omega \qquad (3.12)$$

Second Non-dimensional Equation of Motion

Following the same procedure to nondimensionalize the second equation of motion

$$m_2 r_2^2\ddot{\theta}_2 + C_2\dot{\theta}_2 + k_2\theta_2 - m_2 r_2\ddot{r}_1\sin(\theta_2) = -m_2 r_2 r_1\dot{\theta}_1^2\sin(\theta_2) - 2m_2\dot{r}_1 r_2\dot{\theta}_1\cos(\theta_2) \qquad (3.13)$$

Dividing both sides by $M_2 r_2^2\Omega^2$ and incorporating the non-dimensional parameters obtained previously yields

$$\ddot{\theta}_2 + \gamma_2\dot{\theta}_2 + \omega_2^2\theta_2 - \ddot{\rho}_1\sin(\theta_2) = -\rho_1\Omega^{*2}\sin(\theta_2) - 2\Omega^*\dot{\rho}_1\cos(\theta_2) \qquad (3.14)$$

and nondimensional damping is given by

$$\gamma_1 = \frac{C_1}{l_1^2\left(1-\left(\dfrac{\rho_1 r_2}{l_1}\right)^2\right)(m_1+m_2)\Omega}, \qquad \gamma_2 = \frac{C_2}{m_2 r_2^2\Omega} \qquad (3.15)$$

3.1.2. Scaling

Once the non-dimensional equations of motion are obtained, a small-valued parameter $\varepsilon << 1$ is introduced to study the effects of each of nonlinear and coupling terms. Thus, following change of variables is first introduced

$$\begin{aligned} &F_1 = \varepsilon^k f_1, \qquad \theta_2 = \varepsilon^m \theta, \qquad \rho_1 = \varepsilon^n \rho, \qquad \Omega = \varepsilon^j \omega \\ &\sin(\varepsilon\theta) = \varepsilon\theta, \qquad \cos(\varepsilon\theta) = 1 \end{aligned} \tag{3.16}$$

Such that the orders *j, k, m, n* > *1*, and assuming the following approximations

$$\begin{aligned} &\frac{1}{\left(1-\left(\frac{\rho_1 r_2}{l_1}\right)^2\right)} \simeq 1+\left(\frac{r_2}{l_1}\rho_1\right)^2+\left(\frac{r_2}{l_1}\rho_1\right)^4 \\ &K_{1,1} = \frac{\arcsin\left(\frac{\rho_1 r_2}{l_1}\right)}{\left(1-\left(\frac{\rho_1 r_2}{l_1}\right)^2\right)^{1/2}} \simeq \left(\rho_1\frac{r_2}{l_1}\right)+\frac{2}{3}\left(\rho_1\frac{r_2}{l_1}\right)^3+\frac{8}{15}\left(\rho_1\frac{r_2}{l_1}\right)^5 \end{aligned} \tag{3.17}$$

Scaling of first equation of motion

Applying the approximations from (3.17) to get

$$\begin{pmatrix} \ddot{\rho}_1 + \frac{\left(\frac{c_1}{l_1^2}\right)}{(m_1+m_2)\Omega}\dot{\rho}_1 + \\ \frac{\left(\frac{k_1}{l_1^2}\right)}{(m_1+m_2)\Omega^2}\rho_1 - M\sin(\theta_2)\ddot{\theta}_2 \end{pmatrix} = \begin{pmatrix} \rho_1\Omega^{*2} + F_1\omega_1^2\cos(\Omega_1\tau) + \\ M\left(\Omega^{*2}\cos(\theta_2) + 2\Omega^*\dot{\theta}_2\cos(\theta_2) + \dot{\theta}_2^2\cos(\theta_2)\right) \end{pmatrix} \tag{3.18}$$

And assuming $C_1^* = \frac{c_1}{l_1^2}, \qquad k_1^* = \frac{k_1}{l_1^2}, \qquad \gamma_1 = \frac{C_1^*}{(m_1+m_2)\Omega}, \qquad \omega_1 = \frac{\left(\frac{k_1^*}{m_1+m_2}\right)^{1/2}}{\Omega}$

The result is

$$\ddot{\rho}_1 + \gamma_1\dot{\rho}_1 + \omega_1^2\rho_1 - M\sin(\theta_2)\ddot{\theta}_2 = \rho_1\Omega^{*2} + F_1\omega_1^2\cos\left(\Omega_1\tau\right) + M\left(\Omega^{*2}\cos(\theta_2) + 2\Omega^*\dot{\theta}_2\cos(\theta_2) + \dot{\theta}_2^2\cos\left(\theta_2\right)\right) \tag{3.19}$$

Thus, the scaling transformation of variables are

$$\varepsilon^n\ddot{\rho} + \varepsilon^n\gamma_1\dot{\rho} + \varepsilon^n\omega_1^2\rho - M\varepsilon^{2m}\theta\ddot{\theta} = \varepsilon^{2j+m}\rho\omega^2 + \varepsilon^k f_1\omega_1^2\cos\left(\Omega_1\tau\right) + M\left(\varepsilon^{2j}\omega^2 + 2\varepsilon^{j+m}\omega\dot{\theta} + \varepsilon^{2m}\dot{\theta}^2\right) \tag{3.20}$$

To perturb the system from its linear solution, the orders of ε accompanying linear terms are set to lower than those of the nonlinear terms. Following the same procedure as in [47], the integers j, m, n and k are deduced to control the excitation amplitude.

$$\ddot{\rho} + \gamma_1\dot{\rho} + \omega_1^2\rho - M\varepsilon\theta\ddot{\theta} = \varepsilon^2\rho\omega^2 + \varepsilon^{k-1}f_1\omega_1^2\cos\left(\Omega_1\tau\right) + M\varepsilon\left(\omega^2 + 2\omega\dot{\theta} + \dot{\theta}^2\right) \tag{3.21}$$

Scaling of second equation of motion

Following the same approach, (3.14) will be scaled as:

$$\varepsilon^m\ddot{\theta}_2 + \varepsilon^m\gamma_2\dot{\theta}_2 + \varepsilon^m\omega_2^2\theta_2 - \varepsilon^{n+m}\ddot{\rho}\theta = -\varepsilon^{n+m+2j}\rho\omega^2\theta - 2\varepsilon^{j+n}\dot{\rho} \tag{3.22}$$

Comparing powers of ε in (3.22) and keeping the nonlinear terms one order less than the linear ones [40], The values of integers n, m and j=1 yield the non-dimensional scaled second equation of motion as

$$\ddot{\theta}_2 + \gamma_2\dot{\theta}_2 + \omega_2^2\theta_2 - \varepsilon\ddot{\rho}\theta = -\varepsilon^3\rho\omega^2\theta - 2\varepsilon\dot{\rho} \tag{3.23}$$

Incorporating non-dimensional damping in (3.21) as

$$\gamma_1 = \varepsilon_1\mu_1, \qquad \gamma_2 = \varepsilon_2\mu_2 \tag{3.24}$$

Results in

$$\begin{aligned}\ddot{\rho}+\varepsilon\mu_1\dot{\rho}+\omega_1^2\rho-M\varepsilon\theta\ddot{\theta}&=\varepsilon^2\rho\omega^2+\varepsilon^{k-1}f_1\omega_1^2\cos(\Omega_1\tau)+M\varepsilon\left(\omega^2+2\omega\dot{\theta}+\dot{\theta}^2\right)\\ \ddot{\theta}+\varepsilon\mu_2\dot{\theta}+\omega_2^2\theta-\varepsilon\ddot{\rho}\theta&=-\varepsilon^3\rho\omega^2\theta-2\varepsilon\dot{\rho}\omega\end{aligned} \tag{3.25}$$

3.1.3. The Two-variable Expansion-perturbation Method

The goal of our perturbation analysis is to help in understanding the dynamics of the system near internal or forced resonances. The response is observed in two different time scales (two variable expansion method [48]), a slow time scale η versus a faster one ξ and τ is the independent variable.

$$\xi=\tau, \qquad \eta=\varepsilon\tau \tag{3.26}$$

The idea of this method is to permit the dependent variables ρ and θ to depend explicitly on two time scales: a fast on represented by ξ and a slow one represented by η.

The derivatives of ρ (ξ, η) and θ (ξ, η) are

$$\begin{aligned}\frac{d}{d\tau}&=\alpha\frac{\partial}{\partial\xi}+\varepsilon\frac{\partial}{\partial\eta}\\ \frac{d^2}{d\tau^2}&=\alpha^2\frac{\partial^2}{\partial\xi^2}+2\alpha\varepsilon\frac{\partial^2}{\partial\xi\partial\eta}+O\left(\varepsilon^2\right)\end{aligned} \tag{3.27}$$

And expanding ρ and θ such that

$$\rho=\rho_0+\varepsilon\rho_1+O\left(\varepsilon^2\right), \qquad \theta=\theta_0+\varepsilon\theta_1+O\left(\varepsilon^2\right) \tag{3.28}$$

The different effects when exciting the system at the sense beam natural frequency versus exciting it at the drive beam's one (twice the sense beam's natural frequency) are studied next.

The forced resonance case $\Omega = \omega_1$

Considering that the excitation frequency is close to the drive mode natural frequency

$$\Omega = \omega_1 + \varepsilon\,\sigma_1 \tag{3.29}$$

Choosing $k = 1$ such that $F_1 = \varepsilon f_1$. Substituting (3.27) and (3.28) into (3.25), the for order ε^0 are

$$\rho_{0\xi\xi\xi} + \omega_1^2 \rho_0 = 0, \qquad \theta_{0\xi\xi\xi} + \omega_2^2 \theta_0 = 0 \tag{3.30}$$

And for order ε^1

$$\begin{cases} \rho_{1\xi\xi\xi} + \omega_1^2 \rho_1 = -2\rho_{0\xi\eta} + M\theta_0\theta_{0\xi\xi\xi} + M\left(\theta_{0\xi}\right)^2 - \mu_1\rho_{0\xi} + 2M\omega\theta_{0\xi} + M\omega^2 + f_1\omega_1^2\cos\left(\Omega_1\xi\right) \\ \theta_{1\xi\xi\xi} + \omega_2^2\theta_1 = -2\theta_{0\xi\eta} - \mu_2\theta_{0\xi} + \rho_{0\xi\xi}\theta_0 - 2\omega\rho_{0\xi} \end{cases} \tag{3.31}$$

The solution of the set of equations (3.31) take the general form

$$\begin{aligned} \rho_0 &= K_1(\eta)\sin\left(\omega_1\xi\right) + K_2(\eta)\cos\left(\omega_1\xi\right) \\ \theta_0 &= K_3(\eta)\sin\left(\omega_2\xi\right) + K_4(\eta)\cos\left(\omega_2\xi\right) \end{aligned} \tag{3.32}$$

Then substituting (3.32) into into (3.31) supressing the secular terms associated with $\cos\left(\Omega_1\xi\right)$ where

$$\begin{aligned} \cos\left(\Omega_1\xi\right) = \cos\left(\omega_1\xi + \varepsilon\sigma_1\xi\right) &= \cos\left(\omega_1\xi + \eta\sigma_1\right) \\ &= \cos\left(\omega_1\xi\right)\cos\left(\eta\sigma_1\right) - \sin\left(\omega_1\xi\right)\sin\left(\eta\sigma_1\right) \end{aligned} \tag{3.33}$$

Next, two cases are considered: the *non-resonant case* (i.e. ω_1 is away from $2\omega_2$), and the internal-resonant case $\omega_1 \simeq 2\omega_2$.

The non-resonant case ω_1 ***is away from*** $2\omega_2$

Assuming the following polar transformations

$$K_1(\eta)=a_1\sin(\varphi_1),\ K_2(\eta)=a_1\cos(\varphi_1),\ \ K_3(\eta)=a_2\sin(\varphi_2),\ \ K_4(\eta)=a_2\cos(\varphi_2) \tag{3.34}$$

The secular-term equations are thus obtained as

$$a_{1\eta}=-\frac{\mu_1}{2}a_1+\frac{f_1\omega_1}{2}\sin(\psi),\quad a_{2\eta}=-\frac{\mu_2}{2}a_2,\ \ \psi_\eta=\sigma_1+\frac{f_1\omega_1}{2a_1}\cos(\psi) \tag{3.35}$$

Where $\psi=\sigma_1\eta+\varphi_1,\quad \varphi_2=\text{constant}$.

The equilibrium solution is then derived by equating the right hand side of each equation in (3.35) to zero yielding

$$a_1=\frac{f_1\omega_1}{2\left(\sigma_1^2+\mu_1^2/4\right)^{1/2}},\qquad a_2=0,\qquad \psi=\tan^{-1}\left(\frac{\mu_1}{2\sigma_1}\right) \tag{3.36}$$

Then utilizing the following trigonometric identities

$$\begin{cases}\rho_0=K_1(\eta)\sin(\omega_1\xi)+K_2(\eta)\cos(\omega_1\xi)=a_1\sin(\varphi_1)\sin(\omega_1\xi)+a_1\cos(\varphi_1)\cos(\omega_1\xi)\\ \theta_0=K_3(\eta)\sin(\omega_2\xi)+K_4(\eta)\cos(\omega_2\xi)=a_2\sin(\varphi_2)\sin(\omega_2\xi)+a_2\cos(\varphi_2)\cos(\omega_2\xi)\end{cases} \tag{3.37}$$

We find $$\begin{cases}\rho_0=a_1\cos(\omega_1\xi-\varphi_1)\\ \theta_0=0\end{cases} \tag{3.38}$$

Therefore the steady state solution is given by

$$\begin{cases}\rho=a_1\cos(\omega_1\xi-\varphi_1)+O(\varepsilon^2)=\dfrac{F_1\omega_1\varepsilon^{-1}}{2\left(\sigma_1^2+\mu_1^2/4\right)^{1/2}}\cos(\Omega_1\tau-\psi)+O(\varepsilon)\\ \theta=O(\varepsilon)\end{cases} \tag{3.39}$$

Such that $O(\varepsilon)$ is the linear system solution.

The internal resonance case $\omega_1 = 2\omega_2$

This is the case when ω_1 is very close to 2 ω_2.

$$\omega_1 = 2\omega_2 + \varepsilon\sigma_2 \tag{3.40}$$

And using the following trigonometric identities

$$\begin{cases} \cos(\omega_1\xi) = \cos\left(\left(2\omega_2 + \varepsilon\sigma_2\right)\xi\right) = \cos\left(2\xi\omega_2 + \varepsilon\xi\sigma_2\right) = \cos\left(2\xi\omega_2 + \sigma_2\eta\right) \\ \qquad = \cos\left(2\xi\omega_2\right)\cos\left(\sigma_2\eta\right) - \sin\left(2\xi\omega_2\right)\sin\left(\sigma_2\eta\right) \\ \sin(\omega_1\xi) = \sin\left(\left(2\omega_2 + \varepsilon\sigma_2\right)\xi\right) = \sin\left(2\xi\omega_2 + \varepsilon\xi\sigma_2\right) = \sin\left(2\xi\omega_2 + \sigma_2\eta\right) \\ \qquad = \sin\left(2\xi\omega_2\right)\cos\left(\sigma_2\eta\right) + \cos\left(2\xi\omega_2\right)\sin\left(\sigma_2\eta\right) \end{cases} \tag{3.41}$$

Thus, the steady state amplitude responses with respect to the slowly varying time scale η , in polar form are

$$\begin{cases} a_{1\eta} = \dfrac{m\omega_2^2}{2\omega_1} a_2^2 \sin\left(\psi_2\right) - \dfrac{\mu_1}{2} a_1 + \dfrac{f_1\omega_1}{2}\sin\left(\psi_1\right) \\ a_{2\eta} = -\dfrac{\omega_1^2}{4\omega_2} a_1 a_2 \sin\left(\psi_2\right) - \dfrac{\mu_2}{2} a_2 \\ \varphi_{1\eta} = -\dfrac{m\omega_2^2}{2a_1\omega_1} a_2^2 \cos\left(\psi_2\right) + \dfrac{f_1\omega_1}{2a_1}\cos\left(\psi_1\right) \\ \varphi_{2\eta} = -\dfrac{\omega_1^2}{4\omega_2} a_1 \cos\left(\psi_2\right) \end{cases} \tag{3.42}$$

Where $\psi_1 = \eta\sigma_1 + \varphi_1, \quad \psi_2 = \eta\sigma_2 + 2\varphi_2 - \varphi_1$. Eliminating φ_n from (3.42) we get

$$\begin{cases} a_{1\eta} = \dfrac{m\omega_2^2}{2\omega_1} a_2^2 \sin(\psi_2) - \dfrac{\mu_1}{2} a_1 + \dfrac{f_1\omega_1}{2} \sin(\psi_1) \\ a_{2\eta} = -\dfrac{\omega_1^2}{4\omega_2} a_1 a_2 \sin(\psi_2) - \dfrac{\mu_2}{2} a_2 \\ \psi_{1\eta} = -\dfrac{m\omega_2^2}{2a_1\omega_1} a_2^2 \cos(\psi_2) + \dfrac{f_1\omega_1}{2a_1} \cos(\psi_1) + \sigma_1 \\ \psi_{2\eta} = -\dfrac{\omega_1^2}{2\omega_2} a_1 \cos(\psi_2) + \dfrac{m\omega_2^2}{2a_1\omega_1} a_2^2 \cos(\psi_2) - \dfrac{f_1\omega_1}{2a_1} \cos(\psi_1) + \sigma_2 \end{cases} \tag{3.43}$$

To find equilibrium solutions $a_{i\eta} = \psi_{i\eta} = 0$ in (3.43)

The first case ($a_2 = 0$)

$$a_2 = 0, \quad a_1 = \frac{f_1\omega_1}{2\left(\sigma_1^2 + \dfrac{\mu_1^2}{4}\right)^{\frac{1}{2}}}, \ \psi_1 = -\tan^{-1}\left(\frac{\mu_1}{2\sigma_1}\right), \qquad \psi_2 = arbitrary \tag{3.44}$$

Leading to the solution in (3.45) and (3.46)

$$\begin{aligned} \rho &= \rho_0 + O(\varepsilon) \\ &= \underbrace{K_1(\eta)\sin(\omega_1\xi) + K_2(\eta)\cos(\omega_1\xi)}_{Homogeneous\ Solution} + O(\varepsilon) \\ &= a_1 \sin(\varphi_1)\sin(\omega_1\xi) + a_1 \cos(\varphi_1)\cos(\omega_1\xi) + O(\varepsilon) \\ &= a_1 \cos(\omega_1\xi - \varphi_1) + O(\varepsilon) \\ &= \frac{f_1\omega_1}{2\left(\sigma_1^2 + \mu_1^2/4\right)^{1/2}} \cos(\omega_1\xi - \varphi_1) + O(\varepsilon) \\ &= \frac{F_1\varepsilon^{-1}\omega_1}{2\left(\sigma_1^2 + \mu_1^2/4\right)^{1/2}} \cos(\Omega_1\tau - \psi) + O(\varepsilon) \end{aligned} \tag{3.45}$$

$$\begin{aligned}\theta &= \theta_0 + O(\varepsilon) \\ &= \underbrace{K_3(\eta)\sin(\omega_2\xi) + K_4(\eta)\cos(\omega_2\xi) + O(\varepsilon)}_{\textit{Homogeneous Solution}} \\ &= a_2\sin(\varphi_2)\sin(\omega_2\xi) + a_2\cos(\varphi_2)\cos(\omega_2\xi) + O(\varepsilon) \\ &= 0\end{aligned} \tag{3.46}$$

$$\text{assuming } \begin{cases}\varphi_1 = \psi_1 - \eta\sigma_1 \\ \omega_1\xi - \psi_1 + \eta\sigma_1 = (\omega_1\xi + \eta\sigma_1) - \psi_1 = \Omega_1\xi - \psi_1 = \Omega_1\tau - \psi_1\end{cases} \tag{3.47}$$

This shows that the $O(\varepsilon)$ is the linear solution

$$\begin{cases}\rho = \dfrac{F_1\omega_1\varepsilon^{-1}}{2\left(\sigma_1^2 + \frac{1}{4}\mu_1^2\right)^{1/2}}\cos(\Omega_1\tau - \psi_1) + O(\varepsilon) \\ \theta = O(\varepsilon)\end{cases} \tag{3.48}$$

The second case ($a_1 = -\dfrac{2\mu_1\omega_2}{\omega_1^2 a_1\sin(\psi_2)}$):

$$\begin{cases}a_1 = \dfrac{2\omega_2}{\omega_1^2}\left((\sigma_1 + \sigma_2)^2 + \mu_2^2\right)^{\frac{1}{2}} \\ a_2 = \dfrac{1}{\omega_2}\left[\dfrac{\Gamma_1 \pm \left(f_1^2\omega_1^6 - \Gamma_2^2\right)^{\frac{1}{2}}}{m\omega_1}\right]^{\frac{1}{2}} \\ \psi_1 = \tan^{-1}\left(\dfrac{\mu_2 a_2^2\omega_2^3 + \dfrac{1}{2}\mu_1 a_1^2\omega_1^3}{m\omega_2^3 a_2^2(\sigma_1 + \sigma_2) - \omega_1^3\sigma_1 a_1^2}\right) \\ \psi_2 = \tan^{-1}\left(\dfrac{\mu_2}{\sigma_1 + \sigma_2}\right)\end{cases} \tag{3.49}$$

where $\Gamma_1 = \left(4\sigma_1(\sigma_1 + \sigma_2) - 2\mu_1\mu_2\right)\omega_2, \quad \Gamma_2 = \left(2\mu_1(\sigma_1 + \sigma_2) + 4\mu_1\mu_2\right)\omega_2$

The steady state solution is given by:

$$
\begin{aligned}
\rho &= \rho_0 + O(\varepsilon) \\
&= \underbrace{K_1(\eta)\sin(\omega_1\xi) + K_2(\eta)\cos(\omega_1\xi)}_{\textit{Homogeneous Solution}} + O(\varepsilon) \\
&= a_1\sin(\varphi_1)\sin(\omega_1\xi) + a_1\cos(\varphi_1)\cos(\omega_1\xi) + O(\varepsilon) \\
&= a_1\cos(\omega_1\xi - \varphi_1) + O(\varepsilon) \\
&= \frac{2\omega_2}{\omega_1^2}\left((\sigma_1+\sigma_2)^2 + \mu_2^2\right)^{\frac{1}{2}}\cos(\omega_1\xi - \varphi_1) + O(\varepsilon) \\
&= \frac{2\omega_2}{\omega_1^2}\left((\sigma_1+\sigma_2)^2 + \mu_2^2\right)^{\frac{1}{2}}\cos(\Omega_1\tau - \psi) + O(\varepsilon)
\end{aligned}
\tag{3.50}
$$

And

$$
\begin{aligned}
\theta &= \theta_0 + O(\varepsilon) \\
&= \underbrace{K_3(\eta)\sin(\omega_2\xi) + K_4(\eta)\cos(\omega_2\xi) + O(\varepsilon)}_{\textit{Homogeneous Solution}} \\
&= a_2\sin(\varphi_2)\sin(\omega_2\xi) + a_2\cos(\varphi_2)\cos(\omega_2\xi) + O(\varepsilon) \\
&= \frac{1}{\omega_2}\left[\frac{\Gamma_1 \pm \left(F_1^2\varepsilon^{-2}\omega_1^6 - \Gamma_2^2\right)^{\frac{1}{2}}}{m\omega_1}\right]^{\frac{1}{2}}\cos(\omega_2\xi - \varphi_2)
\end{aligned}
\tag{3.51}
$$

Expanding the variables in (3.50) and (3.51) using

$$
\begin{aligned}
&\omega_1\xi = 2\omega_2\xi + \eta\sigma_2, \quad \omega_2\xi = \frac{1}{2}(\omega_1\xi - \eta\sigma_2) \\
&\omega_1\xi = 2\omega_2\xi + \eta\sigma_2, \quad \omega_2\xi = \frac{1}{2}(\omega_1\xi - \eta\sigma_2) \\
&\psi_2 = \eta\sigma_2 + 2\varphi_2 - \varphi_1, \ \varphi_2 = \frac{1}{2}(\psi_2 + \varphi_1 - \eta\sigma_2) \\
&\psi_1 = \eta\sigma_1 + \varphi_1, \ \varphi_1 = \psi_1 - \eta\sigma_1 \\
&\omega_1\xi - \psi_1 + \eta\sigma_1 = (\omega_1\xi + \eta\sigma_1) - \psi_1 = \Omega_1\xi - \psi_1 = \Omega_1\tau - \psi_1 \\
&\omega_2\xi - \varphi_2 = \frac{1}{2}(\omega_1\xi - \eta\sigma_2) - \frac{1}{2}(\psi_2 + \varphi_1 - \eta\sigma_2) = \frac{1}{2}(\omega_1\xi - \psi_2 - \psi_1 + \eta\sigma_1) \\
&\qquad = \frac{1}{2}(\omega_1\xi - \psi_1 + \eta\sigma_1 - \psi_2) = \frac{1}{2}(\Omega_1\tau - \psi_1 - \psi_2)
\end{aligned}
\tag{3.52}
$$

The steady state response can then be derived as

$$\rho = \frac{2\omega_2}{\omega_1^2}\left(\left(\sigma_1+\sigma_2\right)^2+\mu_2^2\right)^{\frac{1}{2}}\cos\left(\Omega_1\tau-\psi_1\right)+O\left(\varepsilon\right)$$
$$\theta = \frac{1}{\omega_2}\left[\frac{\Gamma_1 \pm \left(F_1^2\varepsilon^{-2}\omega_1^6-\Gamma_2^2\right)^{\frac{1}{2}}}{m\omega_1}\right]^{\frac{1}{2}}\cos\left(\frac{1}{2}\left(\Omega_1\tau-\psi_1-\psi_2\right)\right)+O\left(\varepsilon\right) \tag{3.53}$$

An estimate of the frequency response for each of the two degrees of freedom can be calculated using numerical values obtained from the experimental setup as shown in the table below.

Table 3-1: Numerical values used in numerical simulation

Nondimensionalized Parameter	Symbol	Value/Range
Drive mode natural frequency	ω_1	2
Sense mode natural frequency	ω_2	1
Internal detuning parameter $\omega_1 = 2\omega_2 + \varepsilon\sigma_1$	σ_1	-10 to 10
External detuning parameter $\Omega = \omega_1 + \varepsilon\,\sigma_1$	σ_2	0
Drive mode damping	μ_1	0.69
Sense mode damping	μ_2	2.58
Forcing amplitude	f_1	0.1 to 5

Applying these parameters into the two cases from equation (3.44) and (3.49) the approximate frequency response behavior can be captured. As can be observed in Figure 3-3, the drive mode response in the first case depicts a linear behaviour in the frequency domain, it shows a single sharp peak with no frequency split. The second case however acts nonlinearly.

More importantly, the sense beam deflection is shown to increase in bandwidth as excitation amplitude is increased as seen in Figure 3-4. These results illustrate the hypothesis of increasing a gyroscope's sense mode bandwidth. The perturbation solution obtained here qualitatively match literature sources shown previously despite the differences in the structure of the two degrees of freedom models.

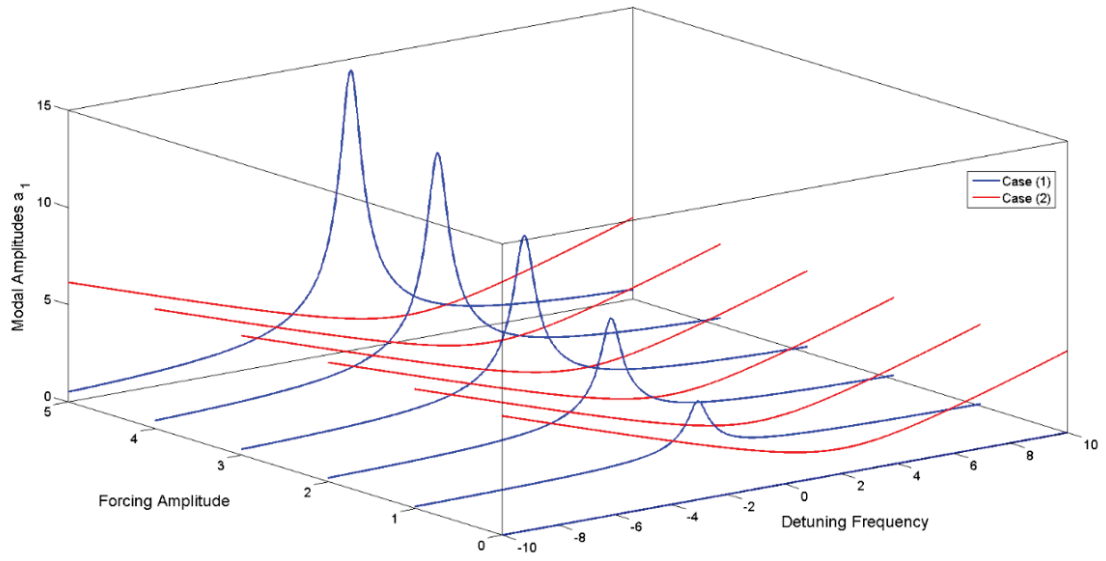

Figure 3-3: Drive mode frequency response perturbation solution as a function of detuned excitation frequency and amplitude

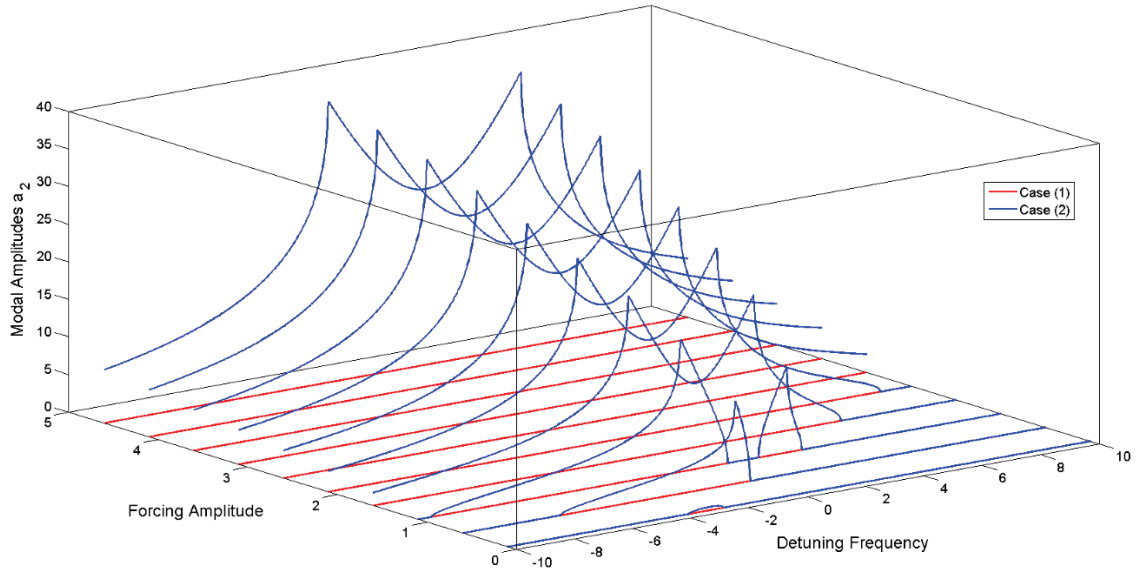

Figure 3-4: Sense mode frequency response perturbation solution as a function of detuned excitation frequency and amplitude

3.1.4. Simulation Results for the Gyroscope's Mathematical Model

This section discusses the simulation results regarding the effect of angular velocity on the responses in both degrees of freedom of the system. This is done to establish the proof of concept for the application of the T-beam structure as a simple gyroscope. These results are later qualitatively compared to the experimental counterparts in later sections. Input angular velocity is simulated as a ramp function with 0.001 $\deg/s^2$ acceleration. The system is harmonically excited with various excitation amplitudes at the lower natural frequency (i.e. sense mode) expecting a linear system behaviour and the higher natural frequency as the nonlinear case. This can clearly show the difference between both cases without changing the structural dimensions.

Linear case $\Omega = \omega_2$

Given that the excitation frequency is set to the lower natural frequency, an overall linear system response is expected. Figure 3-5 shows the displacement and velocity responses along the drive and sense beam directions respectively set against input angular velocity.

An interesting effect can be observed in the drive beam deflection r_1, an increasing drift can be noticed as input angular velocity increases. It can be considered that the centrifugal force generates this drift. The same effect is documented in the experimental section, it shows how this drift can overcome the forcing amplitude at higher angular velocities limiting the measurement range of the sensor. Feedback control of the drive amplitude can be used to mitigate this drift. However, as it falls out of the scope of this study it has been postponed to future work.

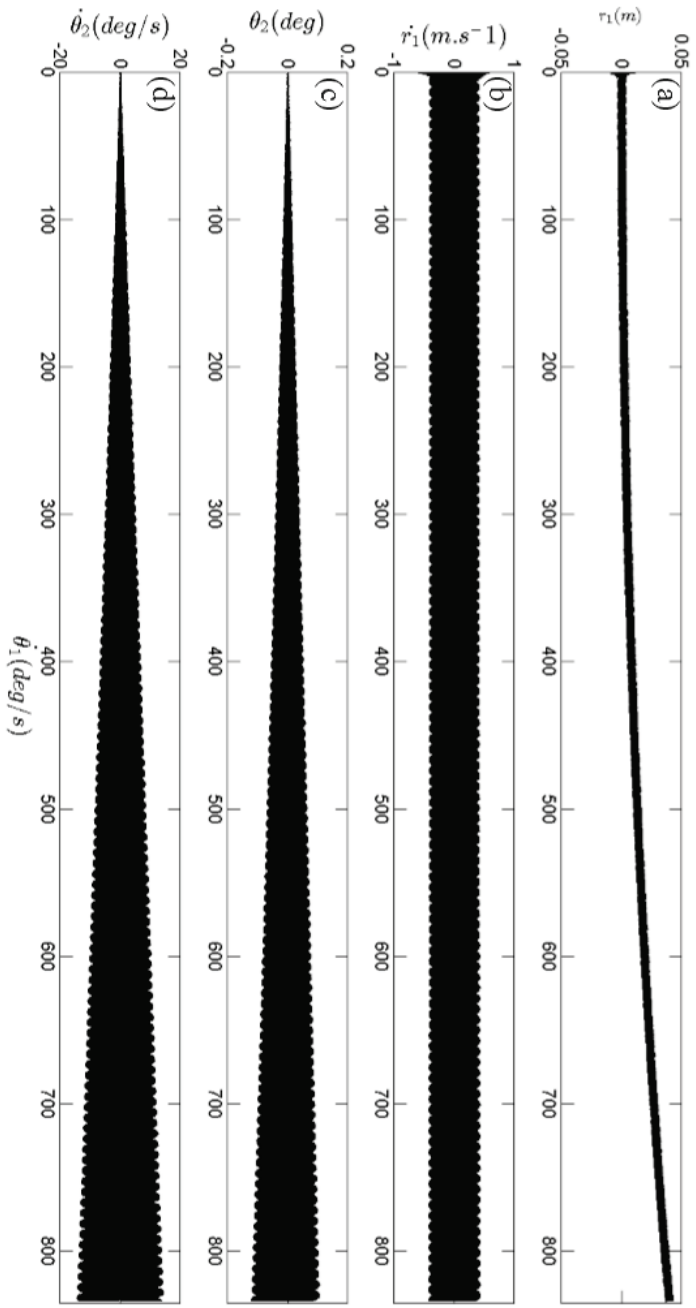

Figure 3-5: Numerical simulation results illustrating the effect of angular velocity on the T-beam gyroscope in the linear case (excitation frequency close to the sense mode natural frequency), (a, b) drive beam displacement and velocity, (c, d) sense beam deflection and velocity

On the other hand, deflection of sense beam (i.e. θ_2) showed a linear response up to a certain threshold of angular velocity. The effect of increasing excitation amplitude is shown in Figure 3-6. As expected, sensitivity increases by increasing the forcing amplitude. Nevertheless, the drifting effect due to the centrifugal force observed from the time domain response on the drive beam can also be seen at higher angular velocities. It results in a negative slope of amplitude response versus angular velocity. This produces a challenge in detecting two different angular velocities on both sides of the threshold. Nonetheless, it is not expected in fully symmetric designs such crab-leg or H-type structures.

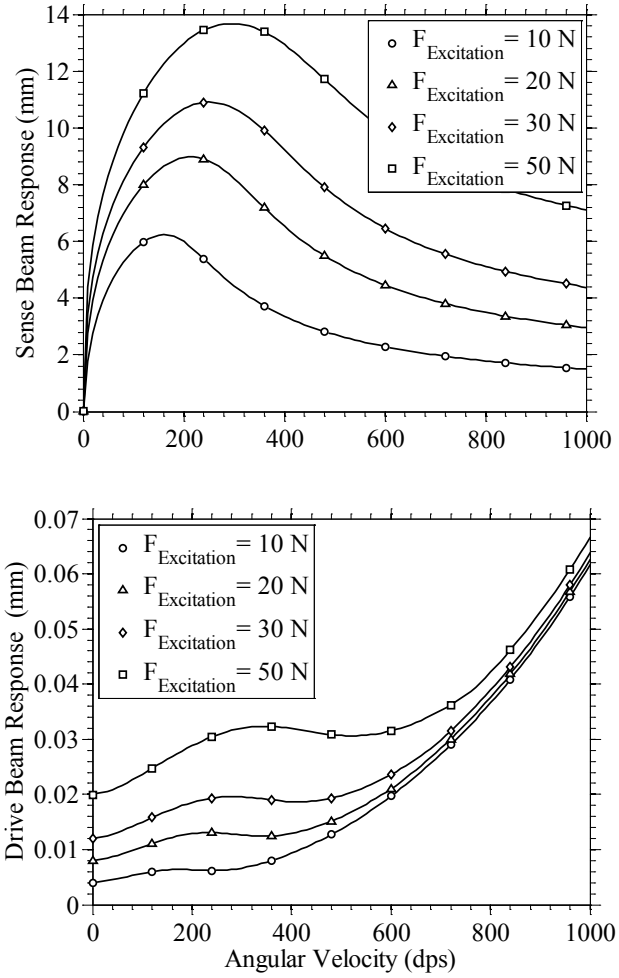

Figure 3-6: Numerical simulation results for the sense beam deflection (top) and drive beam deflection (bottom) deflection in the linear case given various excitation amplitudes

Nonlinear case $\Omega = \omega_1 = 2\omega_2$

Similar to the linear case, a significant drift in the drive beam direction can be observed at higher angular velocities as illustrated in Figure 3-7. In addition, a transfer of energy can be observed between the drive and sense modes (r_1 and θ_2) respectively. This resulted in the sense beam amplitude larger than that in the linear case by approximately an order of magnitude. Also a time lag can be observed between the start of excitation until the sense beam reaches its steady state value. This time-lag was observed to decrease by increasing excitation amplitude in both simulation and experimental results.

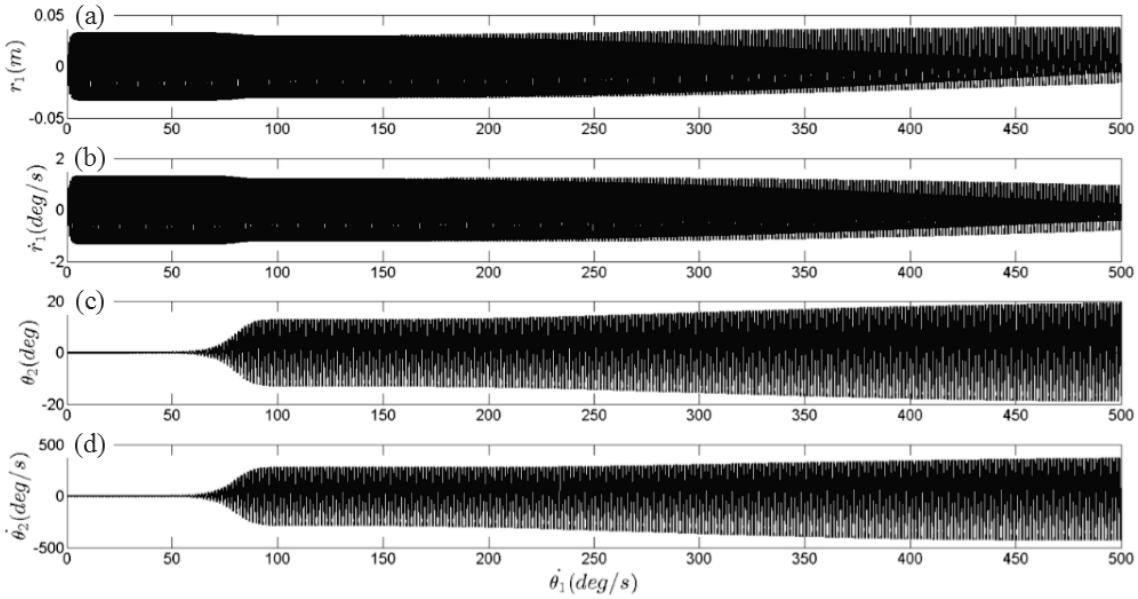

Figure 3-7: Numerical simulation results illustrating the effect of angular velocity on the T-beam gyroscope in the nonlinear case (excitation frequency close to the drive mode natural frequency)

A strong linear relation between the sense beam amplitude responses versus angular velocity can be observed with lower excitation amplitudes as shown inset in Figure 3-8. This relation continues until a certain excitation amplitude threshold defined in the saturation section later. Moreover, significantly higher sensitivities can be achieved by feedback control applied at excitation amplitudes such the one depicted by red in the same figure. This poses a strong novel research topic for future work.

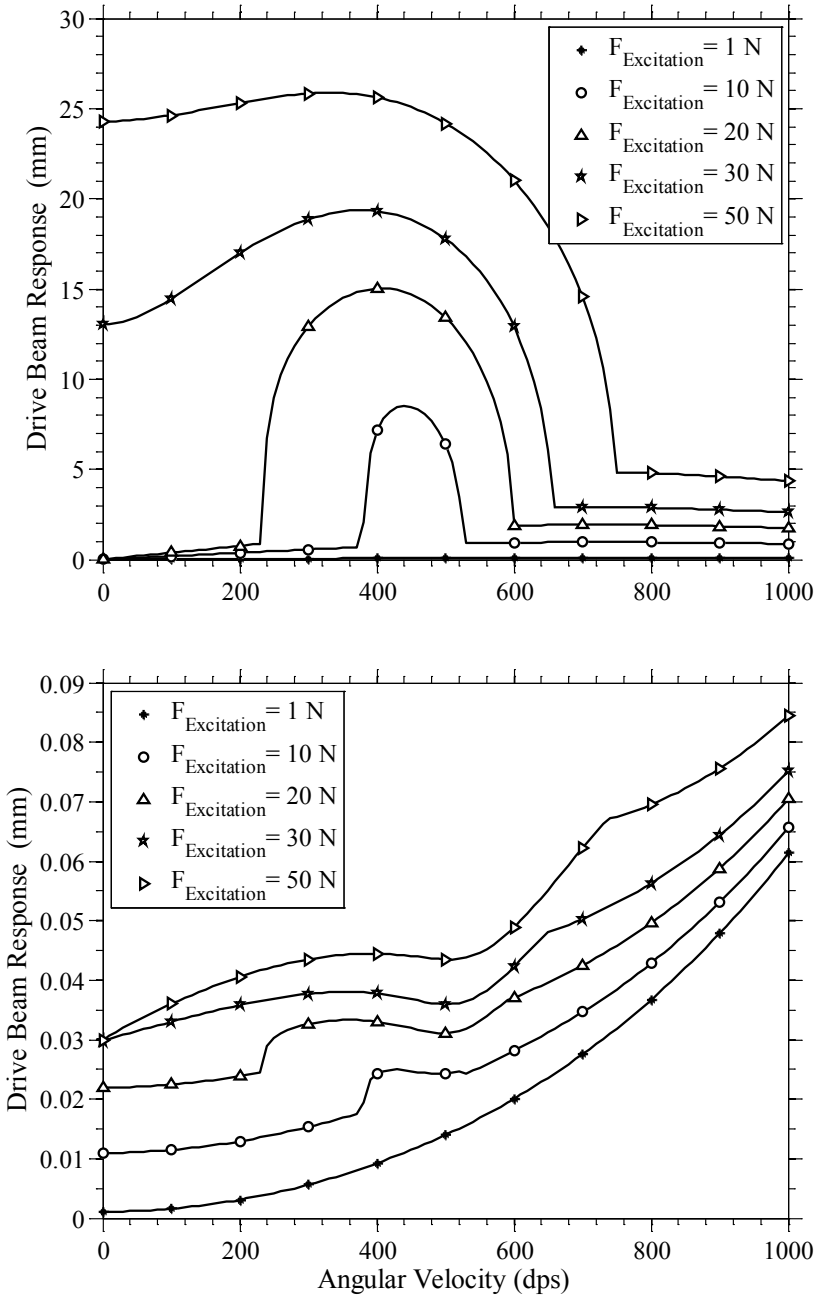

Figure 3-8: Simulation results for the sense mode (top) and drive mode (bottom) displacement in the nonlinear case given various excitation amplitudes

3.2. T-shaped Resonator Mathematical Model

Modelling the same structure as a pure resonator, the only excitation signal is applied to the horizontal clamped-clamped beam and the deflection of the clamped-free vertical beam resembles the sensing element. Both drive and sense beams are approximated to be massless beams with concentrated effective masses [49].

We consider modeling the structure as a resonator is a special case of the detailed model derived in the previous section for a gyroscope. Particularly by assigning no input angular velocity to the system the equations of motion can be considered to be:

$$\begin{aligned}
&\left(M_1+M_2\right)\ddot{r}_1+C_1^*\dot{r}_1+k_1\left(\frac{\arcsin\left(\frac{r_1}{l_1}\right)}{l_1\sqrt{1-\frac{r_1^2}{l_1^2}}}\right)-M_2r_2\left(\ddot{\theta}_2\sin(\theta_2)+\dot{\theta}_2^2\cos(\theta_2)\right)=A\cos\left(\Omega_r t\right)\\
&M_2r_2^2\ddot{\theta}_2+C_2\dot{\theta}_2+k_2\theta_2-M_2r_2\ddot{r}_1\sin(\theta_2)=0
\end{aligned} \tag{3.54}$$

$$\text{Assuming: } \Delta\theta_{spring}=\sin^{-1}\left(r_1/l_1\right),\ \Delta\dot{\theta}_{damper}=\dot{r}_1\Big/\left(l_1\sqrt{1-\left(r_1/l_1\right)^2}\right)$$

Following the same approach the final equations of motion can be derived as:

$$\begin{cases}
\rho=\dfrac{2\omega_2}{\omega_1^2}\left(\left(\sigma_1+\sigma_2\right)^2+\mu_2^2\right)^{\frac{1}{2}}\cos\left(\Omega_1\tau-\psi_1\right)+O\left(\varepsilon\right)\\
\theta=\dfrac{1}{\omega_2}\left[\dfrac{\Gamma_1\pm\left(F_1^2\varepsilon^{-2}\omega_1^6-\Gamma_2^2\right)^{\frac{1}{2}}}{m\omega_1}\right]^{\frac{1}{2}}\cos\left(\dfrac{1}{2}\left(\Omega_1\tau-\psi_1-\psi_2\ \right)\right)+O\left(\varepsilon\right)
\end{cases} \tag{3.55}$$

3.2.1. Simulation Results for the Resonator Mathematical Model

Using small angle approximation the equations of motion (3.54) can be expressed as:

$$\left(M_1+M_2\right)\ddot{r}_1+C_1^*\dot{r}_1+k_1\left(\frac{\arcsin\left(\frac{r_1}{l_1}\right)}{l_1\sqrt{1-\frac{r_1^2}{l_1^2}}}\right)-M_2r_2\underbrace{\left(\ddot{\theta}_2\theta_2+\dot{\theta}_2^2\right)}_{\textit{Quadratic Nonlinearities}}=F_r(\mathrm{t})=A\cos\left(\Omega_r t\right)$$

$$M_2r_2^2\ddot{\theta}_2+C_2\dot{\theta}_2+k_2\theta_2-M_2r_2\ddot{r}_1\theta_2=0$$

The mass matrix remains the same as in (3.5) yields the first two natural frequencies as:

$$\omega_1=\sqrt{\frac{k_1}{\left(M_1+M_2\right)}},\qquad\qquad \omega_2=\sqrt{\frac{k_2}{\left(M_2r_2^2\right)}} \tag{3.56}$$

The energy transfer between the drive and sense modes is then studied. A slowly varying frequency sweep is applied to the system as a forcing function on the drive (r_1) degree of freedom. As the forcing frequency approaches the higher natural frequency, energy transfer between the two modes is expected. However, as can be seen in Figure 3-9a, this energy transfer is unobservable in the case of lower excitation amplitudes. Nevertheless, as observed in Figure 3-9 subplots (b) through (d), as the excitation amplitude is increased the coupling between the two modes increases spanning over a larger time interval.

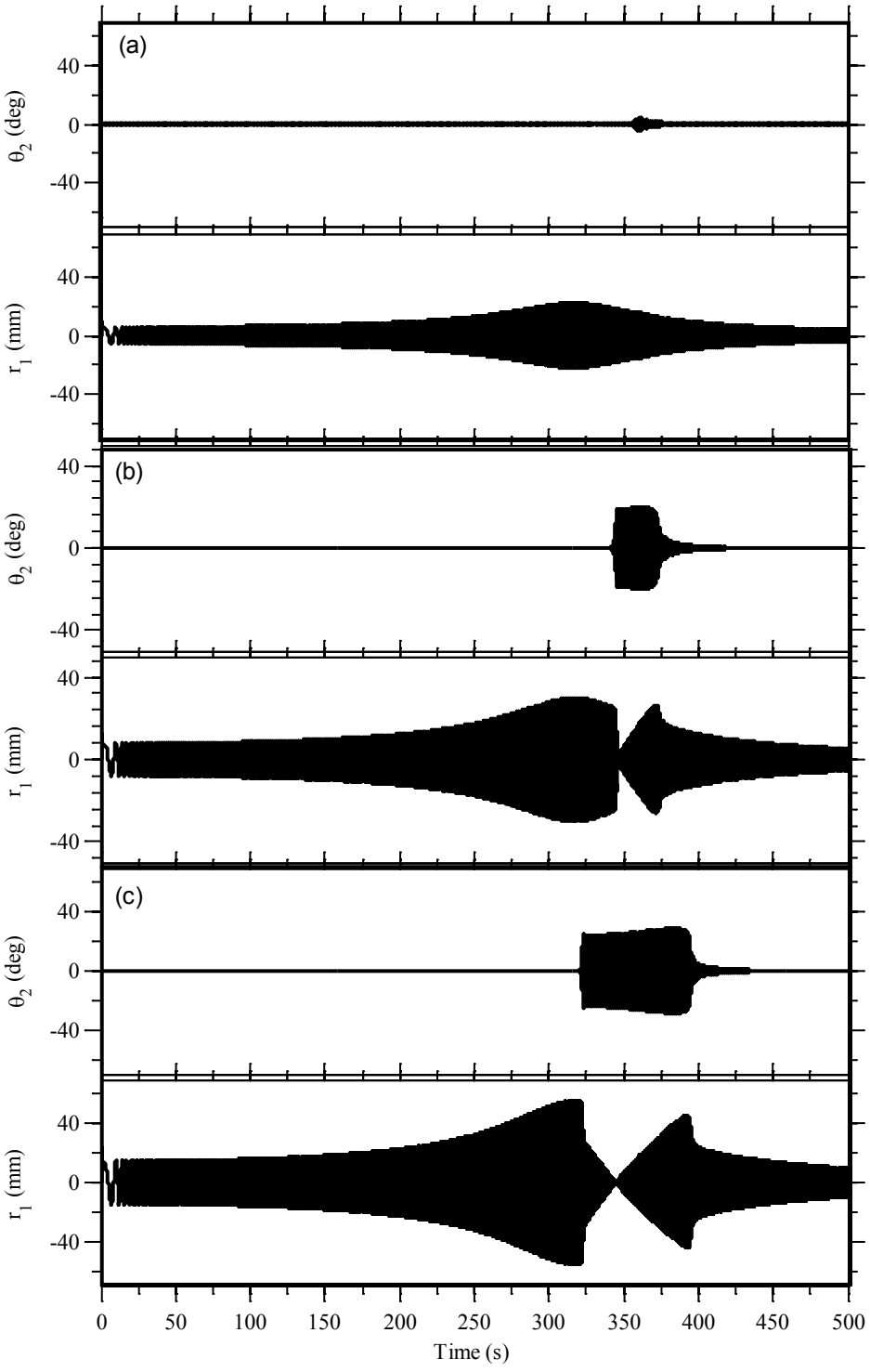

Figure 3-9: Time domain response shows the energy transfer between the drive beam and the sense beam for different excitation amplitudes (a-c)

Common to characterizing a nonlinear system's frequency response, the steady state amplitude of the time response for a given excitation frequency. After that the excitation frequency is changed (incremented in case of an up-sweep or decremented in case of a down-sweep) and the new steady state amplitude is logged and the process repeats over the frequency range of interest. In the case of this model, this process can be done by exciting the system using what is called a "stair case" signal with special care that the duration of each step takes the proper time for the system to reach steady state. Unfortunately, the steady state time varies with multiple variables including excitation amplitude, coupling effects and damping which is extremely challenging to model. This leads to either inaccuracies in determining the nonlinear frequency response function (FRF) and prolonged simulation times. An acceptable replacement method is input a chirp signal -swept cosine- and to capture the envelope of the time response as showed previously in Figure 3-9 after passing through a linear phase filter with cutoff frequencies around the range of interest. After that, the frequency sweep is repeated at different excitation amplitudes to show the evolution of the bandwidth and gain of the sense and drive modes in the frequency domain as shown in Figure 3-10 and Figure 3-11 respectively. As illustrated in red, the frequency response acts similar to a linear one with lower excitation amplitudes. However, in the sense mode the bandwidth and gain increase with reaching a flattop response as excitation amplitude increases. This behavior is very well suited for all resonator applications as it immunizes the system in case either the excitation or the natural frequencies are shifted due to design imperfections.

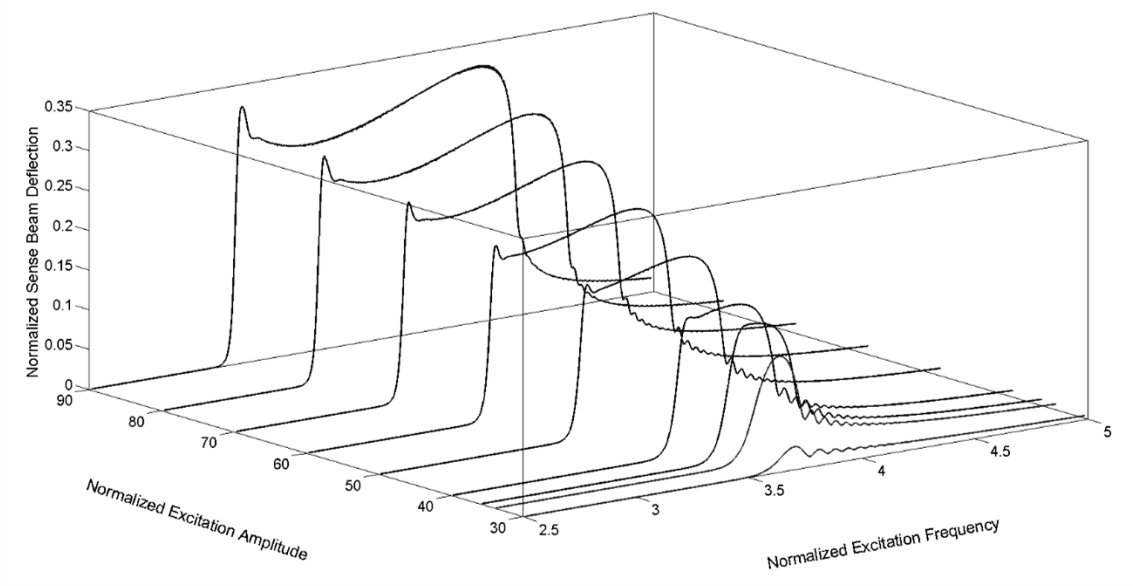

Figure 3-10: Sense beam normalized frequency response showing the increase in the sense mode frequency peak bandwidth proportional to excitation amplitude

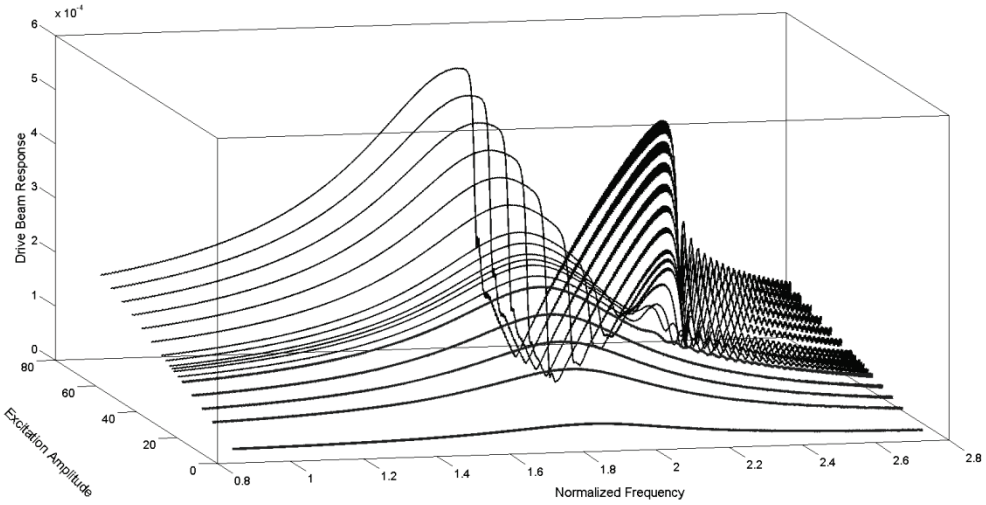

Figure 3-11: Drive beam normalized frequency showing a frequency split increasing proportional to the increase in excitation amplitude

Saturation

Given that the system is tuned to 2:1 ratio and excited at its second mode, the saturation phenomenon occurs after increasing the excitation amplitude beyond a certain threshold. Before that threshold is exceeded, only the drive beam is excited and the system behaves linearly. However, after this excitation threshold is surpassed, the energy is channeled to the sense mode and excites at its natural frequency (i.e. half the drive mode frequency) as shown Figure 3-12Error! Reference source not found..

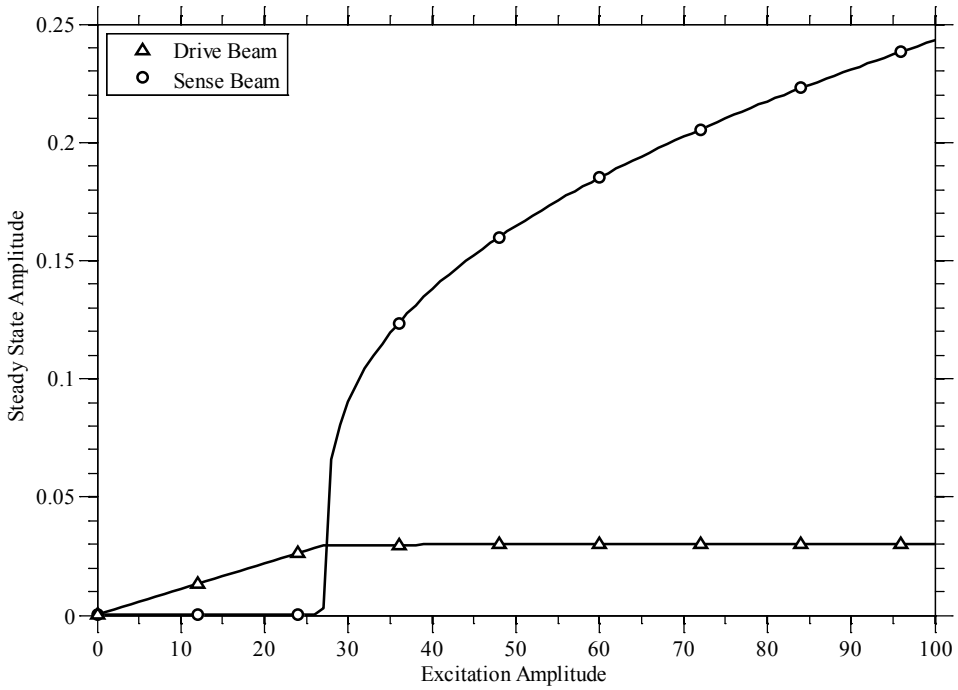

Figure 3-12: Numerical simulation results showing the nonlinear saturation phenomena for the T-beam structure. Energy is transferred from the drive beam to the sense beam after exceeding a specific excitation amplitude threshold

The above presented results for the resonator match the experimental ones in Chapter 4 and literature [8], [38], [39], [44], [47] verifying the validity of the simplified lumped mass model used in this research.

In addition, the overall system bandwidth and gain can be further improved through feedback on the nonlinear coupling terms stated previously in the equations of motion as will be discussed next.

3.3. Feedback Control for Bandwidth and Gain Improvement

Recalling the equations of motion for the resonator (3.54), five coupling terms arise as shown below:

$$\begin{bmatrix} (m_1+m_2) & 0 \\ 0 & m_2 r_2^2 \end{bmatrix}\begin{bmatrix} \ddot{r}_1 \\ \ddot{\theta}_2 \end{bmatrix}+\begin{bmatrix} \dfrac{C_1}{l_1^2\left(1-\left(\frac{r_1}{l_1}\right)^2\right)} & 0 \\ 0 & C_2 \end{bmatrix}\begin{bmatrix} \dot{r}_1 \\ \dot{\theta}_2 \end{bmatrix}+\begin{bmatrix} k_1 & 0 \\ 0 & k_2 \end{bmatrix}\begin{bmatrix} \left(\arcsin\left(\frac{r_1}{l_1}\right)\right)\left(\dfrac{1}{l_1\sqrt{1-\frac{r_1^2}{l_1^2}}}\right) \\ \theta_2 \end{bmatrix}$$

$$= \begin{bmatrix} K_A\underbrace{\left(m_2 r_2 \ddot{\theta}_2 \sin(\theta_2)\right)}_{Coupling\ term\ 1}+K_B\underbrace{\left(2m_2 r_2 \Omega \dot{\theta}_2 \cos(\theta_2)\right)}_{Coupling\ term\ 2}+K_C\underbrace{\left(m_2 r_2 \cos(\theta_2)\dot{\theta}_2^2\right)}_{Coupling\ term\ 3} \\ +K_D\underbrace{\left(m_2 r_2 \cos(\theta_2)\Omega^2\right)}_{Coupling\ term\ 4}+(m_1+m_2)r_1\Omega^2+F_r(\mathrm{t}) \\ K_A\underbrace{\left(m_2 r_2 \ddot{r}_1 \sin(\theta_2)\right)}_{Coupling\ term\ 1}-K_B\underbrace{\left(2m_2 r_2 \Omega \dot{r}_1 \cos(\theta_2)\right)}_{Coupling\ term\ 2}+K_E\underbrace{\left(-m_2 r_2 r_1 \Omega^2 \sin(\theta_2)\right)}_{Coupling\ term\ 5} \end{bmatrix}$$

Studying the effect of each of the coupling terms, the gains K_A through K_E are multiplied to each of the terms respectively. Simulation results showed that the coupling terms $K_A m_2 r_2 \ddot{\theta}_2 \sin(\theta_2)$ and $K_C m_2 r_2 \cos(\theta_2)\dot{\theta}_2^2$ pose immediate effects on the system's performance. As shown in Figure 3-13, K_A has directly proportional effect on the sense mode bandwidth and relatively weaker effect on the drive mode.

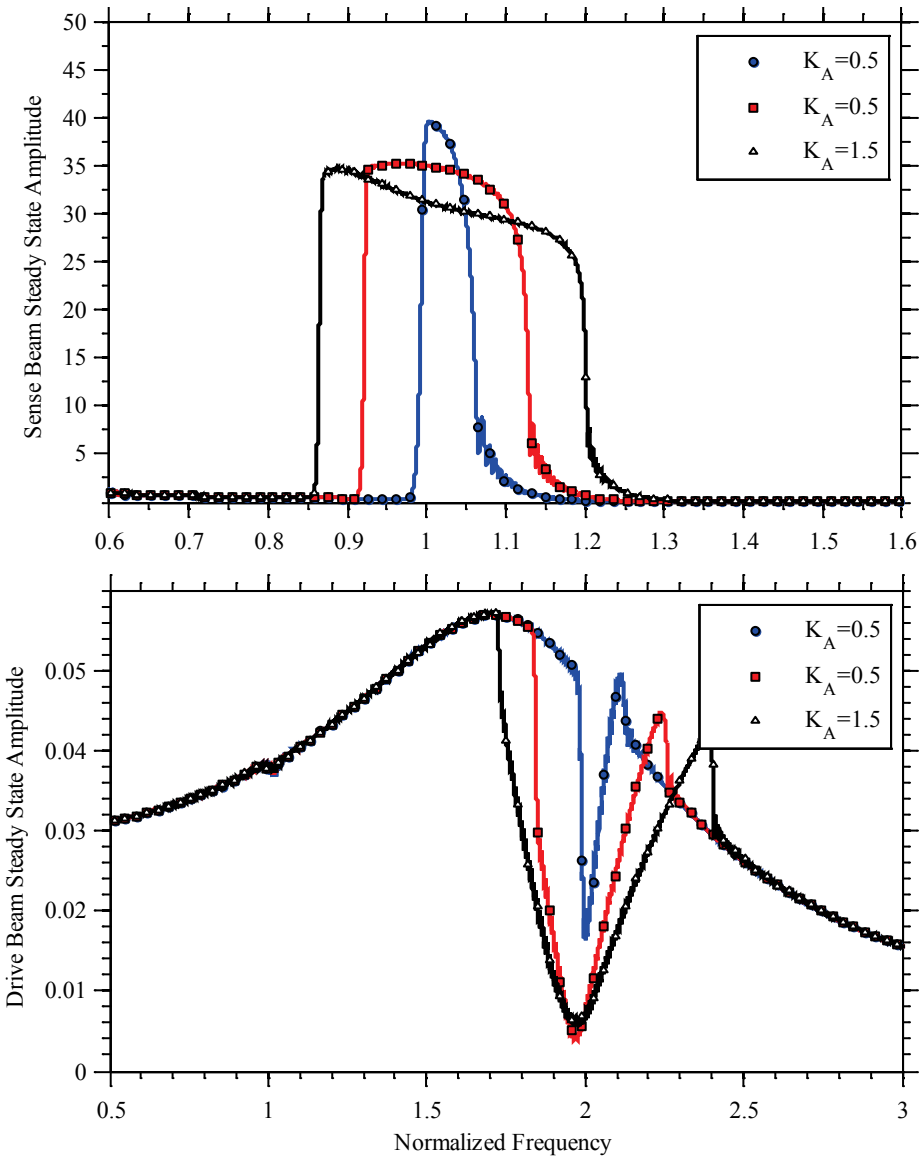

Figure 3-13: The effect of feedback of the coupling term $K_A m_2 r_2 \ddot{\theta}_2 \sin(\theta_2)$ with different proportional gains KA on the sense (top) and drive (bottom) beams' frequency responses

Additionally, the sense mode gain can be further increased by feeding back the nonlinear term $K_C\, m_2 r_2 \cos(\theta_2)\dot{\theta}_2^2$ from the excitation signal driving the system as shown in Figure 3-14.

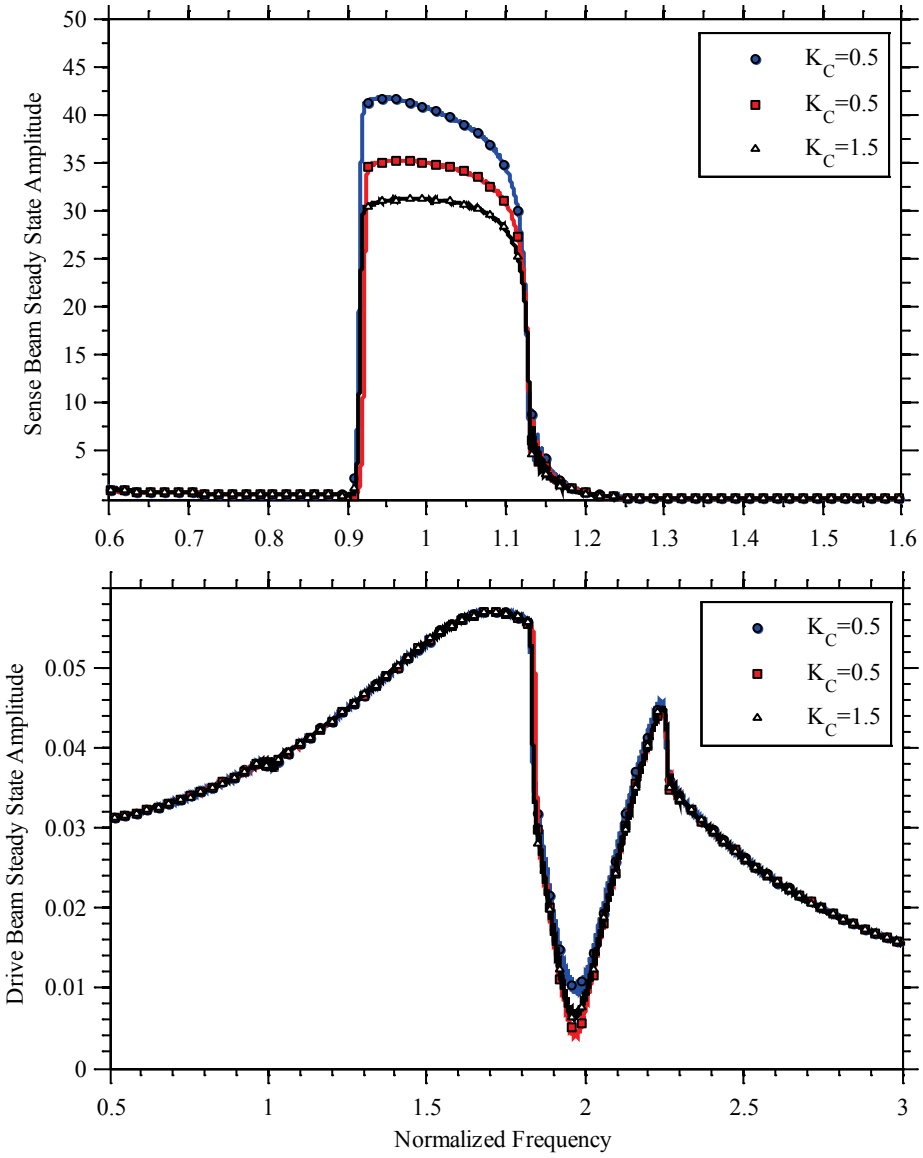

Figure 3-14: The effect of feedback of the coupling term $K_C\, m_2 r_2 \cos(\theta_2)\dot{\theta}_2^2$ with different proportional gains K_A on the sense beam (top) and drive beam (bottom) frequency responses

3.4. Conclusions

In this chapter we presented a simplified mathematical model for a T-beam gyroscope and its simplification as a resonator. The analytical derivations and numerical simulation results proved similar to other two degree of freedom systems with quadratic nonlinearities discussed in Chapter 2 and the results will be validated experimentally in Chapter 4. This concludes the validity of the mathematical model in spite of its simplicity.

Furthermore, the possibility of enhancing the frequency response and sensitivity of the gyroscope model through feedback of coupling terms is shown through numerical simulation. These outcomes establish the foundation for gyroscope designs with enhanced performance and robust stability.

Chapter 4.

Experimental Testing and Results

4.1. Introduction

In this chapter, the proof of concept using experimental macro-models is illustrated. Several prototypes were developed but only the valid test-beds are mentioned. At first, common experimental designs and procedures are stated. After that, major sources of errors are reviewed. The experimental tests follows the theoretical sections of this thesis focusing on the T-beam structure first as a resonator (i.e. no input angular velocity) then as a gyroscope. For each shown experiment, time, frequency response and saturation testing results are compared between the linear and nonlinear cases. The main forcing function variables are excitation amplitude, frequency and input angular velocity in the gyroscope case.

4.2. Experimental procedures

4.2.1. Natural Frequency Tuning

Impulse Response Test Procedure

The purpose of this test was to excite the device under test (DUT) with an impact hammer in order to excite the device's natural frequencies as shown in Figure 4-1. This test procedure was heavily used in the structural tuning process. However, great care had to be considered not to exert excessive impact force that might have detuned the natural frequencies specifically in the drive beam. This was because of the imperfection in the clamped-clamped implementation and non-ideal boundary conditions. The structure was designed so that the torsional out-of-plane mode point {3} is shifted away by at least 20% from the first two in-plane ones (points {1} and {2}) to minimize its effect. The drive beam thickness was set to approximately twice the sense beam thickness.

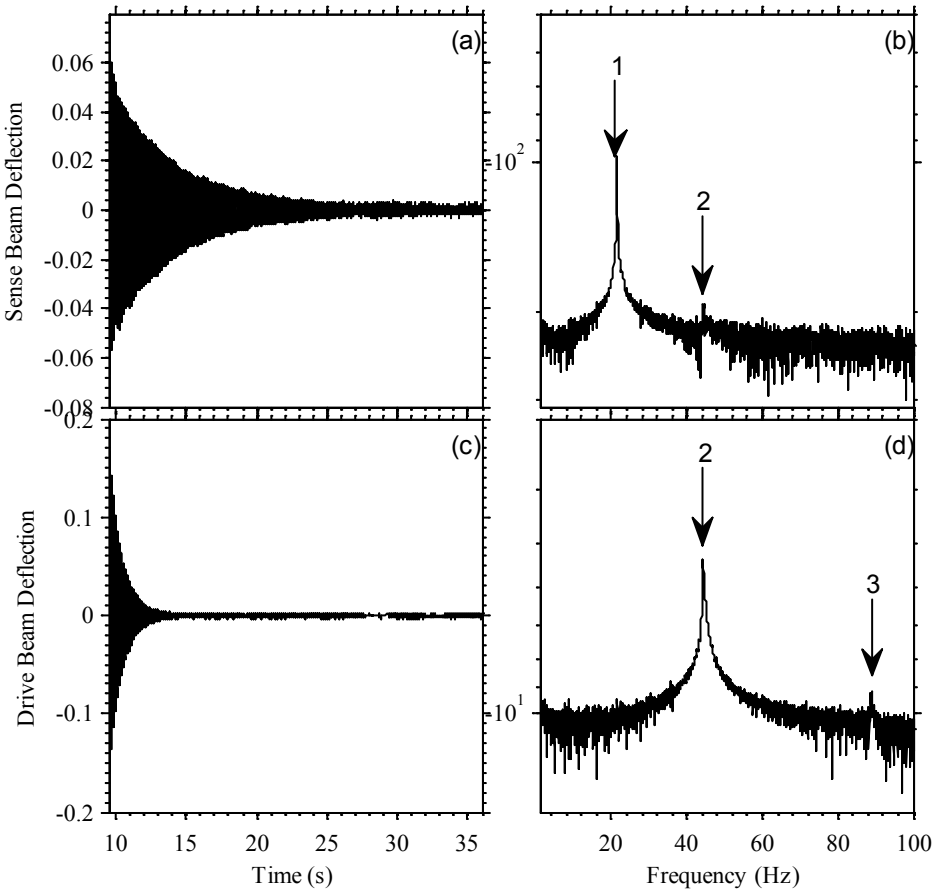

Figure 4-1: Impulse response sample results showing the sense beam frequency response (a, b) and the drive beam frequency response (c, d)

Each DUT was first built based on estimates from both the analytical and FEA models. The physical design was developed to have natural frequencies close to the mathematical model. Nevertheless, the physical model was fine-tuned to meet the design constraints (e.g. 2:1 frequency ratio). The two most common techniques used for tuning were to either add a tuning mass as implemented by Haddow [44] or by changing beam lengths. In either cases, the linear frequency response using the Fast Fourier Transform (FFT) of the impulse time response was obtained as a tuning verification tool. In all the mentioned experiments an impulse test was implemented before and after each test.

After an impulse was applied to the system, acceleration, displacement and in some cases strain gauge signals were logged in real-time at a sampling rate of 1K Sample/s. This

choice of sampling frequency was based on the preliminary FEA analysis of each structure such that the first three natural frequencies were designed to be less than 100 Hz. Furthermore, all logged time-domain data were passed through a linear phase band pass filter as will be shown in a later section. The filtered response was then converted to the frequency domain using the Fast Fourier Transform method (FFT).

Initial Condition Test Procedure

In this procedure the T-beam was given an initial deflection (i.e. initial condition) at its sense beam's tip. After that the structure was released into free vibration. In most cases this initial displacement was large enough to excite the main resonance-frequencies of interest: the fundamental and second in-plane harmonic of the sense beam and the first of the drive mode labeled points {1}, {2} and {3} respectively in Figure 4-2(d). In this example test, the detuning frequency was determined between points {2} and {3}, which was used to study its effect on performance. Compared to the impulse response test, this procedure was found to be more efficient to be used in tuning as the risk of detuning the system via excessive impact was minimized.

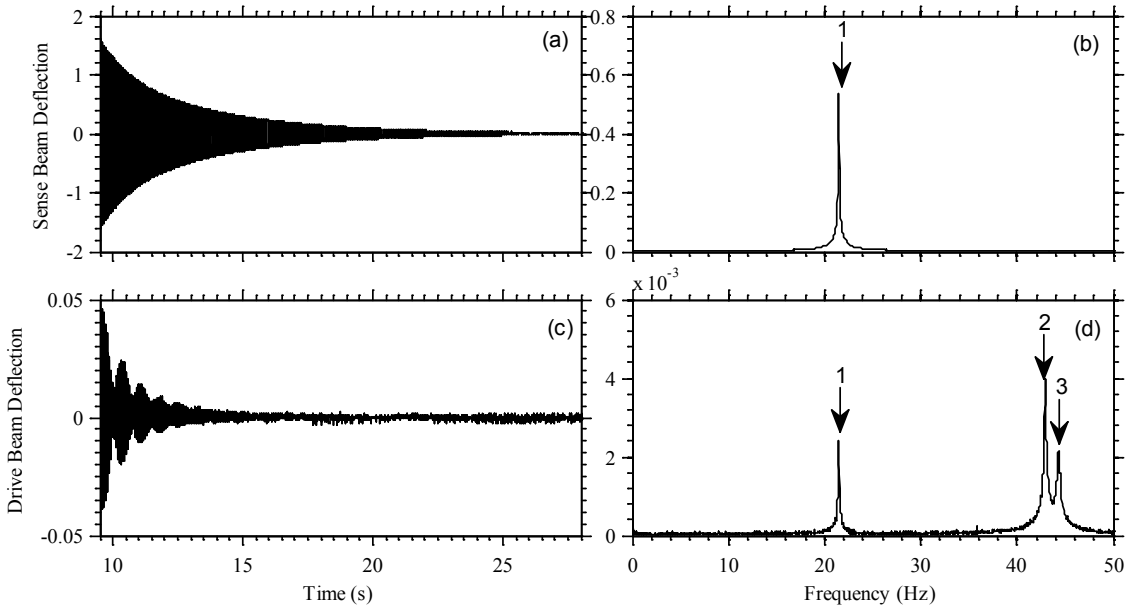

Figure 4-2: Initial deflection sample results showing the sense beam frequency response (a, b) and the drive beam frequency response (c, d)

Experimental Verification of Mode Shapes

The next step after the determining the natural frequencies of the structure was to verify mode shapes. In case of structures with relatively large modal amplitudes and frequencies less than 5 Hz, visual verification of mode shapes was sufficient. In the case of higher frequencies, a high-speed camera was used to verify the in-plane mode-shapes as shown in Figure 4-3. On the other hand if the displacement couldn't be verified visually or using the high-speed camera, non-contact LASER displacement sensors were pointed at various locations of the structure to verify mode shapes.

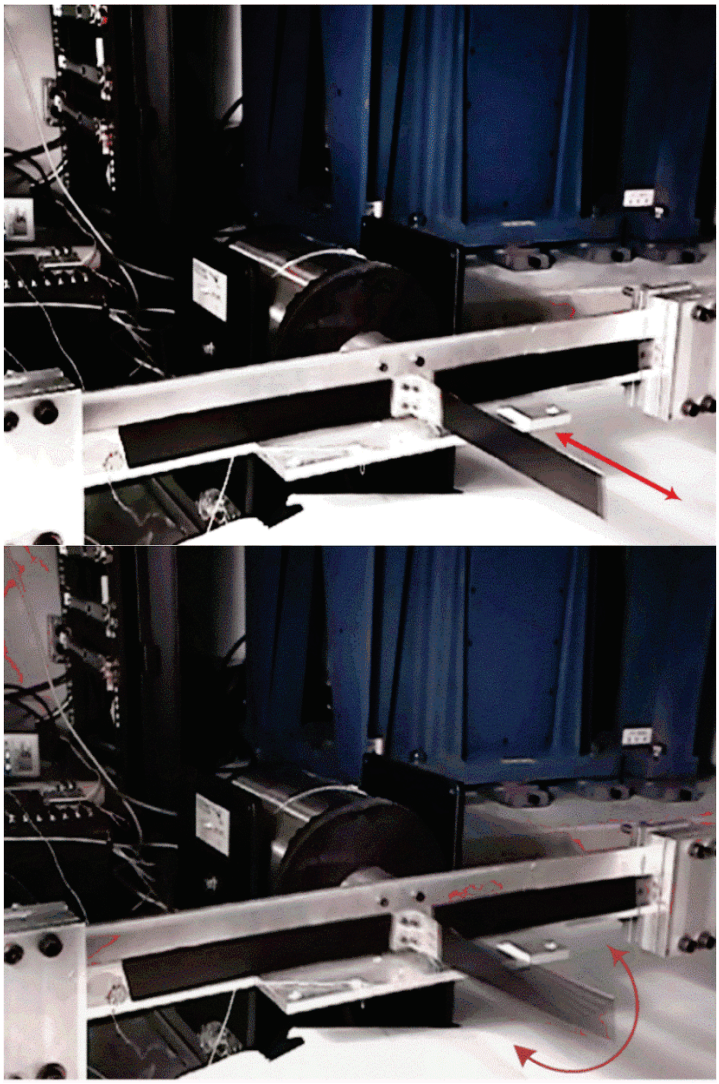

Figure 4-3: Mode shape verification using a high-speed camera for the first T-beam resonator macro-model prototype showing the drive mode (top) and the sense mode (bottom)

4.2.2. Steady State Amplitude Response Test Procedure

Since taking the time response for an impulse and transforming it into the frequency domain via FFT only yielded the linear frequency response function, a few other methods were devised to study the nonlinear counterpart. In this section, the two common methods used for this research are briefly explained.

Steady state amplitude response

The first method was based on the application of a harmonic excitation signal to the structure at a frequency relatively lower than frequency band under study. After that, the structure was monitored online in the time domain until the vibration amplitudes reached steady state. One drawback of this method was that the elapsed time for the system to reach steady state widely varied depending on the nearness of the excitation frequency to the natural frequency and damping. Once the system reached steady state, the amplitude was averaged over a proper interval of time with a sufficient number of oscillations (e.g. order of hundreds of cycles) or an envelope detector was used. However, depending on the frequency separation between the excitation frequency and the natural frequency, the response amplitude of the sense beam could suddenly drop after a change in the excitation frequency as shown in Figure 4-5 between t=620 and t=640 seconds**.**

As a solution, a simple approach to overcome the aforementioned problem was devised. The excitation frequency was applied as a staircase signal. The goal was to maintain the same excitation frequency for a sufficient amount of time for the system to reach steady state. After that, the excitation frequency was increased or decreased depending on the nature of the test such as an upward frequency sweep or a downward one.

In order to avoid transients, only the last few number of cycles were captured from sensors before a new excitation frequency transition takes place. The transition of the excitation frequency was located using the first derivative of the stair case pattern resulting in a delta function representing every change (i.e. delta train). Then the steady state values were determined on the time axis 3 seconds before each delta function. A summary of the algorithm to determine the nonlinear steady state response is depicted in Figure 4-4.

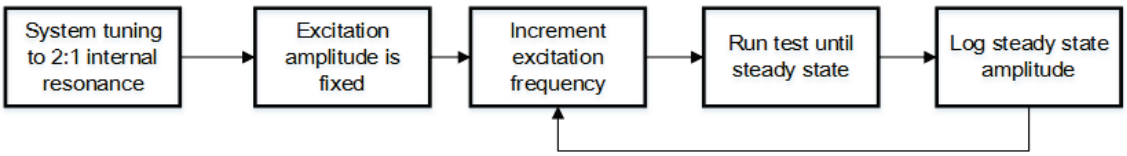

Figure 4-4: Flowchart of the procedure to obtain the nonlinear frequency response using steady state amplitude

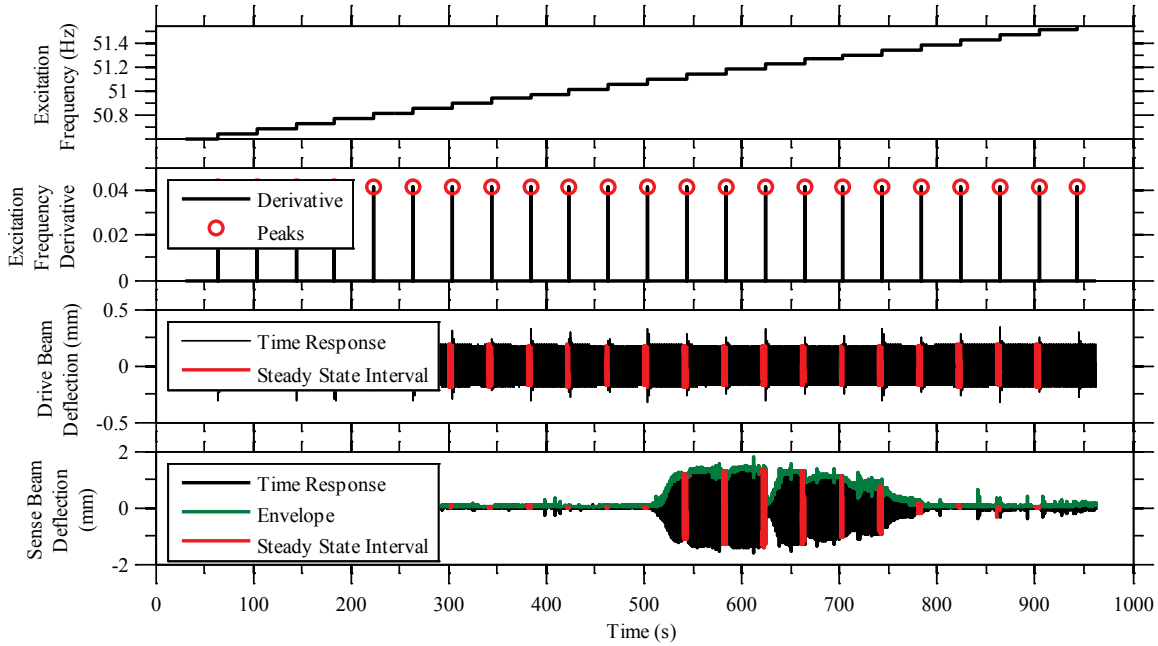

Figure 4-5: Time history showing the difference between obtaining the frequency response to an input staircase excitation frequency sweep (a), using an envelope detector versus calculating the steady state amplitude at discrete time intervals (c, d) using the excitation frequency time-derivative (b)

Once a sufficient number of points was acquired, the steady state amplitude response function could be determined as shown in Figure 4-6**.** The advantage of using the derivative of the stair-case signal to locate the exact time of transition for steady state amplitude calculation proved helpful in avoiding transient responses. The contrast between the two methods can be shown by comparing the result of an envelope detector on one of the drive beams by calculating the steady state amplitude right before the transition in frequency occurs in Figure 4-6. This is due to the fact that the envelope detector will not differentiate between the time transients occurring after each change of excitation frequency giving a false result for the steady state amplitude.

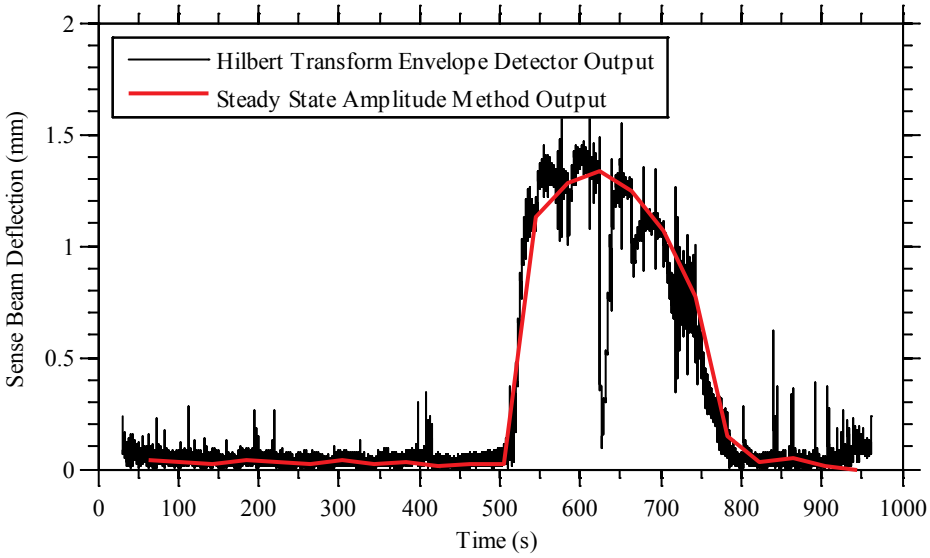

Figure 4-6: Performance comparison in calculating the frequency response using a Hilbert transform envelope detector versus using the steady state amplitude for a staircase frequency sweep

Slowly varying frequency sweep

As seen in the last section, the steady state amplitude response can be time and computer-memory consuming. As a more convenient alternative, a slowly varying frequency sweep was found to achieve acceptable results in less time. However, in this case, great care had to be considered when setting the rate of the frequency sweep. It had to be small enough to allow the system to reach steady state. After that the envelope of the response's amplitude can be determined. An advantage of this method over the previous one was that it didn't induce large transient responses as the frequency is varied as a ramp function not as a staircase. Another two major contributors to the frequency response were internal detuning and damping (i.e. quality factor) of the structure under testing.

4.2.3. Saturation Test Procedure

In this experiment, the excitation frequency was held constant at the drive beam's first natural frequency (i.e. twice the sense beam's) and the excitation amplitude was incremented. Increasing in excitation amplitude could have been done either manually, or automatically using a staircase or ramp signal with small slope. The experimental

procedure is shown in Figure 4-7. The procedure to determine the steady state amplitude is the same as discussed earlier in this chapter.

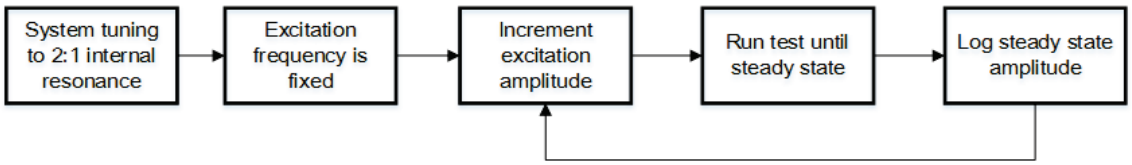

Figure 4-7: Flowchart of the procedure to show the nonlinear saturation phenomenon using an excitation amplitude sweep

Boundary conditions, clamping and vise parallelism

Boundary conditions play an important role in the analytical as well as the experimental system behavior. It was found that the clamping forcing greatly affected the natural frequencies specifically for the drive (clamped-clamped) beam.

Aluminum clamps were originally chosen for their light weight and ease of machining in the first prototype. The reasoning behind that was great attention had to be given not to exert unnecessary forces perpendicular to the shaker's direction of motion. For the same reason, a linear bearing guide was adopted in the design**.** As a result, the choice of using aluminum clamps proved problematic due to its material properties such as stiffness. Experimental results showed that the force exerted by each of the clamp screws had significant effects on the drive beam's natural frequency. As a solution to this issue, a torque wrench was used to assure the uniform force distribution exerted by the clamp screws on the beam.

Warmup Effect on zero-input bias drift

Equipment warm-up time was observed to affect the zero-input bias of the sensors. Electronic equipment used in this test included data acquisition cards, piezoelectric and strain-gauge amplifiers and two LASER displacement sensors. The LASER displacement sensors' signals showed a drift and DC bias in the case of no system excitation as can be seen in Figure 4-8. The difference in bias at t=0 is due to human error while placing the sensors in proximity of the sense and drive beams respectively. The signal drifts is in the

order of hundreds of micrometers over a 4.5 hours' time span. This zero-input bias drift was filtered using the bandpass filter mentioned later in this chapter.

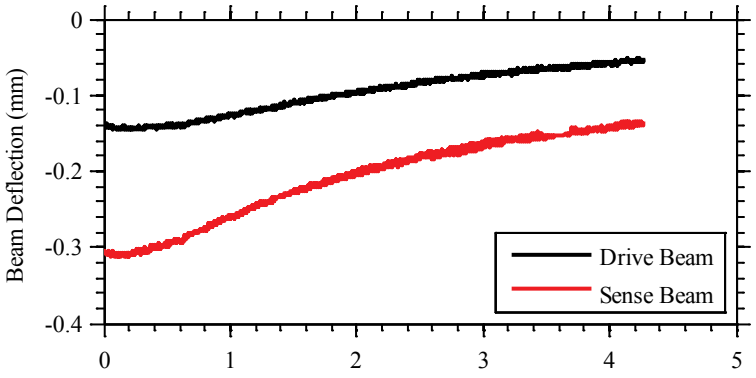

Figure 4-8: Effect of 4.5 hours warmup time on zero-input DC-drift

A frequency and amplitude time-response shifts were also observed while testing T-beam structures actuated with misaligned PZT actuator patches as shown in Figure 4-9. Based on literature [50], these effects are due to imperfect boundary conditions and pre-stresses acting on the DUT. This explanation agrees with the clamping challenges discussed in the previous section. As a solution, the vise clamps had to be aligned using a micrometer and machined guides to ensure symmetry and minimum pre-stress effects.

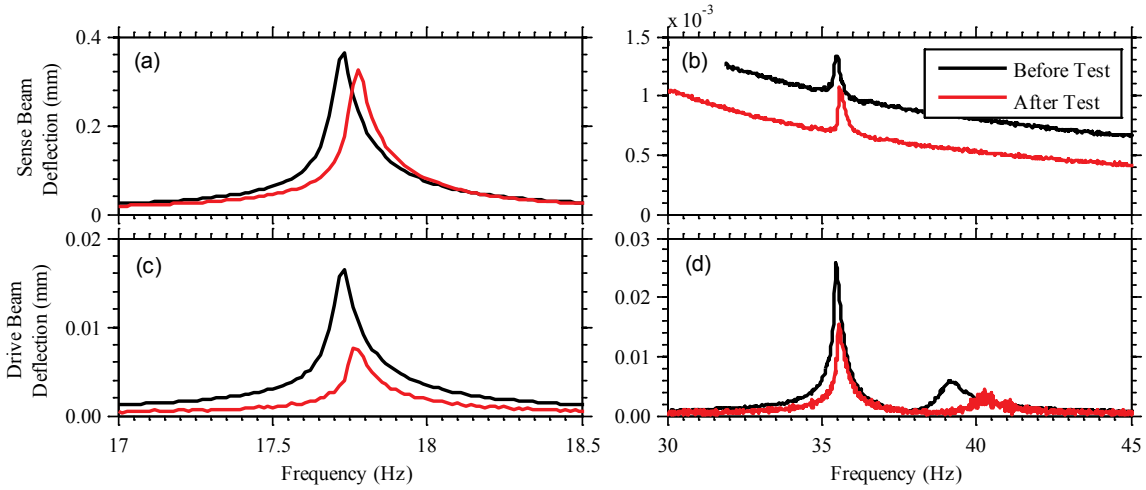

Figure 4-9: The effect of 4.5 hours warmup time on the frequency response of the sense beam (a, b) and the drive beam (c, d)

Angular Velocity effects on the T-Beam Structure

The centrifugal force acting on the system was found to affect the natural frequency of the drive beam in particular as shown in Figure 4-10. In the case of a linear system with low damping this would result in a significant gain drop. However, given a flattop frequency response as will be shown, the system maintains consistent performance over a wider bandwidth. In the second prototype, at higher angular velocities this centrifugal force overcame the excitation force applied on the drive beam limiting the measurement range.

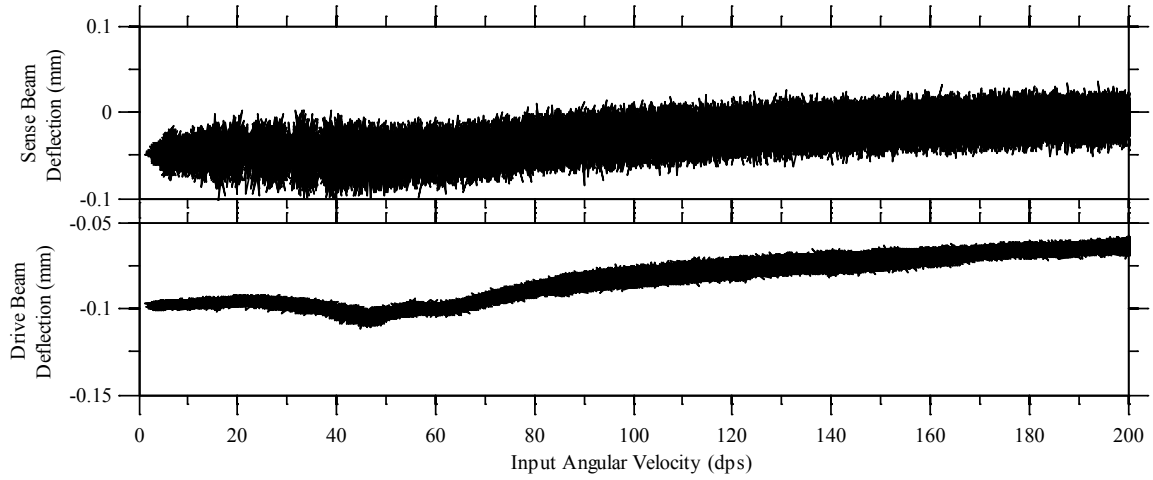

Figure 4-10: Angular velocity effect on an unexcited T-beam structure, at higher angular velocity the centrifugal force shifted the joint mass pre-stressing the drive beam

Filtering Electrical noise

Given that sampling frequency was fixed through all experiments at 1000 Sample/s, all acquired signals were passed through a software band pass filter (BPF). This linear phase FIR filter was designed to block the DC bias and drift as well as high frequency noise as shown in Figure 4-10. The –3 dB cutoff frequencies was set to 5 and 60 Hz respectively. This ensured that the first three natural frequencies of interest passed. Figure 4-11 shows the filter's magnitude and phase responses.

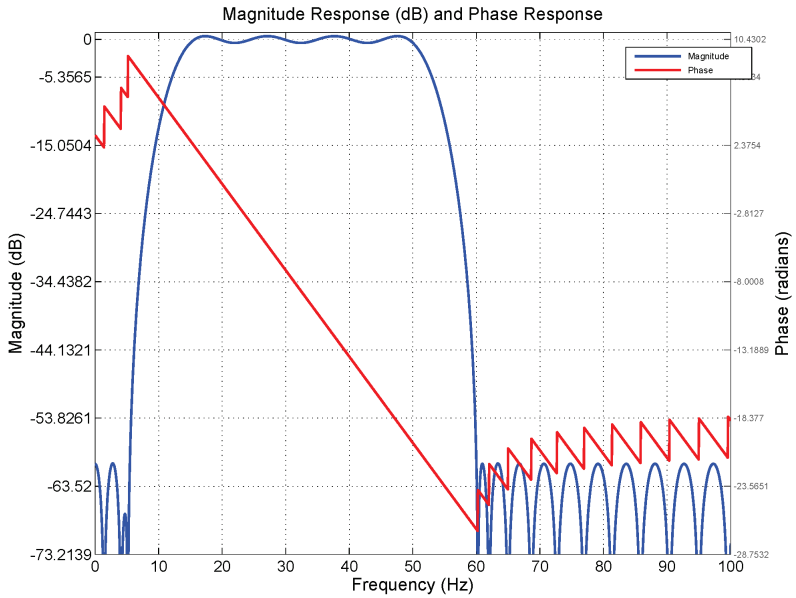

Figure 4-11: Band pass filter magntiude and phase frequency response used to filter DC bias, slow drift and high frequency noise affecting the LASER displacement sensor signals

4.3. Experimental Prototypes

4.3.1. First Experimental Prototype

Macro T-Beam Resonator Prototype

Several T-structure macro-scale prototypes were built in order to precisely tune the system to have the correct frequency ratio of 2:1 between its two lateral vibration modes. The system was also designed such that the torsional mode was located away from the in-plane modes. The first full functional prototype was designed and built using off-the-shelf stainless steel sheet metal beams with dimensions as shown in the next table.

Table 4-1: First Experimental Prototype Dimensions

Part	Parameter	Value
Drive Beam	Length	650 mm (25.6 in)
	Width	1.519 mm (Gauge 16 / 0.0598 in)
	Thickness	35 mm (1.38 in)
Sense Beam	Length	240 mm (9.45 in)
	Width	35 mm (1.38 in)
	Thickness	0.607 mm (Gauge 24 / 0.0239 in)

Furthermore, a vibration shaker controlled by a Brüel & Kjær vibration control system (LDS COMET USB) was used to drive the resonator for the experiments. A vibration shaker was specifically chosen to study the effect of increasing drive/excitation signal amplitude on the system's time and frequency responses as well the nonlinear phenomena under investigation. As shown in Figure 4-12, a linear guide was adapted to support the structure's longitudinal motion along the shaker's axis and minimize the vertical load and avoid instabilities in the shaker's drive controller. Nevertheless, tuning the linear guide to be perfectly parallel to the shaker's motion axis proved challenging. A misaligned guide caused the shaker to excite the support structure which added measurement noise.

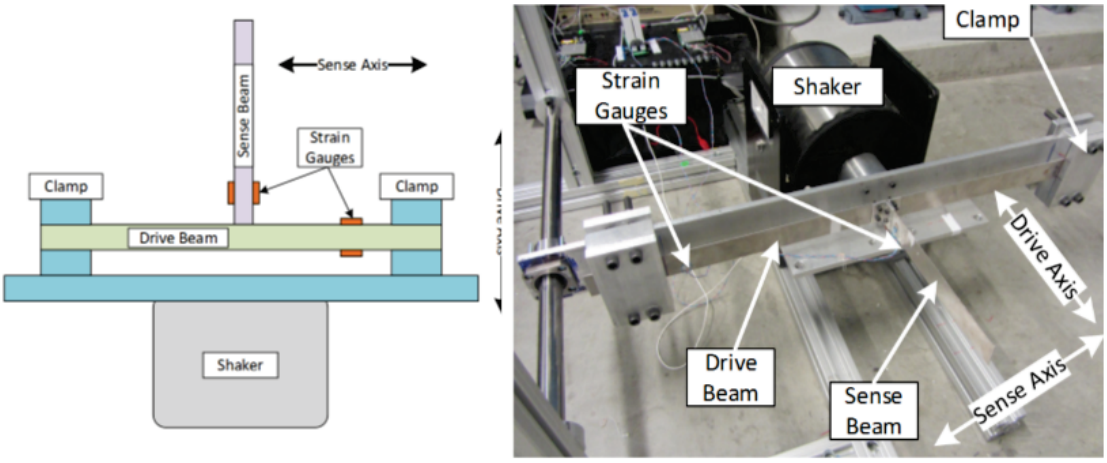

Figure 4-12: First T-Beam macro-scale experimental prototype used as a resonator excited by an electromagnetic shaker

Strain gauges mounted on the drive and sense beams were utilized to measure deflection. T-shape strain gauges were connected in a full Wheatstone bridge configuration for high sensitivity. In addition, this T-rosette type strain gauge configuration was adopted for its temperature compensation and axial strain rejection. Two EA-13-125TQ-350 strain gauge sets from Vishay industries were used as shown in Figure 4-13. Also a full layer of Cyanoacrylate strain gauge adhesive was applied to mount the strain gauges from HBM part number Z70 and left for 24 hours to fully cure.

Once the strain gauges were bonded successfully to the substrate, wiring the electrical connections was the next step. Since this prototype was on a relatively large scale,

wire mass and stiffness played a negligible role in affecting the system's dynamics. However, this was not the case with the second smaller prototype as will be discussed in later sections. In this design, wire wrap was soldered to connect the strain gauges on the stainless steel substrate. Hot glue was then used as a strain relief as the strain gauge pads could easily be damaged if the wire was pulled rendering them dysfunctional. After that the strain gauge wires were connected to a standard 350 Ω strain gauge amplifier and then sampled in real-time via the DSPACE data acquisition card.

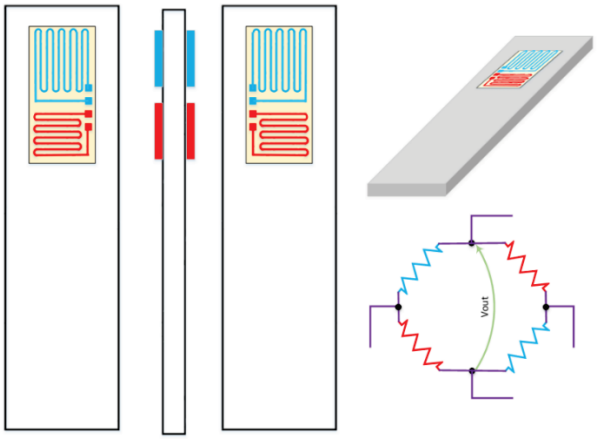

Figure 4-13: Strain gauge configuration to measure beam bending with temperature compensation and axial-strain rejection

The use of an electromagnetic shaker for base excitation helped characterize the forces needed to choose the proper piezoelectric actuators in the experimental prototypes. As mentioned in the experimental procedures at the beginning of this chapter, the structure had to be first tuned to 2:1 ratio using an impulse response. The tuning process in this case was completely performed by changing the drive beam length through relocating the clamps maintaining symmetry about the shaker's longitudinal axis. An example impulse response of the quasi-tuned structure is shown in Figure 4-14. The first frequency peak at approximately 7.7 Hz is the first natural frequency (i.e. sense mode), the second and third frequency peaks represent the second harmonic of the sense mode and the first drive mode respectively. The frequency difference between peaks {2} and {3} is approximately 1 Hz, with ratios between them and the sense mode (peak {1}) equal 1.98 and 2.12 respectively, the system was said to be tuned. Moreover the natural frequency at {4} depicts the torsional

mode showing a shift away from the second mode by approximately 75%. This insured the minimum effect of the torsional mode on the system dynamics within the frequency band of interest.

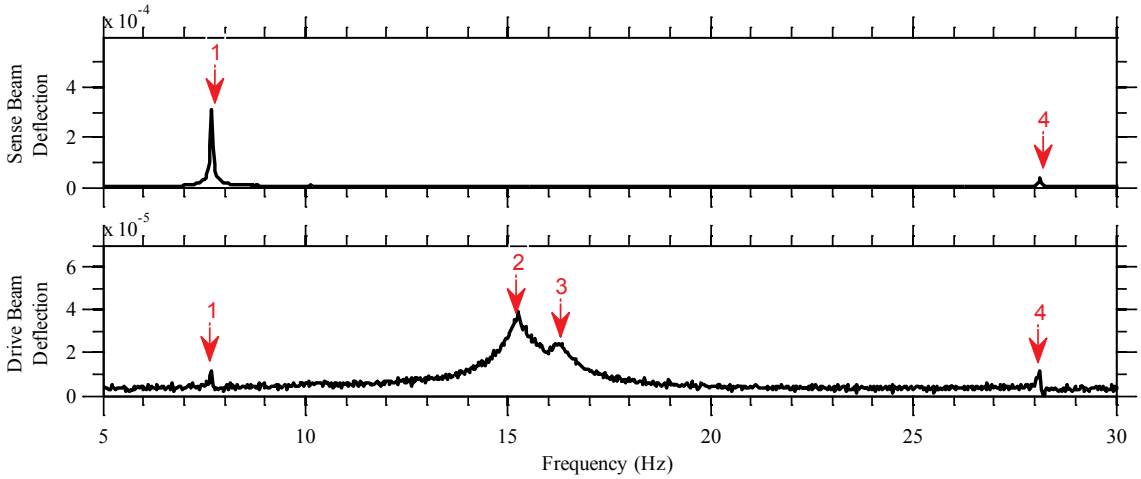

Figure 4-14: First T-beam resonator impulse response in the frequency domain showing the frequency response of the drive beam (top) and the sense beam (bottom)

Time Response

Once the system was tuned, a quick verification test to show the effect of the 2:1 internal resonance was performed. The shaker's excitation frequency as set to twice the first mode natural frequency (e.g. 15.4 Hz) and a reasonable excitation amplitude (0.254 mm for this test). As illustrated in Figure 4-15, the bottom plot shows the measured strain gauge voltage located on the drive beam reaching steady state in about t=10 seconds. On the other hand, the sense beam remains unexcited until the drive beam reached steady state when a virtual energy gate can be thought to open between the two modes. After that, the deflection of the sense beam started to grow with relative decrease in the drive beam deflection. The sense beam deflection reaches steady state at approximately t=23 seconds with a frequency half that of excitation.

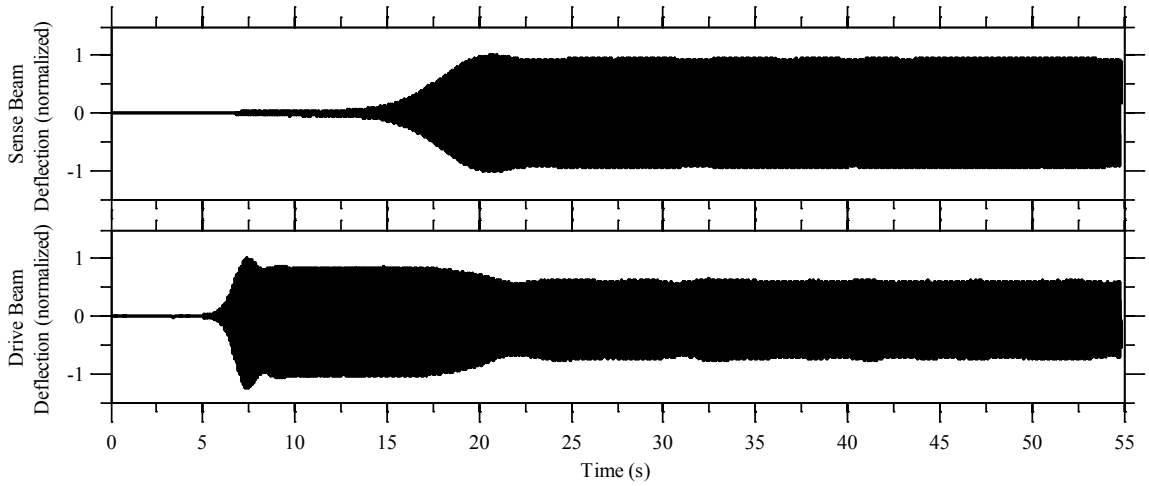

Figure 4-15: T-shaped resonator time history showing the transfer of energy from the drive beam (bottom) to the sense beam (top)

Steady State Amplitude Frequency Response

One relatively challenging aspect of using the shaker was that its controller did not accept external input signals. This rendered the idea of automating a stair-case frequency sweep impossible. Nevertheless, the test was completed manually by setting the shaker's drive signal parameters using the controller's provided software. The steady state amplitude response was logged given different excitation frequencies (around twice the sense mode natural frequency). After that the test was repeated using a higher excitation amplitude. As can be seen in Figure 4-16, the sense mode frequency response has a flat-top (similar to that of a band-pass filter) with a stable frequency region of symmetry about the sense beam's natural frequency. These results match the predictions obtained from analytical model shown in Figure 3-10 and Figure 3-11.

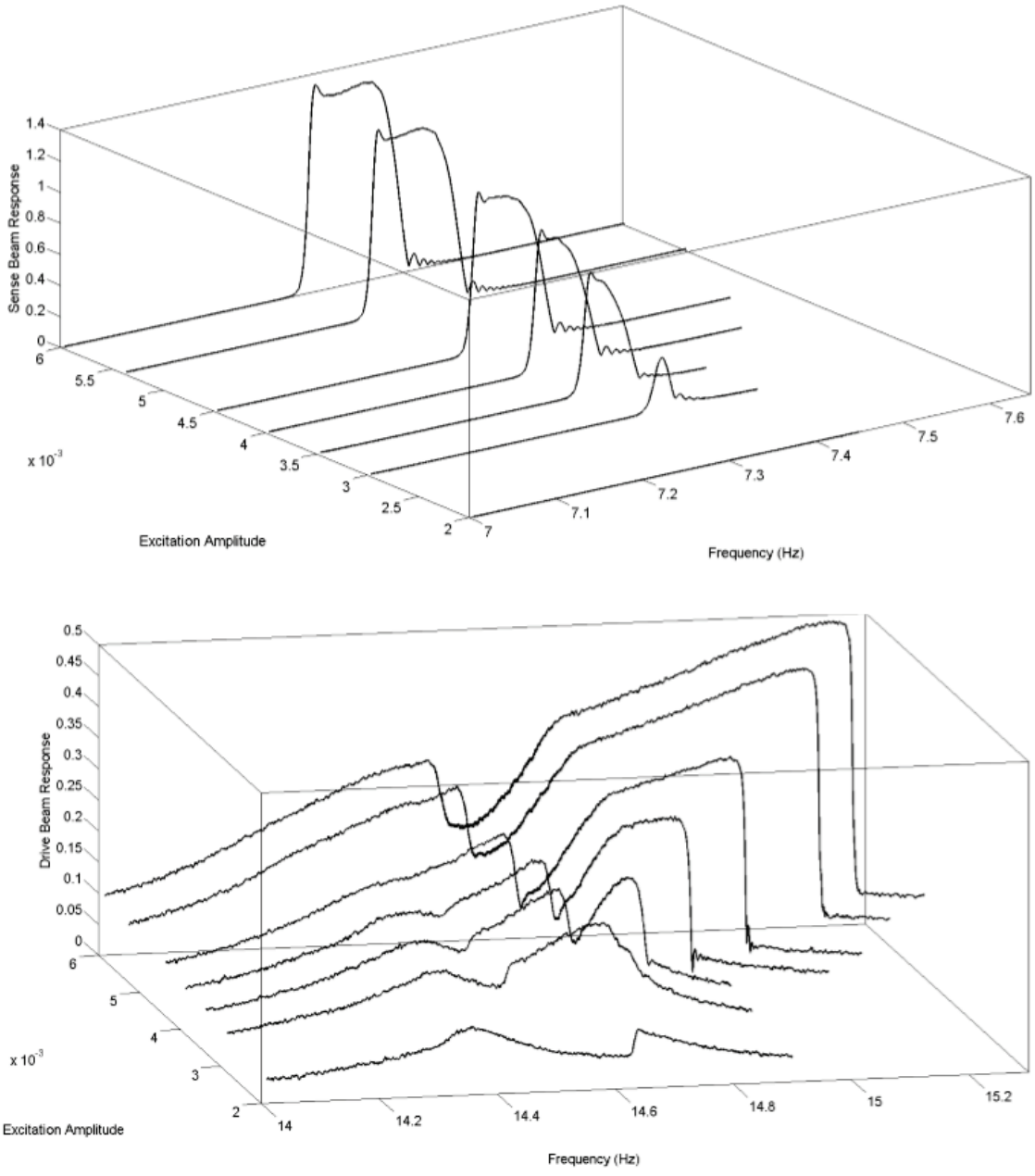

Figure 4-16: First resonator prototype frequency responses for various excitation amplitudes; sense beam (top) and drive beam (bottom)

Saturation

Given that the system was tuned to 2:1 ratio and excited at its second mode, the saturation phenomenon occurred after increasing the excitation amplitude beyond a certain threshold. Before that threshold was exceeded, only the drive beam was excited and the system behaved linearly. However, after this excitation threshold was exceeded, the energy was channeled to the sense mode and was excited at its own natural frequency (i.e. half the drive mode frequency) as shown in Figure 4-17.

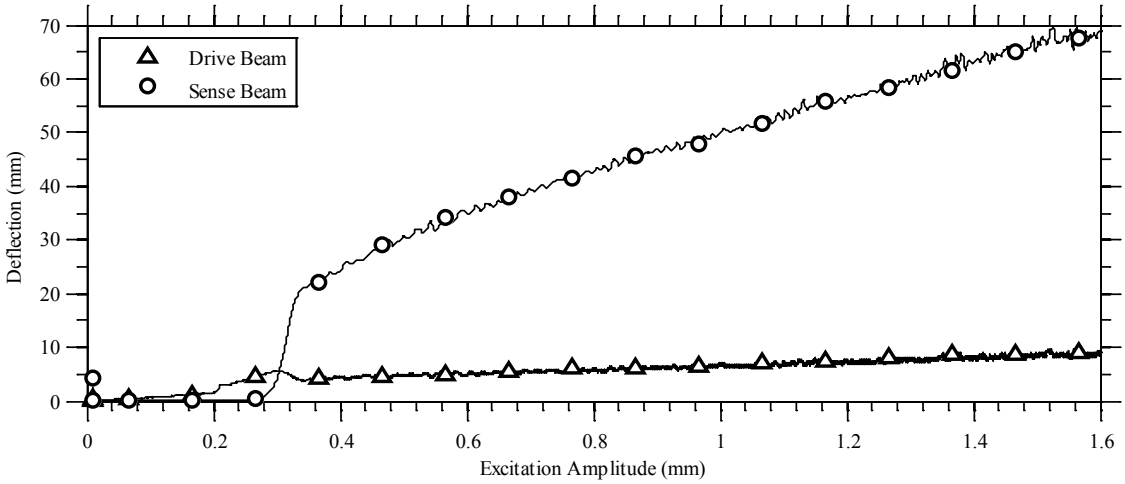

Figure 4-17: First Macro T-beam prototype saturation experimental results showing the transfer of energy from the drive beam to the sense beam

Gyroscope Experiment

Next was to study the effects of angular velocity on the T-beam structure. The first design constraint was the driving actuator. In the previous resonator experiments, an electromechanical shaker was used. However, since a rotating platform was required for this experiment, an actuator with significantly lighter weight was needed. A flexible piezoelectric actuator (Physik Instrumente™ P876.15) was chosen as the driving actuator. It offered sufficient blocking force (775 N) to drive the system into the nonlinear region of operation and lower power consumption.

Moreover a custom-made rate table test bed was designed and built to rotate the test bed as shown in Figure 4-18. The rate table design contained a slip-ring to connect the rotating sensors and actuators to their respective amplifiers and data acquisition cards without

entanglement. It also used an industrial grade servo motor and a quadrature shaft encoder to monitor angular displacement for feedback control purposes. The gyroscope calibration test was then performed by linearly increasing angular velocity of the rate table and then maintaining a steady state angular velocity. The sense beam strain was then monitored using strain gauges showing promising results as can be seen in Figure 4-19.

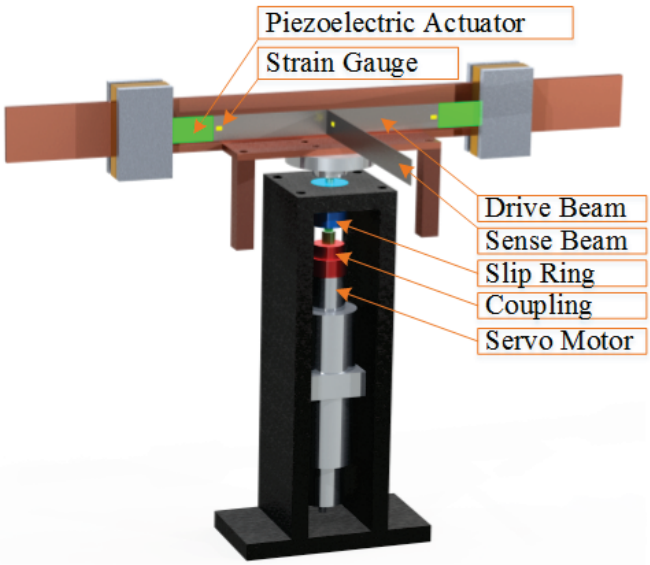

Figure 4-18: First T-beam gyroscope experimental prototype mounted on a custom-made rate table using piezoelectric actuators for excitation and strain gauges for deflection measurements

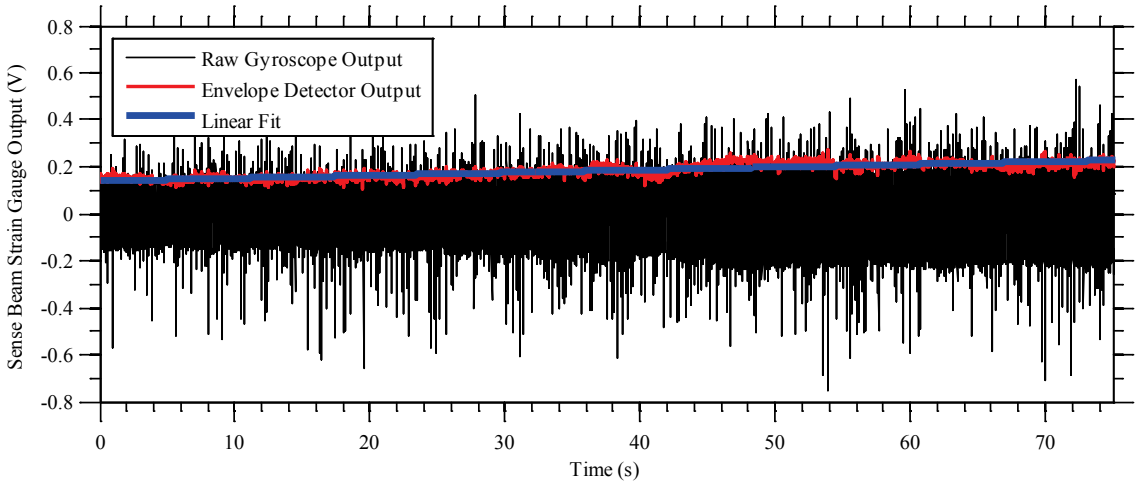

Figure 4-19: Time history for a ramp angular velocity input of the first T-beam gyroscope prototype showing a linear correlation to the sense beam deflection

4.3.2. Second Experimental Prototype

A second resonator prototype, shown in Figure 4-20, with different design specifications was built for several reasons. Firstly to validate the results of the earlier prototype. Secondly was to mitigate the observed design shortcomings, and thirdly to be later used on a state-of-the-art rate table for validating experimental results in response to rotary motion.

The physical prototype was implemented using off-the-shelve available materials (i.e. standard stainless steel sheet metal thicknesses) shown in Figure 4-20. The drive beam thickness was chosen to be thicker than the sense beam's in order to shift the torsional mode as far as possible but not overly thick to be easily actuated using piezoelectric actuators. A mass was attached at the joint to reduce the drive mode natural frequency to be closer to twice the sense mode's natural frequency.

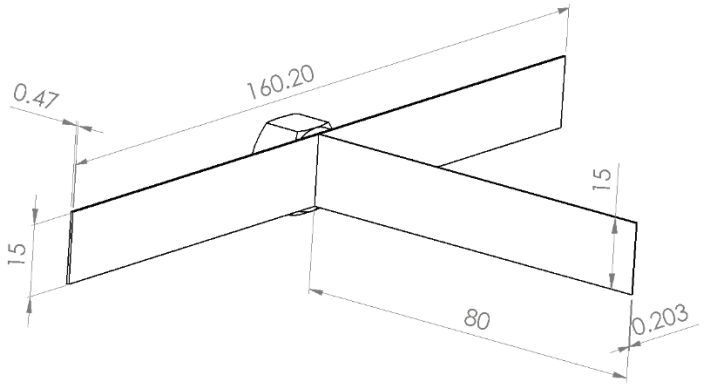

Figure 4-20: Preliminary T-beam resonator physical design dimensions (in mm) used in simulation

Mode shapes of the structure were verified using FEA analysis (ANSYS^{TM}) to ensure the proper order of mode shapes and natural frequencies. The first three mode shapes are shown in Figure 4-21. This step proved important in the implementation stage of the physical model as the displacements were smaller than to be visually observed without specialized equipment.

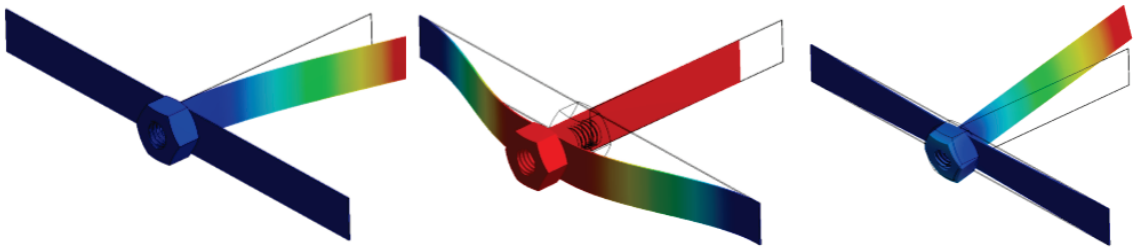

Figure 4-21: FEA simulation using ANSYS™ showing the first three mode shapes of the T-beam resonator (left) sense mode (middle) drive mode (right) torsional mode

The earlier design utilized strain gauges to measure deflection. Since this system is on a relatively small scale, strain gauge wires significantly altered the system dynamics. As a solution, two noncontact LASER displacement sensors (LTS 15/03 and 15/12) were used to measure deflection of both the drive and the sense beams respectively as shown in Figure 4-22.

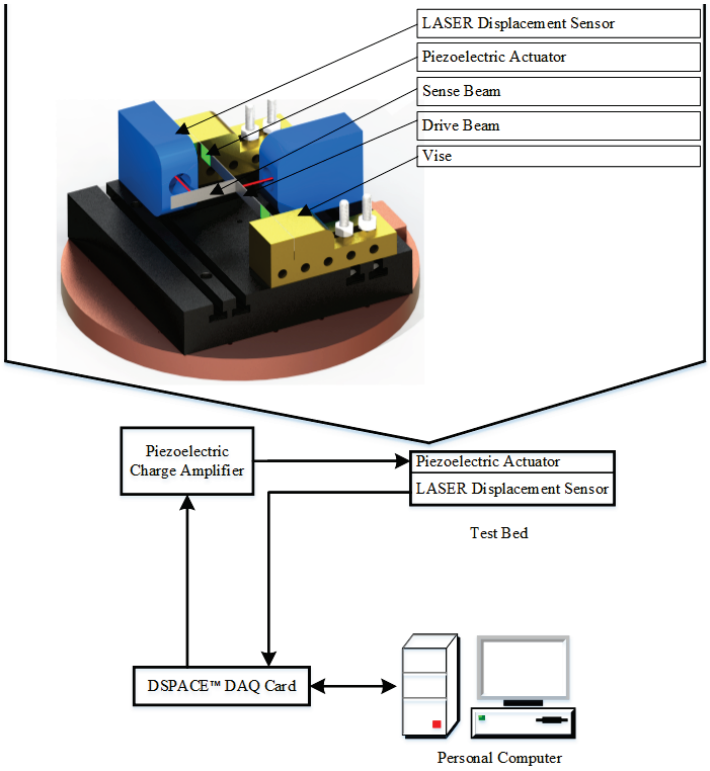

Figure 4-22: Second T-beam gyroscope macro-scale experimental prototype composed of a two degrees of freedom resonator, piezoelectric actuators and LASER displacement sensors for deflection measurements

Also better drive beam clamps were designed to overcome the challenges experienced in the first prototype. The earlier clamp design proved very challenging with respect to tuning as it used a four screw configuration as shown on the left in Figure 4-23, the same setback was reported in [51]. As a solution to this problem a pair of precision grinding vises were used as shown in Figure 4-23. Two KBC™ P/N 1-814-015 grinding vises that utilize one machine cap screw to hold the work piece were adopted. This eliminated the challenge of tuning the torque on each of the four screws to maintain uniform distribution of the clamping force on the beam. Nevertheless, both vises holding the drive beam had to be perfectly aligned using specialized equipment for near-ideal boundary conditions.

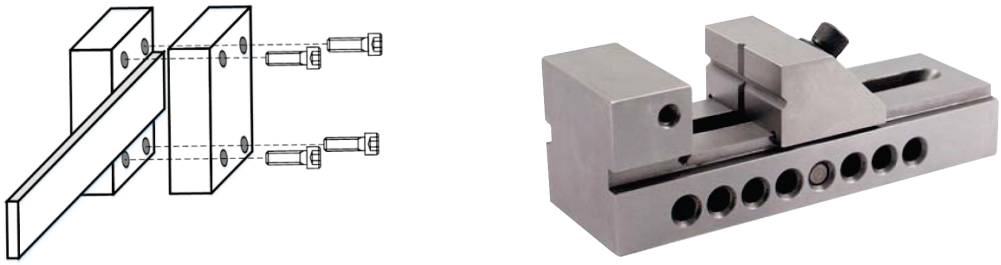

Figure 4-23: Early prototype clamp design (left) vs precision grinding vise (right)

The second modification updated in this design was the use of piezoelectric actuators instead of the vibration shaker so it can be later used on a rate table. The design constraint in this case was not only the unavailability of an accurate vibration shaker suitable for this task, but also the slip ring wire current rating were significantly lower than needed.

An updated T-shaped structure was designed in CAD software (Solidworks™), mode shapes analyzed in ANSYS™ then physically built. Since this experiment acts primarily as a proof of concept for a gyroscope, the platform needed to be rotated at different angular speeds.

Piezoelectric ceramics were used in numerous applications as both sensors and actuators. One of the main reasons for the popularity of using piezoelectric sensors and actuators is their relatively low power consumption and linearity. Several research groups

use them for vibration suppression and energy harvesting through mounting on flexible beams. The key idea behind using piezoelectric ceramics for bending flexible beams is that once voltage is applied; the patch will either expand or contract depending on polarity.

In this experiment, four identical 15x19x0.19 mm PSI-5H4E piezoelectric ceramic actuators were used as shown in Figure 4-24. As also shown in the same figure, the actuators were connected in a parallel configuration with the stainless steel substrate acting as a common conductor. An E-835 Duract™ bipolar piezoelectric driver module was used to drive all piezoelectric patches simultaneously. This insured that the top set of patches shrank in-phase with expansion of the bottom set and vice versa. In case there was a phase shift, the excitation forces would not be symmetric which might had an effect on the desired mode shape of the drive beam.

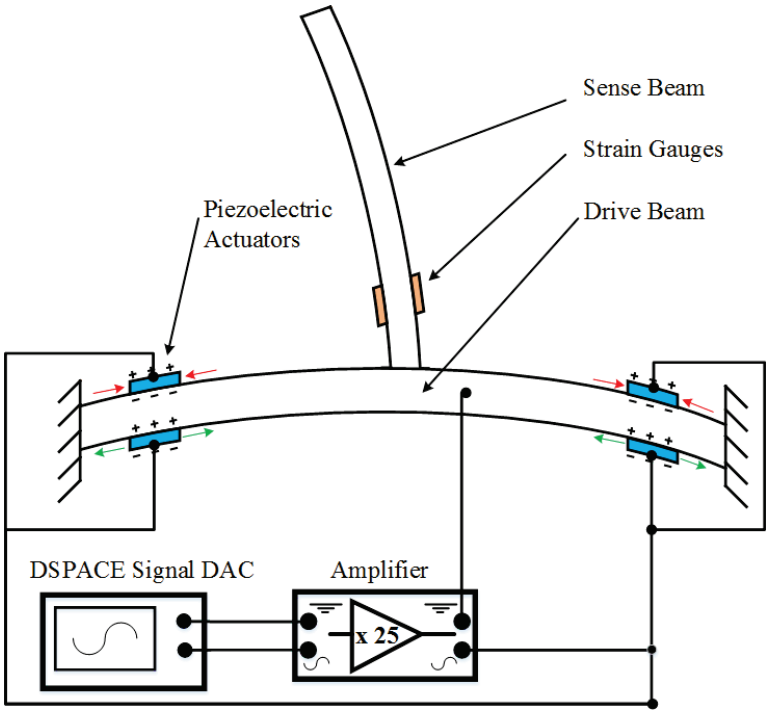

Figure 4-24: Piezoelectric actuator configuration for exciting the T-beam using four piezoelectric actuators connected to one amplifier

Similar to strain gauges, the same mounting Cyanoacrylate glue (Z70) was used to fix the piezoelectric patches in place. It is worth noting that Cyanoacrylate acts as an insulator, which posed a challenge as good conductive connections were needed to be made

between the bottom side of the patches and the stainless steel substrate. As a solution, a drop of 8330S silver conductive epoxy was first applied to the middle of the patch. After that, a thin layer of Cyanoacrylate glue was spread across the area around the conductive epoxy before pressure was applied for two minutes to insure a strong electrical and mechanical bonds between the two surfaces.

Frequency Response

At first an initial deflection and impulse response test was performed to fine-tune the structure to 2:1 resonance. Examining the initial deflection results shown in Figure 4-25, one can see that the sense mode natural frequency labelled {1} is 21.48 Hz and it's second harmonic labelled {2} 42.97 Hz while the drive mode natural frequency labelled {3} is 44.5 Hz, 1.62 Hz away. The resonance ratios between the point {2}, {3} and {1} are 2.00 and 2.07.

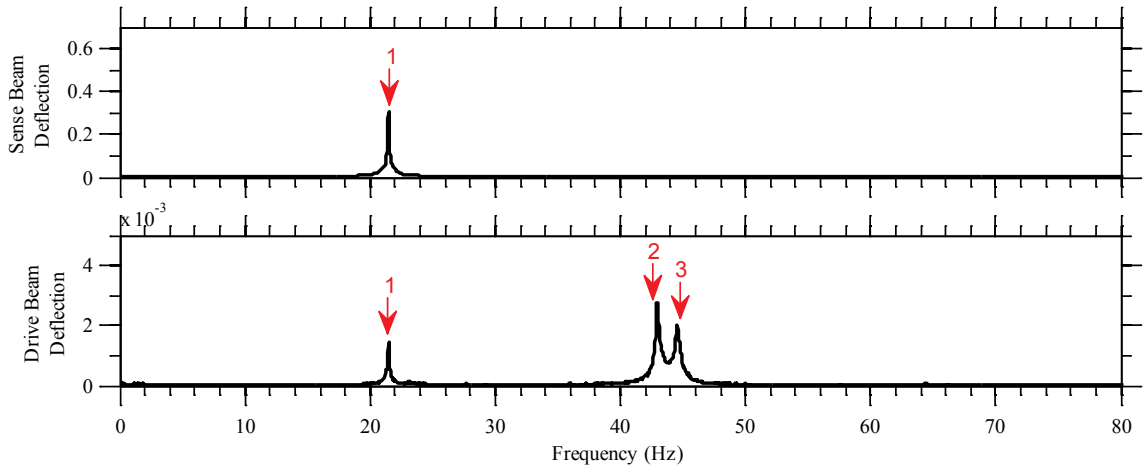

Figure 4-25: Initial deflection time history tests results for the second T-beam prototype, drive beam (top) and sense beam (bottom)

As a next step, a series of slowly varying frequency sweep tests with a slope of 0.001 Hz/sec were performed to obtain accurate frequency response curves. The first experiment shown in Figure 4-26 shows the effect of different excitation amplitudes over a frequency sweep passing the sense mode natural frequency. As expected, results show that the sense beam frequency peak behaved linearly in the frequency domain (i.e. single

sharp peak rather than flattop) irrelevant of excitation amplitudes. The sense beam deflections amplitudes ranged from 6 μm at 7 V to 10 μm at 9 V, respectively.

On the other hand, the drive beam deflection showed rather interesting behaviour. At lower excitation amplitudes (i.e. 7 V and 8 V), the drive beam's frequency response was similar to that of the linear case. However, at 9 V excitation amplitude, the drive beam showed a significant increase in bandwidth (doubled). It is worth noting that the drive beam peak-to-peak deflection was smaller than that of the sense beam's (0.6 μm and 0.4 μm). This was due to the nature of its boundary conditions as well as dimensions compared to the sense beam. The higher frequency components for both the sense and the drive beams are shown for the reader's convenience.

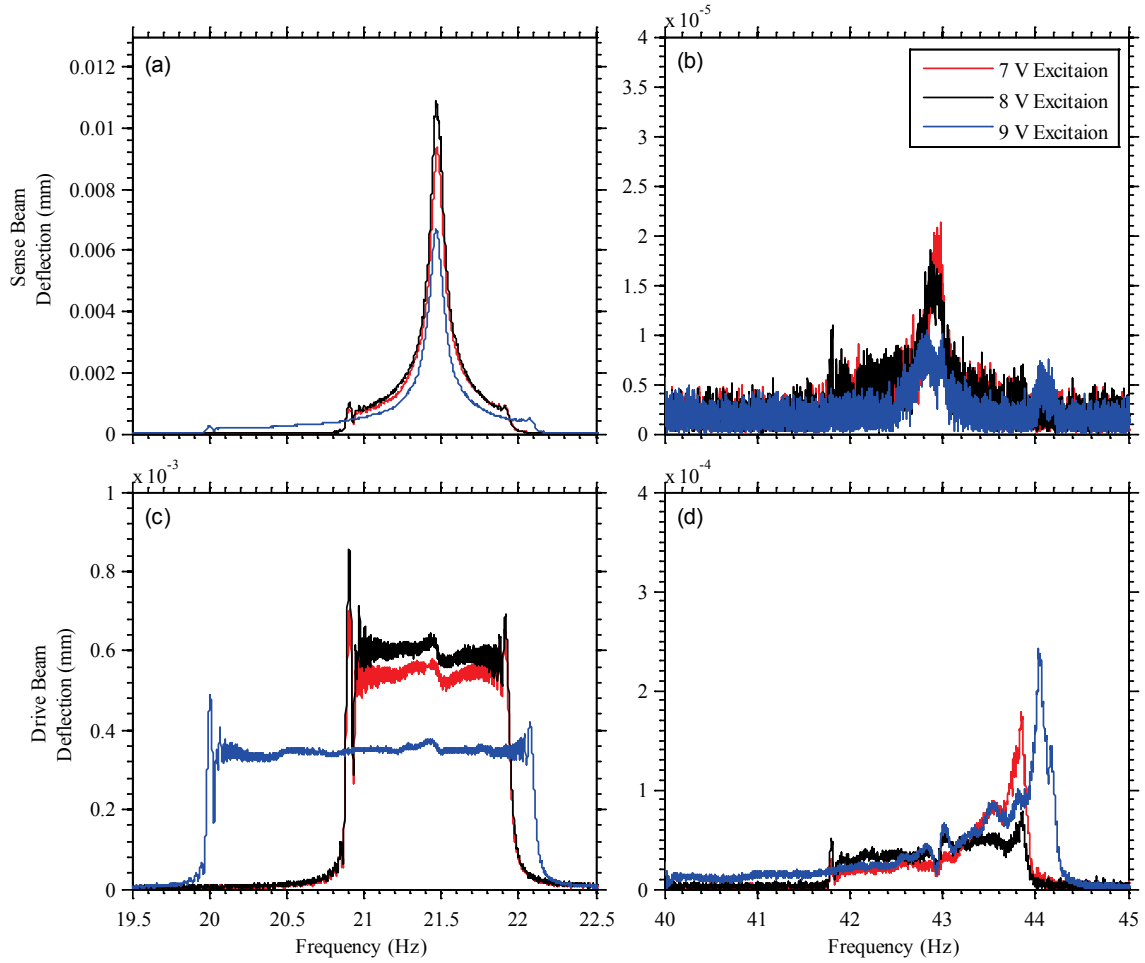

Figure 4-26: Effect of excitation amplitude on the frequency response in the linear case, sense beam deflection (a, b) and drive beam deflection (c, d)

With the purpose of studying the nonlinear frequency response of the system, the excitation frequency sweep was shifted to around twice the sense mode natural frequency (42.5 Hz to 43.5 Hz) using the same slope as the previous test. The experimental results are shown in Figure 4-27, the sense beam responded near its own natural frequency (half that of excitation) showing a nonlinear flat-top behaviour at 9 V excitation amplitude.

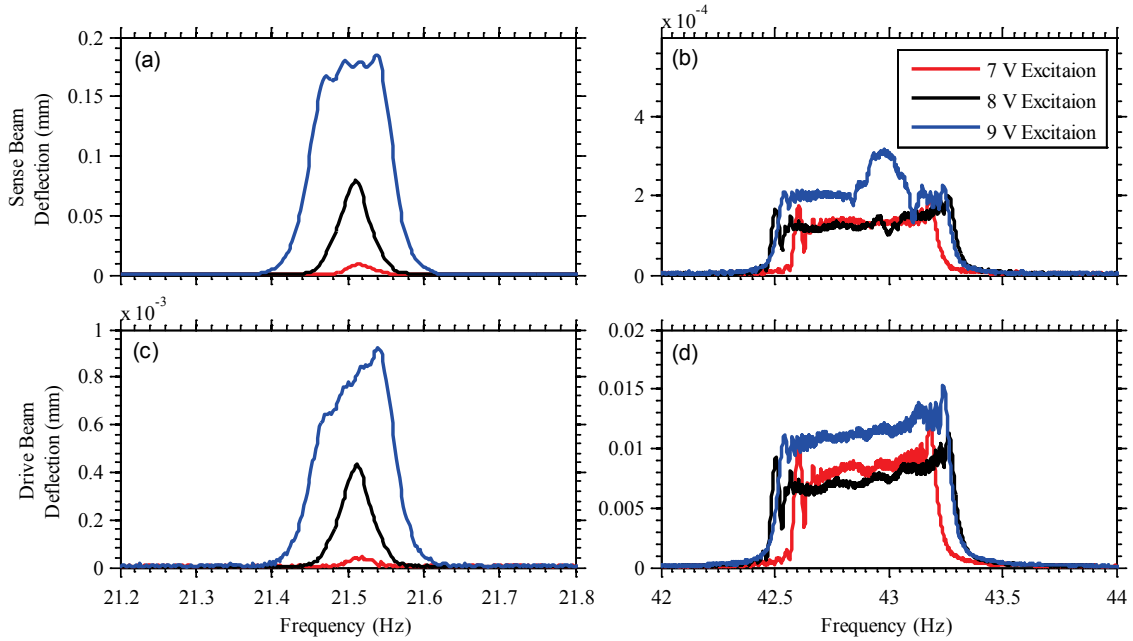

Figure 4-27: Effect of excitation amplitude on the frequency response in the nonlinear excitation case, sense beam deflection (a, b) and drive beam deflection (c, d)

It is also worth noting that the sense beam response amplitude increased to approximately 15-times more than the previous "linear" case. Both linear and nonlinear results are compared in Figure 4-28. It can be observed that by increasing excitation amplitude, not only a significant flat-top bandwidth can be achieved, but in this case, also the overall gain (i.e. quality factor) was increased.

Saturation

The saturation test for this design also matches the theoretical expectation. For this test, the excitation frequency was fixed at 21.5 Hz for the "linear" case and 42.8 Hz for the "nonlinear" case and all excitation amplitude sweeps were introduced at a 0.01 V/sec slope.

As shown in Figure 4-29, the linear case response amplitude increased linearly as expected. On the other hand, the sense beam started to respond in the nonlinear case after a threshold excitation amplitude of approximately 3.5 V was exceeded. After that, it increased almost linearly after 4 V.

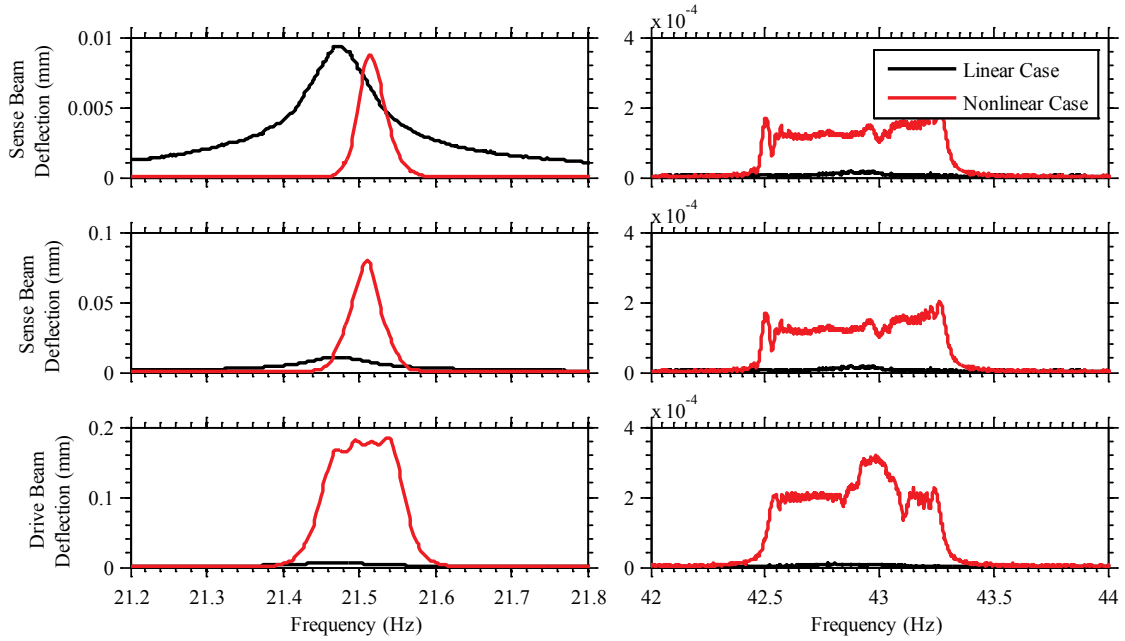

Figure 4-28: Comparison between the linear and nonlinear frequency responses of the sense beam excitation amplitudes of 7 V (a, b), 8 V (c, d) and 9 V (e, f)

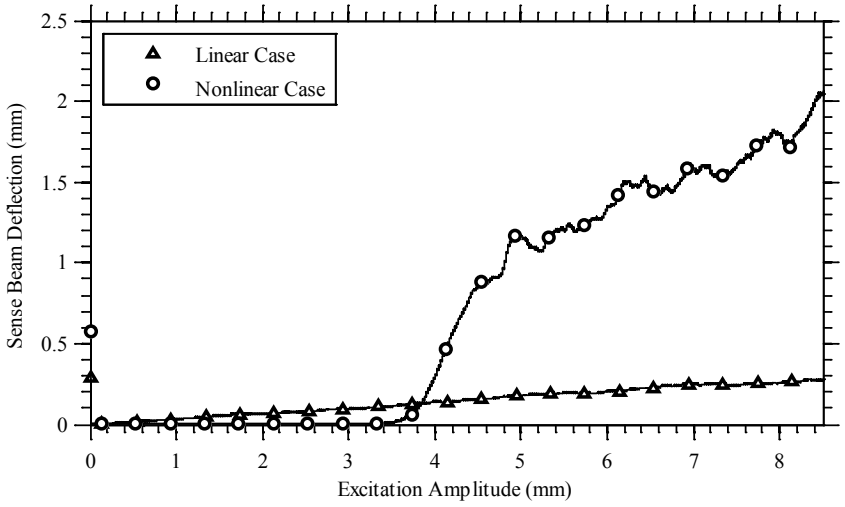

Figure 4-29: Second Macro T-beam prototype saturation experimental results showing the transfer of energy to the sense beam in the nonlinear case

Gyroscope Experiments

This experimental prototype had the same mechanical structure as the second resonator prototype with the exception of sensors. A state-of-the-art rate table (Ideal Aerosmith 1621-200A-TL) was used in this test as a replacement for the custom made one. In addition, the rate table's angular velocity was monitored through interfacing the DPSACE DAQ card with the analog output of the rate table's controller as shown in Figure 4-30.

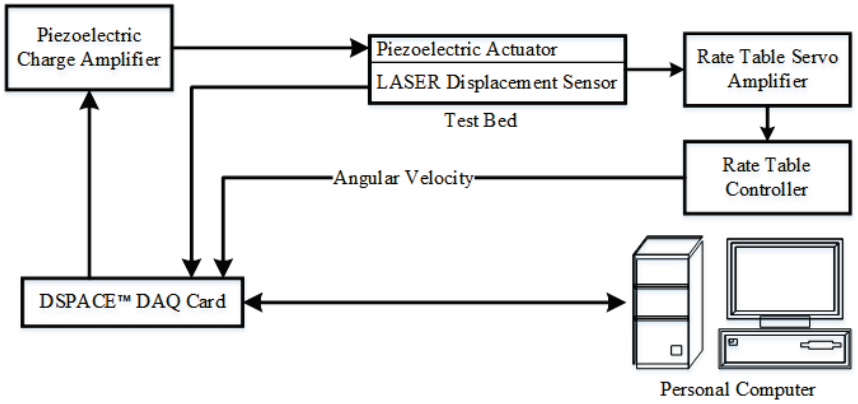

Figure 4-30: Gyroscope test bed system block diagram

The Linear case: $\Omega_{exc} = \omega_{sense}$

In this test, excitation frequency was fixed at the sense mode natural frequency (i.e. $\omega_s = 21.5$ Hz) and piezoelectric actuator excitation amplitude of 9 V. This choice of excitation amplitude was because the same structure showed nonlinear behavior in the resonator experiments. Angular velocity was then increased at the slowest possible acceleration allowed by the rate table $\left(0.256\,\text{deg/sec}^2\right)$ resulting in the time domain results shown in Figure 4-31. A linear increase in the sense beam deflection was observed starting at approximately 15 deg/sec up to 58 deg/sec with sensitivity of $0.7\ \mu\text{m/deg/s}$. However, after the angular velocity exceeded 58 deg/sec, sense beam deflection sensitivity to angular velocity became inversely proportional. This was due to the centripetal forces applied on the structure counteracting the drive forces exerted by the piezoelectric actuators.

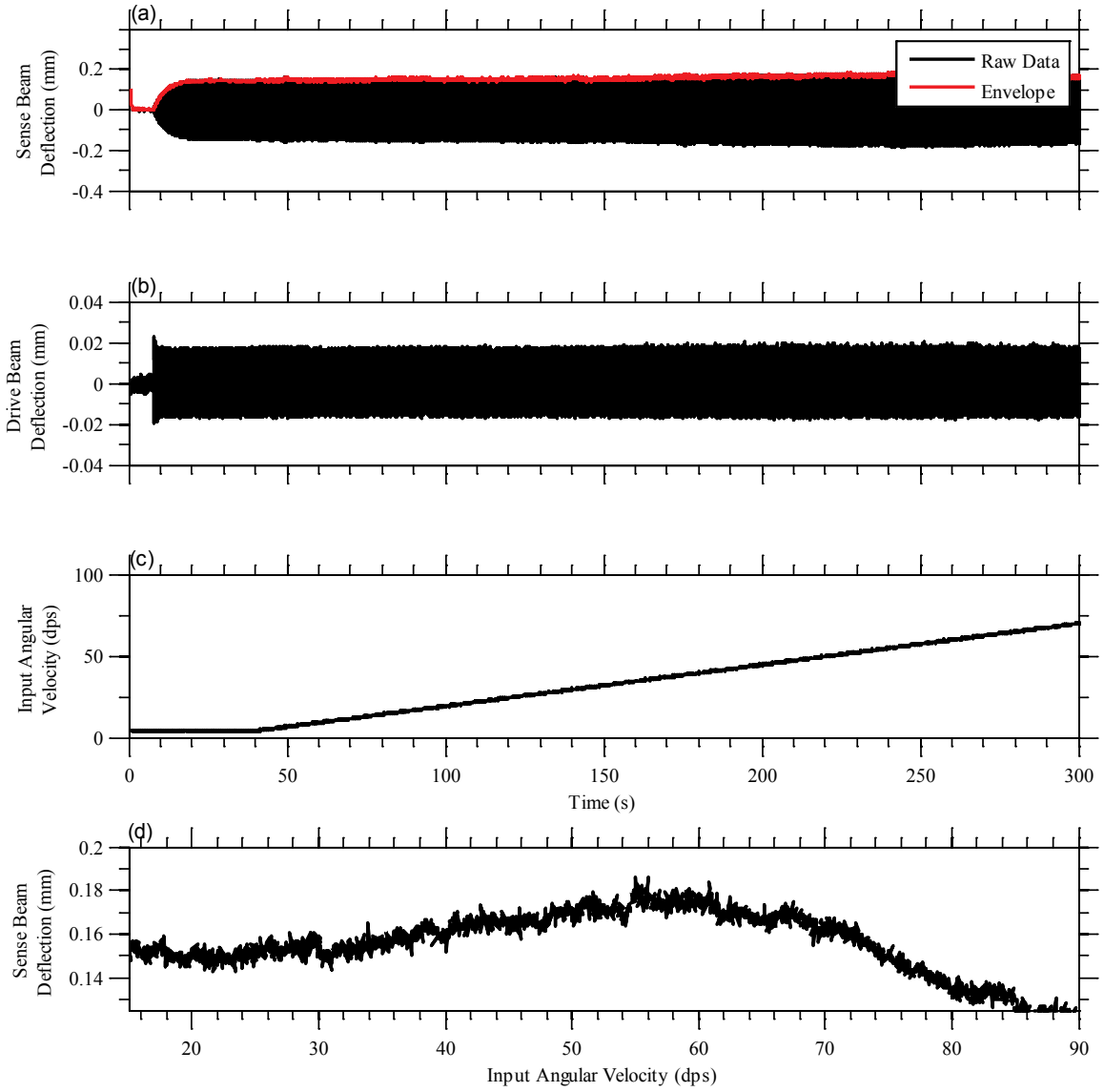

Figure 4-31: Linear case time history results showing the deflection in the sense and drive beams respectively (a, b) in response to a ramp angular velocity signal (c). Calibration curve (d) shows sensitivity of the sense beam against angular velocity

The Nonlinear case: $\Omega_{exc} = \omega_{drive} = 2\omega_{sense}$

In this case, excitation amplitude was fixed similar to the linear case experiments but excitation frequency was doubled. This facilitates the comparison between the linear and nonlinear cases of the same structure. Figure 4-32 shows the envelope of the sense beam deflection increasing proportionally with angular velocity with sensitivity of $22\ \mu m/deg/s$, 21 times higher than the linear case.

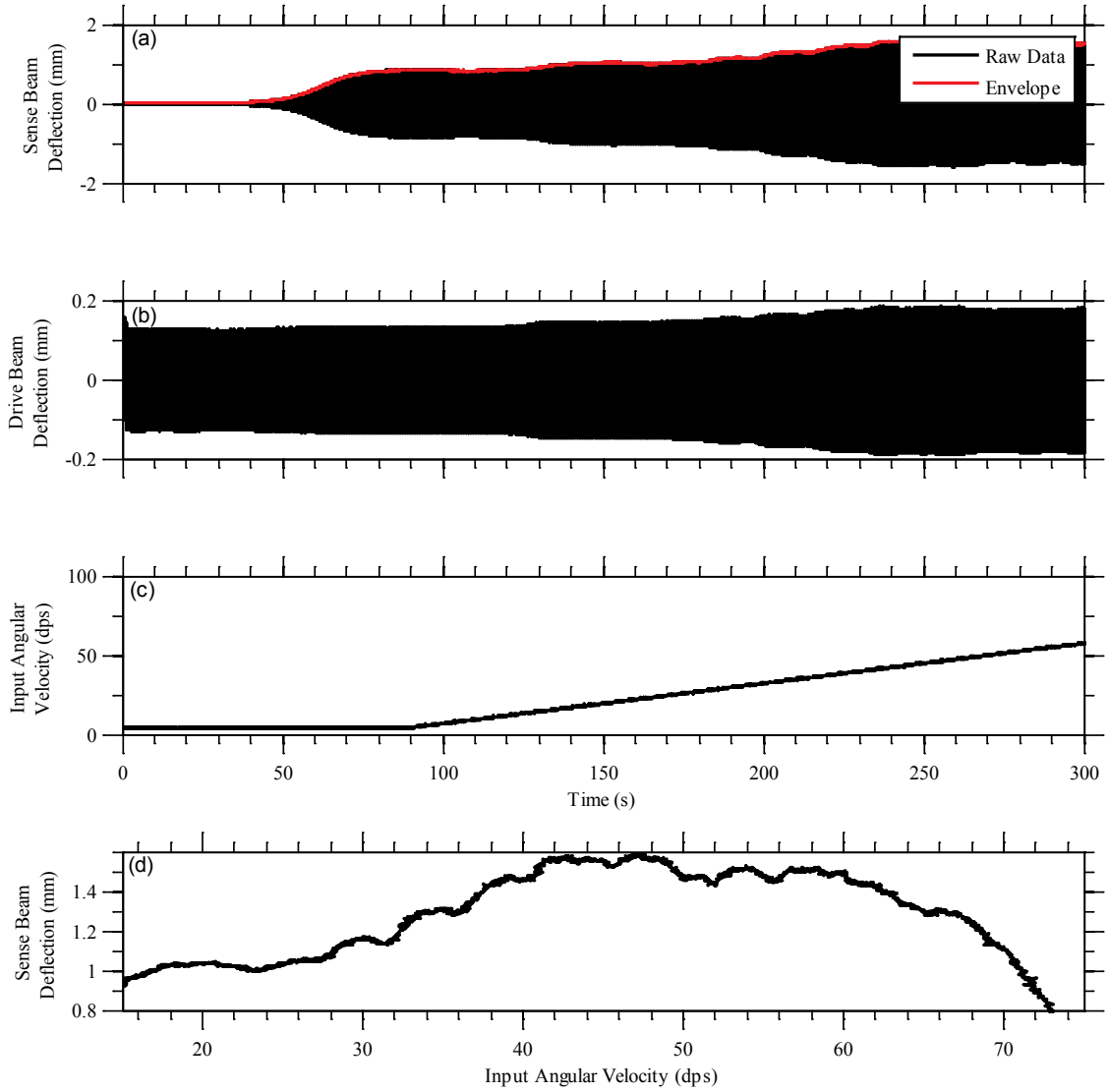

Figure 4-32: Nonlinear case time history results showing the deflection in the sense beam (a) and drive beam (b) in response to a ramp angular velocity signal (c). The calibration curve (d) shows sensitivity of the sense beam deflection versus angular velocity

It can be also seen that the centrifugal force affected the drive beam displacement after the same angular velocity threshold was exceeded. In-turn the sense beam response was affected. This drawback can be addressed in the future through the use of feedback control algorithms to regulate the drive beam deflection.

Linear vs Nonlinear Frequency Response

In addition to evaluating the linear vs nonlinear frequency responses of the structure as a resonator, the effect of angular velocity on the frequency response was established. The two shown frequency sweep results in Figure 4-33 were performed at angular velocities of 30 and $40\,\mathrm{deg}/s$ respectively.

It was found that the frequency peaks were shifted at the two input angular velocities. In turn, this structural natural frequency shift detuned the system away from the frequency of the drive signal significantly after $45\ \mathrm{deg/s}$. As a result, this angular velocity threshold behaved as an upper bound for this design. One method used in MEMS gyroscopes designs is to track the resonance frequency of the structure using a phased locked loop to maintain consistent performance at the cost of system complexity.

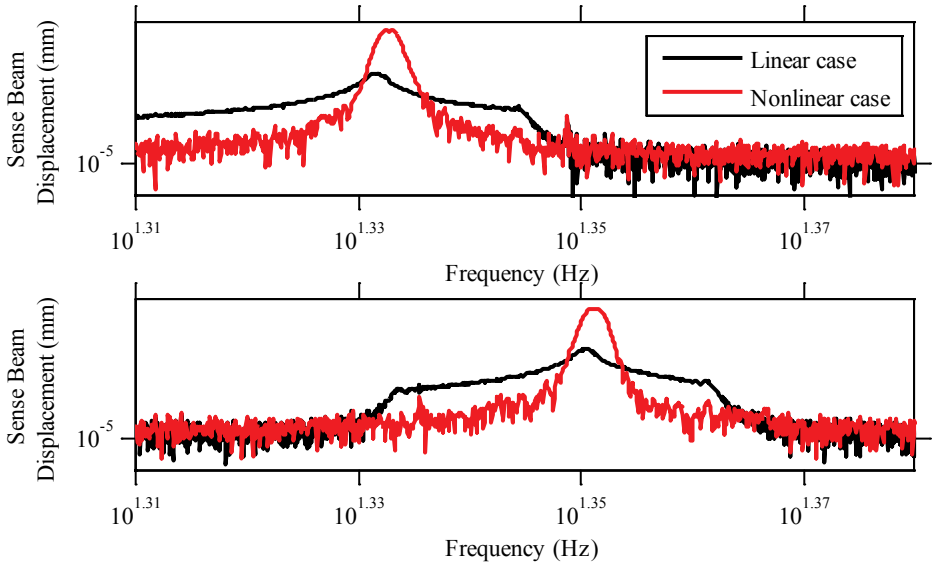

Figure 4-33: Comparison frequency responses in the linear and nonlinear cases to a swept sine excitation at angular velocities of 30 deg/sec (top) and 40 deg/sec (bottom)

4.4. Feedback Control for Bandwidth Enhancement

In addition to the increase in bandwidth associated with internal resonance, more robustness was achieved by introducing simple closed-loop feedback control. The general idea was to feedback a coupling nonlinear term -or a combination of nonlinear terms- to be added to the excitation signal. If tuned correctly, this was found to increase the coupling between the drive and sense beam which in-turn facilitated the transfer of energy between the two vibration modes.

In this section, the effect of using the measured in-plane velocities of the centers of mass of the drive and sense beams represented by $\dot{x}_d$ and $\dot{x}_s$ to achieve an increase in bandwidth. The reason behind this choice of quadratic coupling term is its resemblance to a Coriolis-like term in gyroscopes. Moreover, a simple proportional controller was used to tune the effect of the aforementioned nonlinear terms on the amplitude of the excitation signal similar to amplitude modulation as

$$(A + K_p \dot{x}_s \dot{x}_d) \sin(\omega t) \tag{4.1}$$

Such that A is the minimum excitation amplitude in volts observed to drive the system to operate in its nonlinear region (A was set to 9 V for this test bed).

Moreover, in order to avoid driving the system to instability that might damage the test bed, the tuning gain K_p was introduced. It was used in studying the effect of the nonlinear term (i.e. $\dot{x}_s \dot{x}_d$) on the system's overall response. A preliminary experiment was first performed to estimate the maximum possible value of the nonlinear terms without introducing the gain K_p as shown in Figure 4-34.

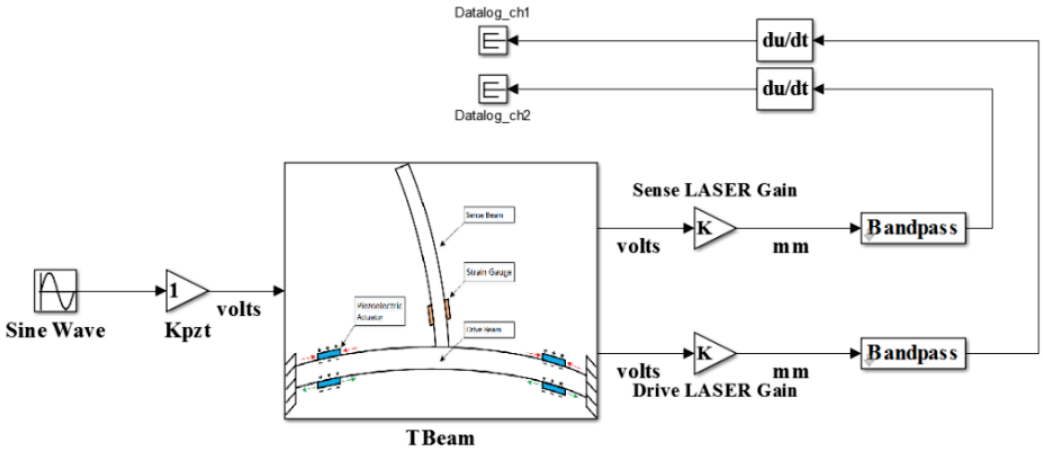

Figure 4-34: Preliminary test to estimate the maximum value of the term $\dot{x}_s\,\dot{x}_d$

After that, the system was excited at its higher natural frequency to induce the nonlinear response with the highest drive amplitude possible. For this experiment the maximum measured value for $\dot{x}_s\,\dot{x}_d$ was 2000. Consequently, the nonlinear term $\dot{x}_s\,\dot{x}_d$ was first normalized by the aforementioned estimate (i.e. 2000) to insure stability and then amplified by the gain K_p as shown in Figure 4-35.

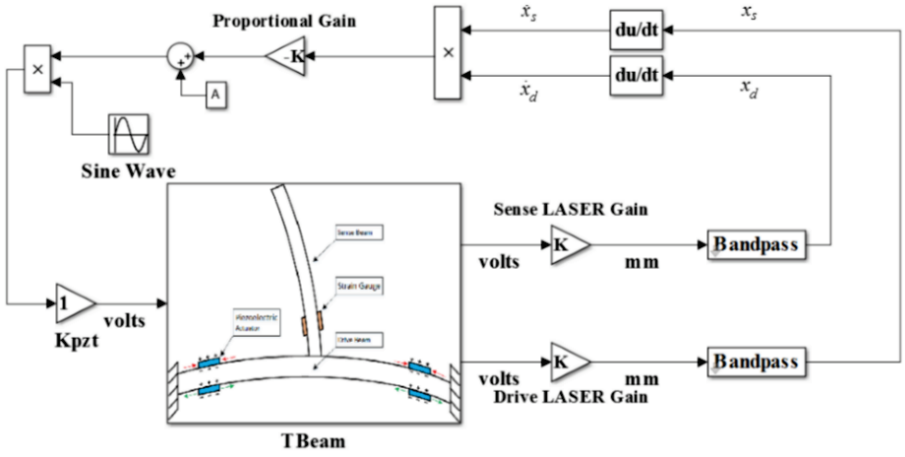

Figure 4-35: Proportional feedback algorithm of the nonlinear terms for bandwidth enhancement

Lastly, a series of experiments were completed using different values of the proportional gain K_p and a frequency sine sweep within the range of the second mode (i.e.

drive) natural frequency of the T-beam. Figure 4-36 shows the sense beam tip deflection in the frequency domain. A significant gain drop was observed in-line with increasing the proportional gain K_p until it diminished to zero at $K_p = 200$.

Figure 4-37 shows the effect in the time domain of increasing the gain positively compared to open loop excitation (i.e. $K_p = 0$). It can be observed that the sense beam time response amplitude decreased with increasing K_p. Moreover, the drive beam deflection exhibited no apparent change as the excitation frequency approached the drive mode natural frequency.

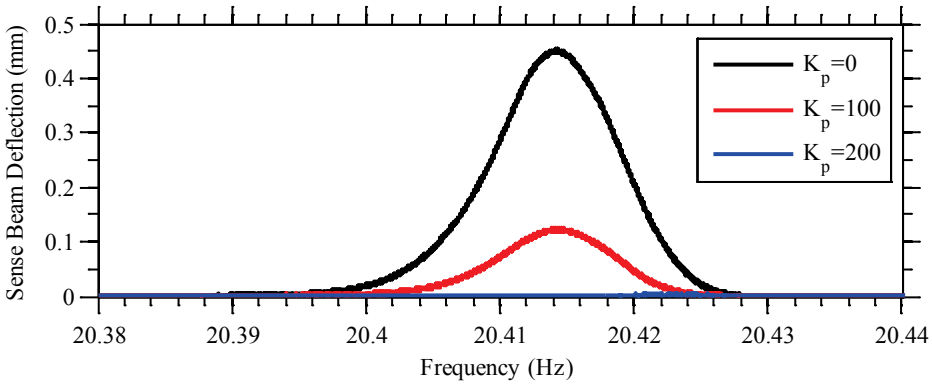

Figure 4-36: The effect of positive feedback gain on the sense beam frequency response, higher gain is observed in the frequency domain proportional to the feedback proportional gain Kp

Since the positive feedback gain showed not only gain degradation but also unobservable bandwidth enhancement, negative feedback gain was introduced. Figure 4-38 and Figure 4-39 show the relation between the system time responses given different negative feedback gain values. The first interesting effect to be observed is the significant change in the response of the nonlinear term compared to the previous case contributing to the excitation signal. Also, the drive beam deflection ascended to a stable amplitude within a frequency range around the drive mode natural frequency of 40.83 Hz between t=250 and t=300 seconds. As the proportional gain K_p was increased, the time interval at which the drive beam switches to the higher amplitude increased indicating a frequency response with higher bandwidth. Conversely, a gain beyond -900 forced the system to instability.

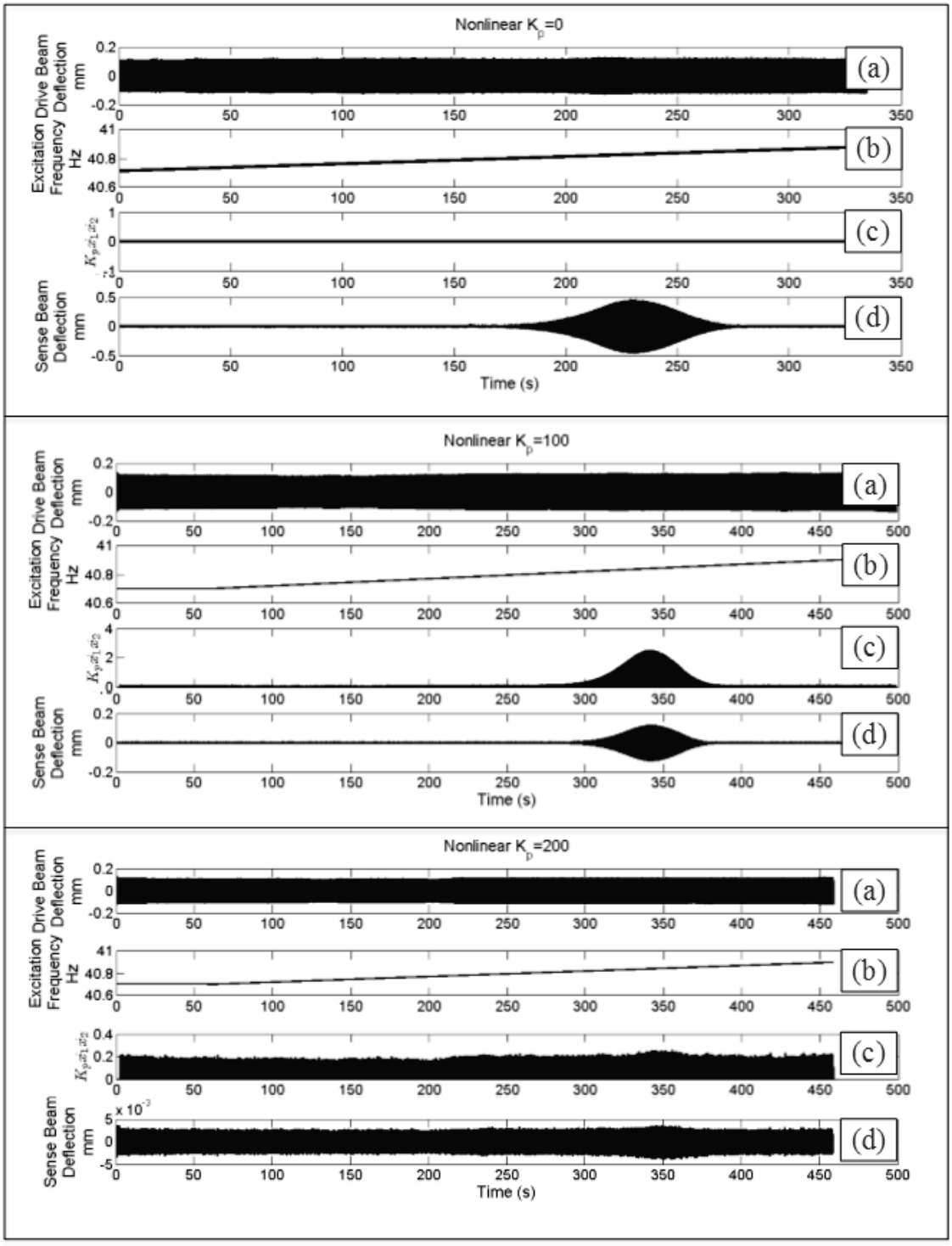

Figure 4-37: Time history during a frequency sweep (b) showing the effect of positive feedback of the nonlinear term (c), with gains K_p= 0, 100 and 200 on the drive beam (a) and sense beam (d)

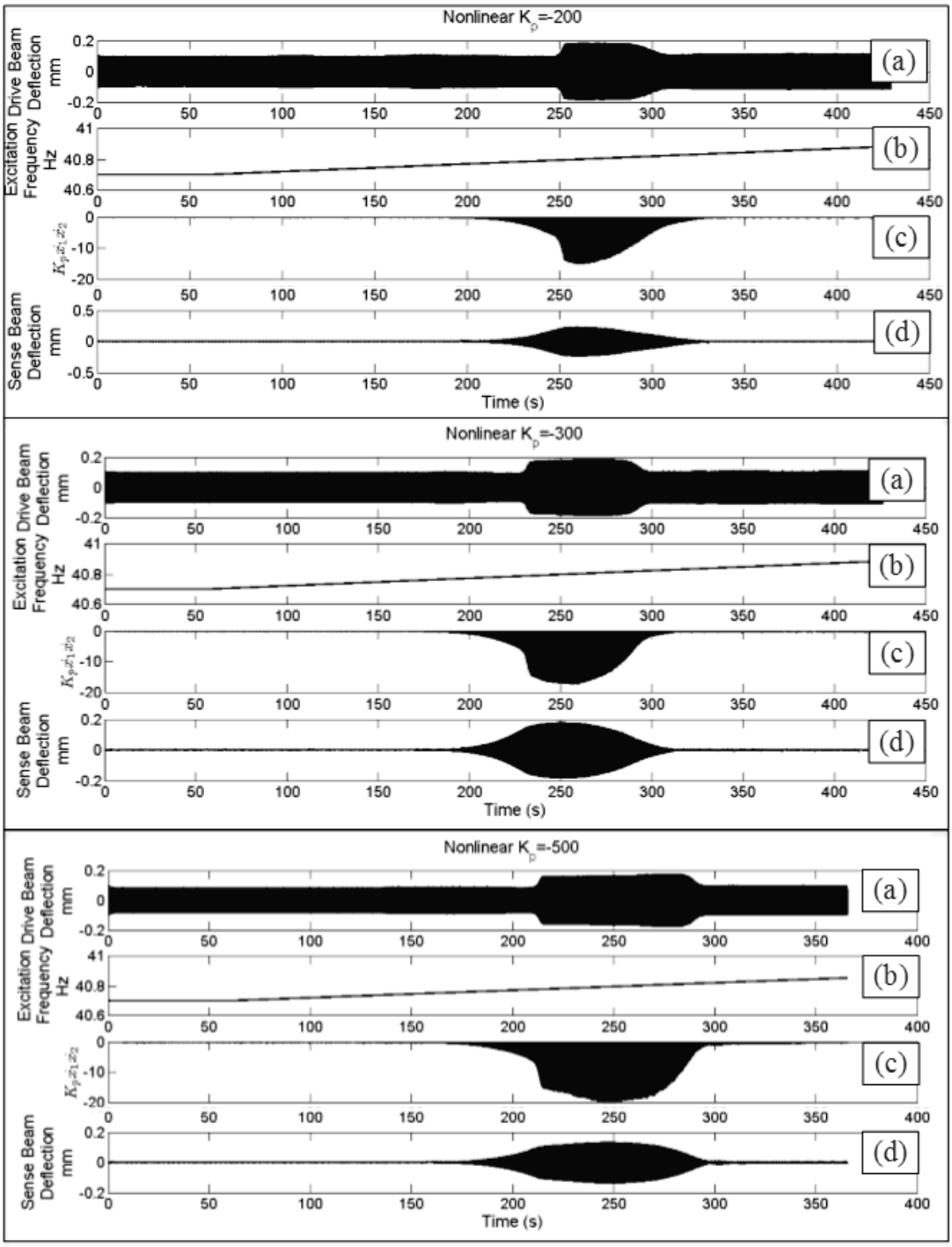

Figure 4-38: Time history during a frequency sweep (b) showing the effect of positive feedback of the nonlinear term (c), with gains K_p= -200, -300 and -500 on the drive beam (a) and sense beam (d)

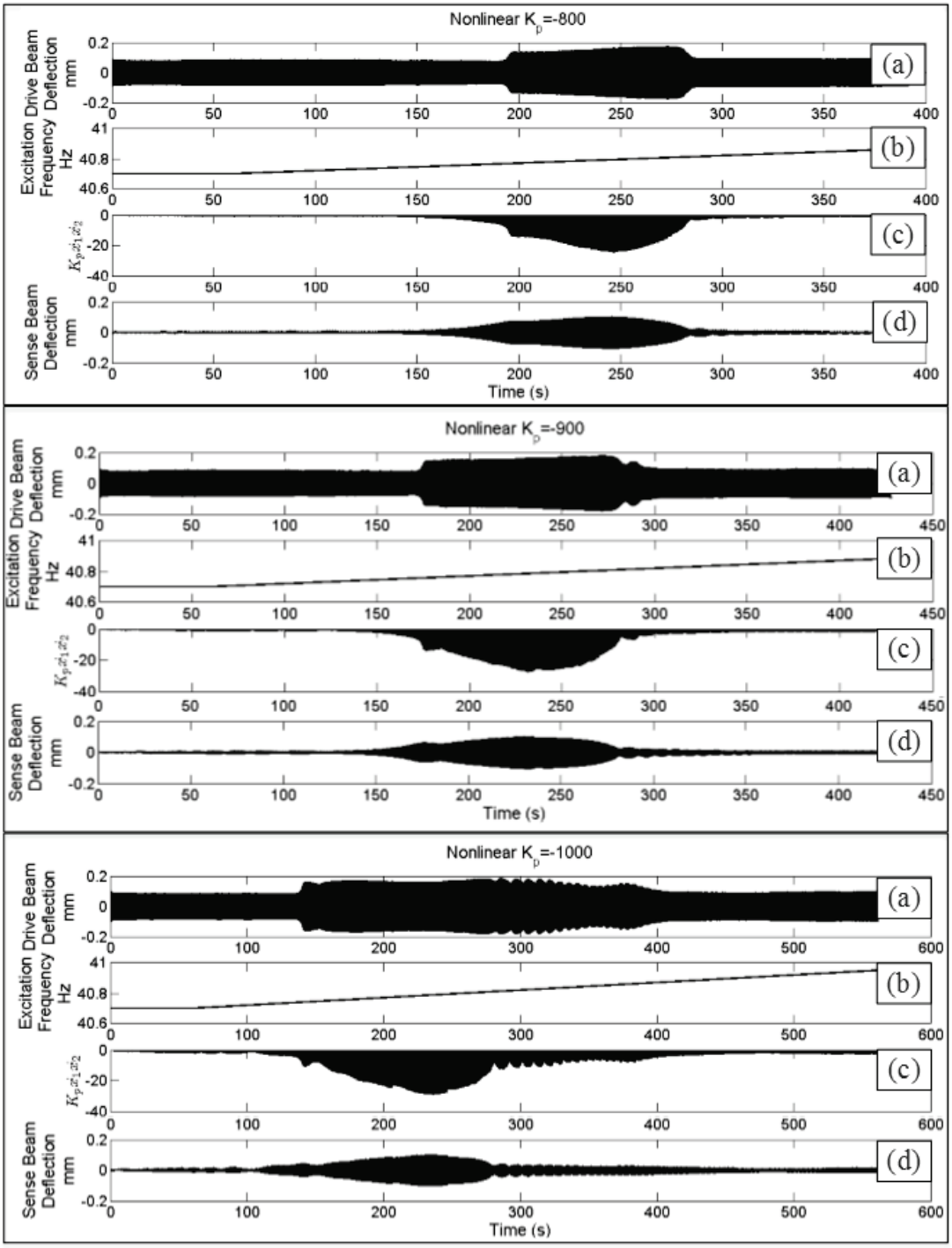

Figure 4-39: Time history during a frequency sweep (b) showing the effect of positive feedback of the nonlinear term (c), with gains K_p= -800, -900 and -1000 on the drive beam (a) and sense beam (d)

Similar to the positive feedback case, the sense beam frequency responses for different proportional gain values are compared in Figure 4-40. The sense mode bandwidth increased by increasing the proportional gain on the cost of decreasing the gain (i.e. quality factor). This aligned with the theoretical background established in the chapters two and three. It also proves the hypothesis that by amplifying the coupling terms between the two vibration modes, one can induce an increase in bandwidth.

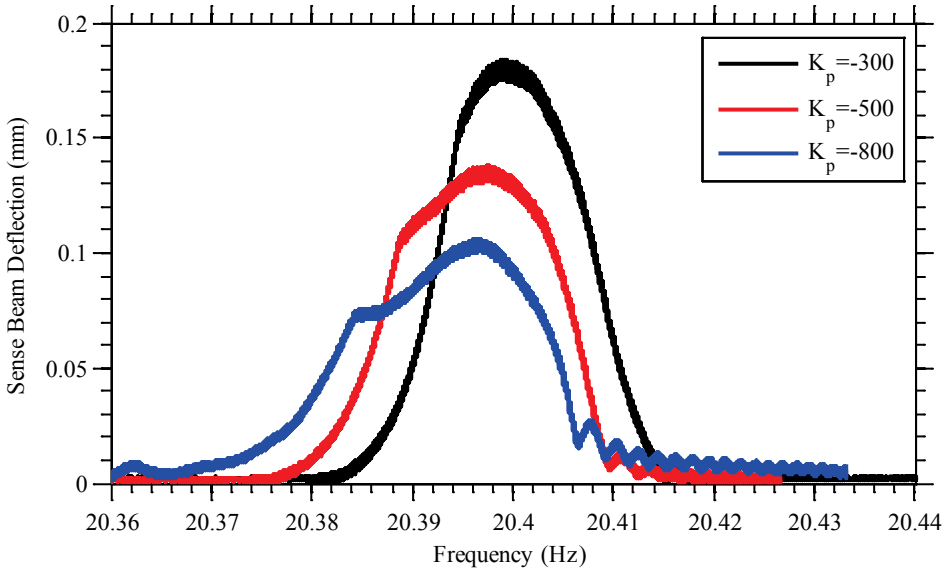

Figure 4-40: The effect of negative feedback gain on the sense beam frequency response, wider bandwidth with decreased gain was observed in the frequency domain proportional to the feedback proportional gain K_p

4.5. Conclusions

The experimental results shown in this chapter qualitatively validate the numerical simulation results for the gyroscope and resonator mathematical models shown in Chapter 3. The goals of increasing the sense mode bandwidth and the potential additional performance improvements that could be obtained using feedback of the appropriate nonlinear coupling terms to the forcing function were successfully achieved.

Chapter 5.

Conclusion and Future Work

The main objective of this research to establish the proof of concept in utilizing nonlinear internal resonance in modern gyroscope designs was successfully established. A theoretical background was founded by comparing typical gyroscope models to designs used in literature showing the effects of internal resonances on the frequency response. For each of the examined designs, the Coriolis-like terms as well as the coupling and quadratic nonlinearities were identified and related to similar terms in the gyroscope's equations of motion.

A mathematical model of a T-shaped two DOF structure was derived and solved both analytically and using numerical simulation. The analytical derivation used the Euler-Lagrange equations to derive the nonlinear coupled equations of motion. After that the equations of motion were nondimensionalized in order to study the modal interaction separately from physical units. This step will ease the transition from the macro-scale analysis performed in this research to future work on implementing this concept to the micrometer scale (i.e. MEMS gyroscopes). Moreover, the equations of motion were then scaled to examine the effect of nonlinearities on the overall system response. Lastly, the perturbation solution was derived to provide qualitative results to be later put in use during the design of experimental models.

An experimental test bed was developed to confirm the analytical results. These investigational results qualitatively showed promising trends to the corresponding numerical and analytical counterparts. A significant increase in the sense beam bandwidth with a flattop behavior was achieved in the case of 2:1 internal resonance. Nevertheless, this increase in bandwidth and gain was quasi-proportional to excitation amplitude. The sense beam deflection in the nonlinear case showed significant increase in the nonlinear resonance case over the linear case. Also the saturation phenomenon was analytically and experimentally validated.

The developed gyroscope design showed a linear relationship to angular velocity over an acceptable range. As future work, this measurement range limitation can be mitigated using a feedback control loop to track the drive mode natural frequency. Moreover, utilizing the analytical investigation, the nonlinear terms were added to the excitation frequency in a simple feedback scheme to the frequency response and achieve wider bandwidth while maintaining higher gains (i.e. quality factor).

The hypothesis of increasing the sense mode bandwidth through feedback of nonlinear coupling terms was established and validated by experimental results. Further studies can be completed on examining other coupling terms or a combinations of multiple terms weighted to achieve both higher quality factor and increase bandwidth as well as thorough stability analysis.

At the time of writing, our research team has successfully completed several preliminary MEMS gyroscope prototypes based on the concept of internal resonance established in this thesis. Nonetheless, the fundamental principles of nonlinear modal interactions as well as saturation can be projected to hold.

References

[1] C. Acar and A. Shkel, MEMS vibratory gyroscopes: structural approaches to improve robustness. Springer, 2008.

[2] "IEEE Standard Specification Format Guide and Test Procedure for Coriolis Vibratory Gyros," IEEE Std 1431-2004, pp. 1–78, Dec. 2004.

[3] J. Yang, E.-S. Choi, W. Chang, W.-C. Bang, S.-J. Cho, J.-K. Oh, J.-K. Cho, and D.-Y. Kim, "A novel hand gesture input device based on inertial sensing technique," in 30th Annual Conference of IEEE Industrial Electronics Society, 2004. IECON 2004, 2004, vol. 3, pp. 2786–2791 Vol. 3.

[4] Y. Tao, H. Hu, and H. Zhou, "Integration of Vision and Inertial Sensors for 3D Arm Motion Tracking in Home-based Rehabilitation," Int. J. Rob. Res., vol. 26, no. 6, pp. 607–624, Jun. 2007.

[5] N. Yazdi, F. Ayazi, and K. Najafi, "Micromachined Inertial Sensors," 1998, vol. 86.

[6] S. W. Shaw and B. Balachandran, "A Review of Nonlinear Dynamics of Mechanical Systems in Year 2008," 2008, vol. 2, no. 3, 2008.

[7] J. F. Rhoads, S. W. Shaw, and K. L. Turner, "Nonlinear Dynamics and Its Applications in Micro- and Nanoresonators," J. Dyn. Sys., Meas., Control, vol. 132, no. 3, pp. 034001–034001, Apr. 2010.

[8] A. Vyas, D. Peroulis, and A. K. Bajaj, "A Microresonator Design Based on Nonlinear 1:2 Internal Resonance in Flexural Structural Modes," Journal of Microelectromechanical Systems, vol. 18, no. 3, pp. 744–762, Jun. 2009.

[9] N. Parnian, "Integration of Local Positioning System & Strapdown Inertial Navigation System for Hand-Held Tool Tracking," Sep. 2008.

[10] P. Won, "Intelligent Fastening Tool Tracking Systems Using Hybrid Remote Sensing Technologies," May 2010.

[11] A. Marzouk, "A model based stroke rehabilitation monitoring system using inertial navigation systems," Thesis, School of Engineering Science - Simon Fraser University, 2009.

[12] R. P. G. Collinson, Introduction to Avionics Systems, 3rd ed. Springer, 2011.

[13] J. Bernstein, S. Cho, A. T. King, A. Kourepenis, P. Maciel, and M. Weinberg, "A micromachined comb-drive tuning fork rate gyroscope," in Micro Electro Mechanical Systems, 1993, MEMS '93, Proceedings An Investigation of Micro Structures, Sensors, Actuators, Machines and Systems. IEEE., 1993, pp. 143–148.

[14] J. Geen and D. Kraukauer, "New iMEMS Angular-Rate-Sensing Gyroscope." [Online]. Available: http://www.analog.com/library/analogdialogue/archives/37-03/gyro.html. [Accessed: 18-May-2014].

[15] P. Greiff, T. K. Boxenhom, and L. Niles, “Silicon Monolithic Micromechanical Gyroscope,” 1991.

[16] A. M. Shkel, R. Horowitz, A. A. Seshia, S. Park, and R. T. Howe, “Dynamics and control of micromachined gyroscopes,” in American Control Conference, 1999. Proceedings of the 1999, 1999, vol. 3, pp. 2119–2124 vol.3.

[17] A. Shkel and R. T. Howe, “Modeling and Simulation of Micromachined Gyroscopes in The Presence of Imperfections,” presented at the International Conference on Modeling and Simulation of Microsystems, Puerto Rico, 1999, pp. pp. 605–608.

[18] W. A. Clark, R. T. Howe, and R. Horowitz, “Surface micromachined Z-axis vibratory rate gyroscope,” in Tech. Dig. Solid-State Sensor and Actuator Workshop, 1996, pp. 283–287.

[19] X. Li, R. Lin, and K. W. Leow, “Performance-enhanced micro-machined resonant systems with two-degrees-of-freedom resonators,” Journal of Micromechanics and Microengineering, vol. 10, no. 4, p. 534, 2000.

[20] T. Usuda, “Operational characteristics of electrostatically driven torsional resonator with two degrees of freedom,” Sensors and Actuators A: Physical, vol. 64, no. 3, pp. 255–257, 1998.

[21] A. A. Seshia, “Design and Modeling of a Dual Mass SOI-MEMS Gyroscope,” Department of Electrical Engineering and Computer Sciences, University of California, 1999.

[22] U. Breng, W. Guttman, P. Leinfelder, B. Ryrko, S. Zimmermann, D. Billep, T. Gessner, K. Hillner, and M. Weimer, “A bulk micromachined gyroscope based on coupled resonators,” in Int. Conf. Solid-State Sensor and Actuators, 1999, pp. 1570–1573.

[23] J. J. Allen, C. W. Dyck, and R. J. Huber, “Parallel-Plate Electrostatic Dual Mass Oscillator,” Sandia National Labs., Albuquerque, NM (US); Sandia National Labs., Livermore, CA (US), 1999.

[24] C. Acar and A. M. Shkel, “An approach for increasing drive-mode bandwidth of MEMS vibratory gyroscopes,” Journal of Microelectromechanical Systems, vol. 14, no. 3, pp. 520–528, Jun. 2005.

[25] C. Acar, A. Schofield, A. Trusov, L. E. Costlow, and A. Shkel, “Environmentally Robust MEMS Vibratory Gyroscopes for Automotive Applications,” IEEE Sensors Journal, vol. 9, no. 12, pp. 1895–1906, Dec. 2009.

[26] S. Park and R. Horowitz, “Adaptive control for Z-axis MEMS gyroscopes,” in American Control Conference, 2001. Proceedings of the 2001, 2001, vol. 2, pp. 1223–1228.

[27] R. P. Leland, “Adaptive tuning for vibrational gyroscopes,” in Proceedings of the 40th IEEE Conference on Decision and Control, 2001, 2001, vol. 4, pp. 3447–3452 vol.4.

[28] I. Sitaraman, Z. Yong, and M. Tamal, “Analytical modelling of cross-axis coupling in micromechanical springs,” in Modeling and Simulation of Microsystems, 1999, pp. 632–635.

[29] K. Y. Yasumura, “Energy dissipation mechanisms in microcantilever oscillators with applications to the detection of small forces,” 2001.

[30] F. Braghin, F. Resta, E. Leo, and G. Spinola, “Nonlinear dynamics of vibrating MEMS,” Sensors and Actuators A: Physical, vol. 134, no. 1, pp. 98–108, Feb. 2007.

[31] D. J. Ewins, “Modal testing: theory, practice and application, 2000,” Research Studies Press LTD., Baldock, Hertfordshire, England, vol. 171, pp. 415–437.

[32] F. Braghin, E. Leo, and F. Resta, “Numerical and experimental analysis of a nonlinear vibrating MEMS,” in ASME 2005 International Mechanical Engineering Congress and Exposition, 2005, pp. 253–261.

[33] M. I. Younis, MEMS Linear and Nonlinear Statics and Dynamics: Mems Linear and Nonlinear Statics and Dynamics, vol. 20. Springer, 2011.

[34] J. A. Geen, S. J. Sherman, J. F. Chang, and S. R. Lewis, “Single-chip surface-micromachined integrated gyroscope with 50/spl deg//hour root Allan variance,” in Solid-State Circuits Conference, 2002. Digest of Technical Papers. ISSCC. 2002 IEEE International, 2002, vol. 1, pp. 426–427 vol.1.

[35] A. G. Haddow, “Theoritical and Experimental Study of Modal Interaction in a Two DOF Nonlinear Structure,” PhD, University of Dundee, Scotland, 1983.

[36] M. Farid Golnaraghi, “Vibration suppression of flexible structures using internal resonance,” Mechanics Research Communications, vol. 18, no. 2–3, pp. 135–143, Mar. 1991.

[37] S. S. Oueini, A. H. Nayfeh, and M. F. Golnaraghi, “A Theoretical and Experimental Implementation of a Control Method Based on Saturation,” Nonlinear Dynamics, vol. 13, no. 2, pp. 189–202, Jun. 1997.

[38] K. L. Tuer, A. P. Duquette, and M. F. Golnaraghi, “Vibration Control Of A Flexible Beam Using A Rotational Internal Resonance Controller, Part I: Theoretical Development And Analysis,” Journal of Sound and Vibration, vol. 167, no. 1, pp. 41–62, Oct. 1993.

[39] A. P. Duquette, K. L. Tuer, and M. F. Golnaraghi, “Vibration Control Of A Flexible Beam Using A Rotational Internal Resonance Controller, Part II: Experiment,” Journal of Sound and Vibration, vol. 167, no. 1, pp. 63–75, Oct. 1993.

[40] M. F. Golnaraghi, “Chaotic dynamics and control of nonlinear and flexible arm robotic devices,” PhD. dissertation, mechanical engineering, Cornell, New York, 1988.

[41] A. P. Pisano and Y.-H. Cho, “Mechanical design issues in laterally-driven microstructures,” Sensors and Actuators A: Physical, vol. 23, no. 1–3, pp. 1060–1064, Apr. 1990.

[42] G. K. Fedder, “Simulation of Microelectromechanical Systems,” PhD, University of California, Berkley, 1994.

[43] A. Trusov, “Investigation of Factors Affecting Bias Stability and Scale Factor Drifts in Coriolis Vibratory MEMS Gyroscopes,” PhD, University of California, Irvine, 2009.

[44] A. G. Haddow, A. D. S. Barr, and D. T. Mook, “Theoretical and experimental study of modal interaction in a two-degree-of-freedom structure,” Journal of Sound and Vibration, vol. 97, no. 3, pp. 451–473, Dec. 1984.

[45] A. H. Nayfeh, Introduction to Perturbation Techniques. John Wiley & Sons, 2011.

[46] A. H. Nayfeh, D. T. Mook, and L. R. Marshall, "Nonlinear Coupling of Pitch and Roll Modes in Ship Motions," Journal of Hydronautics, vol. 7, no. 4, pp. 145–152, 1973.

[47] M. F. Golnaraghi, F. C. Moon, and R. H. Rand, "Resonance in a high-speed flexible-arm robot," Dynamics and Stability of Systems, vol. 4, no. 3–4, pp. 169–188, 1989.

[48] J. D. Cole and J. Kevorkian, "Uniformly valid asymptotic approximations for certain non-linear differential equations," Proc. Internat. Sympos. Non-linear Differential Equations and Non-linear Mechanics, Academic Press, New York, pp. 113–120, 1963.

[49] W. Weaver Jr, S. P. Timoshenko, and D. H. Young, Vibration problems in engineering. John Wiley & Sons, 1990.

[50] H. Waisman and H. Abramovich, "Active stiffening of laminated composite beams using piezoelectric actuators," Composite Structures, vol. 58, no. 1, pp. 109–120, Oct. 2002.

[51] A. Vyas and A. K. Bajaj, "Microresonator Designs Based on Nonlinear 1:2 Internal Resonance Between Flexural-Flexural and Torsional Flexural Structural Modes," Purdue University, West Lafayette, Indiana, 2008.